Master of Science Thesis

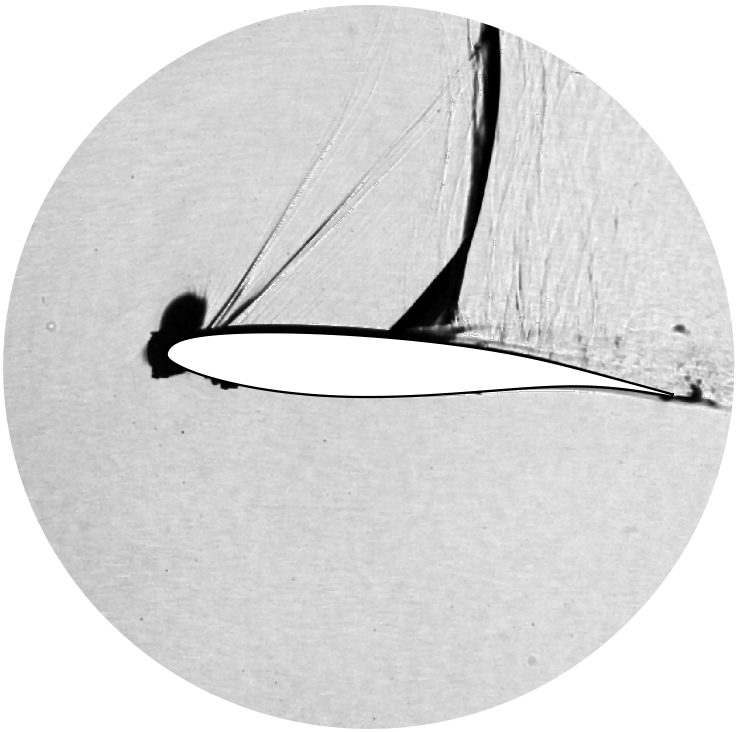

On the unsteady development of the flow under transonic Buffet conditions

Experimental study of the interaction of shock and pressure waves using PIV and Schlieren visualization

Roberto Solana Pérez

August 27, 2017

Aerodynamics

Faculty of Aerospace Engineering

TU Delft

Delft University of Technology

On the unsteady development of the flow under transonic Buffet conditions

Experimental study of the interaction of shock and pressure waves using PIV and Schlieren visualization

Master of Science Thesis

For obtaining the degree of Master of Science in Aerospace Engineering
at Delft University of Technology

Roberto Solana Pérez

August 27, 2017

Faculty of Aerospace Engineering · Delft University of Technology

Delft University of Technology

DELFT UNIVERSITY OF TECHNOLOGY
DEPARTMENT OF AERODYNAMICS

The undersigned hereby certify that they have read and recommend to the Faculty of Aerospace Engineering for acceptance the thesis entitled **"On the unsteady development of the flow under transonic Buffet conditions"** by **Roberto Solana Pérez** in fulfillment of the requirements for the degree of **Master of Science**.

Dated: August 27, 2017

Supervisors:

Dr.ir. B.W. van Oudheusden

Dr.ir. F.F.J. Schrijer

Dr. D. Ragni

Lo menos que podemos hacer, en servicio de algo, es comprenderlo.

The least we can do, in service of anything, is to understand it.

- J. Ortega y Gasset -

Acknowledgments

This Thesis project puts and end to my MSc studies at TU Delft and marks the end of a stage of my life. A new one starts now, and I would not like to enter it without first mentioning here all the people that have done of these past years a wonderful experience in this enthralling country that welcomed me with open arms, The Netherlands.

Firstly, I would like to thank my supervisors, Bas and Ferry, for their valuable input not only to this project, but to my training and preparation in the experimental ways. I would like to thank as well all the committee members of my defense for their effort. I also owe my gratitude to the technical staff of the high speed lab, specially Peter, Frits, Nico and Dennis, who helped me both in the day-by-day tasks and in moments of real trouble. I thank Paul for his valuable help during my experimental campaigns and the rest of the PhD students that at some point helped me. I really appreciate the time I spent in the basement with the rest of the MSc students, with no particular mention apart from the *TST-ST team*, Martin, Sumit and Qais, with whom I spent the most challenging moments, I thank all of you very much for making of these past months an unforgettable experience. My gratitude goes as well to all the people out of the academic environment that shared their time with me during these years.

Finally, I thank my family in my mother tongue...
Quiero agradecer de todo corazón a mis padres, Asun y Fernando, a mi hermano Miguel, a mi novia, Yas, y a mis abuelos, Josefina, Daniel, Dolores y Paco, por su incansable esfuerzo e incondicional apoyo a lo largo de todos estos años. Si alguien ha hecho posible que hoy yo sea quien soy y haya llegado hasta aquí, sin duda alguna, han sido ellos y a ellos les dedico mi trabajo. Por todo esto, gracias.

Summary

This thesis presents an experimental study of the unsteady phenomenon known as transonic buffet. Completely developed in the High Speed Lab of the Aerospace Faculty at TU Delft (The Netherlands), the experiments were conducted in the transonic/supersonic wind tunnel TST-27. In order to achieve time and spatial resolution of the phenomenon, high-speed Schlieren and time-resolved particle image velocimetry were used as the main measurement techniques over two aerodynamic models, the NACA0012 and the OAT15A. The aim of the project was to achieve fully developed buffet conditions, to study the time evolution of the flow and the dynamic characteristics of the features involved in the phenomenon, to investigate the wave propagation in the flow that maintains the self-sustained character of buffet and to study the origin and dynamic development of these waves.

An spectral analysis of the shock wave motion was done over all the experimental test cases to analyze the influence of different aerodynamic parameters (Ma, Re, α) over the phenomenon and to come up with the cases were buffet is most fully developed. The results showed that, as expected, there is a range of values of these aerodynamic parameters under which buffet develops, and out of this range it just vanishes. Buffet was fully achieve for the OAT15A model at $Ma = 0.70$, $\alpha = 3.5°$ and fixed transition at $x/c = 7\%$, on the other hand, buffet about the NACA0012 was not fully developed, but it was found to be stronger at $Ma = 0.70$, $\alpha = 4°$ and free transition. Note that the Mach values given are uncorrected, the respective corrected values can be found in 3.4.1. From the PIV results, the instantaneous and the phase-average velocity fields showed how the actual flow development takes place and all the features involved in the buffet cycles. It was shown that under fully developed buffet conditions, massive separation takes place from the shock foot and extends beyond the trailing edge during the upstream motion of the shock wave, whereas reattachment occurs in that region during the downstream motion of the shock.

Finally, a correlation analysis of the velocity fields demonstrated the presence of the so called *upstream traveling waves* shed at $\sim$ 2000 Hz and traveling upstream at $\sim$ 80 m/s. Furthermore, it was demonstrated that the vortices shed from the shock foot when full separation occurs are not the cause for the *upstream traveling waves*, instead they are originated by another type of disturbances shed when reattachment occurs at the shock foot. This made possible a reformulation of the hypothetical dynamic evolution of the features involved in the buffet cycles, explaining the links between them and the physical mechanisms that cause their self sustained development.

Table of Contents

List of Figures

List of Tables

Nomenclature

Abbreviations

AR	Aspect ratio
DFT	Discrete Fourier transform
FFT	Fast Fourier transform
FOV	Field of view
fps	Frames per second
HSL	High speed lab
LDV	Laser doppler velocimetry
PIV	Particle image velocimetry
PSD	Power spectral density
RMS	Root mean square
SIO	Shock induce oscillations
SWBL	Shock wave-boundary layer
UTW	Upstream traveling waves
WS	Window size

Greek Symbols

α	Angle of incidence
β	Prandtl-Glauert Factor
ϵ	Correction parameter
ϵ_m	Model blockage correction parameter
ϵ_w	Wake blockage correction parameter
ϵ_{corr}	Correlation uncertainty
ϵ_{cc}	Cross-correlation uncertainty
$\epsilon_{\vec{u}}$	Statistical uncertainty of $\vec{u}$
$\epsilon_{\vec{v}}$	Statistical uncertainty of $\vec{v}$

ϵ_{τ_p}	Particle slip uncertainty
ϵ_{sr}	Spatial resolution uncertainty
δ	Boundary layer thickness
Δ	Increment
Δt_p	Laser pulse duration
γ	Air specific heat ratio
$\chi(f)$	Fourier transform
κ	Digital resolution
λ	Geometrical airfoil constant, light wavelength
μ	Dynamic viscosity
π	Pi number
σ	Standard deviation
ρ	Density
τ_p	Particle relaxation time
τ_f	Flow characteristic time scale

Superscripts

sf	Shock foot
te	Trailing edge

Subscripts

corr	Corrected, correlation
loc	local
0	Total conditions
s	Static conditions
∞	Free stream conditions

Miscellaneous

$\vec{a}$	Particle acceleration
c	Chord length
c_L	Lift coefficient
c_d	Drag coefficient
f	Frequency
f_2	Focal length
$f_\#$	f-stop
h	Test section height

H	Height
I	Light intensity
k	Roughness element height
K	Gladstone-Dale contact
L	Length
Ma, M	Mach number
M_{corr}	Corrected Mach number
n	Refraction index
N	Ensemble size
P_0	Total pressure
P_s	Static pressure
R	Air gas constant
$R(\tau)$	Correlation parameter
Re	Reynolds number
Re_c	Reynolds based on the chord length
s	Light offset
S_k	Stokes number
Str	Strouhal number
t	Airfoil thickness, time
t_{exp}	Exposure time
T_0	Total temperature
T_s	Static temperature
T_p	Period of a buffet cycle
U_{corr}	Corrected velocity
U_∞	Free stream velocity
U_d	Velocity of downstream traveling disturbances
U_u	Velocity of upstream traveling disturbances
$\vec{u}$	Instantaneous velocity component
$\bar{u}$	Mean velocity component
$\tilde{u}$	Oscillatory velocity component
u'	Turbulent velocity component
W	Width
x_s	Shock wave position

Chapter 1

Introduction

Nowadays, modern commercial airliners and military jets fly in the lower transonic aerodynamic regime, i.e. at high subsonic cruise velocities slightly below the sound speed, $Ma \approx 0.78 - 0.85$. In this regime, both subsonic and supersonic conditions are present in the wing. Fig. 1.2 shows an schematic of the flow development as function of the Mach number over a standard airfoil from subsonic to supersonic conditions. For the region of interest, i.e. the *lower transonic* regime, a supersonic region is formed, firstly on the suction side and then on the pressure side. This region is terminated by a quasi-normal shock wave that moves downstream for increasing Mach numbers, until reaching the trailing edge in the *upper transonic* regime. Fig. 1.1 shows a military fighter jet flying above the critical Mach number, i.e. under transonic conditions. This can be observed due to the presence of a condensation region, characteristic of transonic flows.

Figure 1.1: F-14D "Super Tomcat" fighter jet flying above critical Mach and experiencing transonic shock waves over the wings

Normally, under steady flow conditions the shock wave is expected to be steady, however there is a range of aerodynamic conditions (Ma, α, Re) under which the shock may become unsteady and it will oscillate. This oscillatory phenomenon is known as transonic buffet. The pressure field changes almost discontinuously across a shock wave, which means that an oscillating shock over the airfoil surface will largely affect the pressure field of such airfoil. This would influence its lift coefficient due to the varying loads, and even affect the wing structure under the aeroelastic phenomenon of buffeting, defined as the coupling of the solely aerodynamic buffet with the structural response of the wing. The shock induced fluctuations are specially severe over modern supercritical airfoils due to the higher amplitude achieved by such fluctuations. The airliners flight envelopes are restricted by buffet conditions, and this phenomenon plays an important role in design restrictions of modern aircrafts as shown in Fig. 1.3. This is why it is of paramount importance to completely understand buffet and its causes and consequences over the flow field. The understanding of this unsteady phenomenon will play a major role in the design of future highly-flexible light-weight wings for fuel efficient aircrafts, as well as in the design for compressor blades for fuel-efficient engines or the design of active and passive buffet control devices. Furthermore, the numerical simulation of this phenomenon is still a great challenge and further understanding of its physical mechanisms is a must.

Previous buffet investigations have mainly focused on analyzing the onset conditions of the phenomenon, i.e. the aerodynamic conditions (Ma, Re, α) under which buffet develops, and on studying the physical mechanisms that sustain the oscillatory motion. This experimental thesis project focuses on the study of the flow under fully developed buffet conditions, the aim is to study the different flow features that play a major role in the phenomenon, to capture their existence and their actual role and try to enhance the understanding of the features that are still not fully explained in the literature.

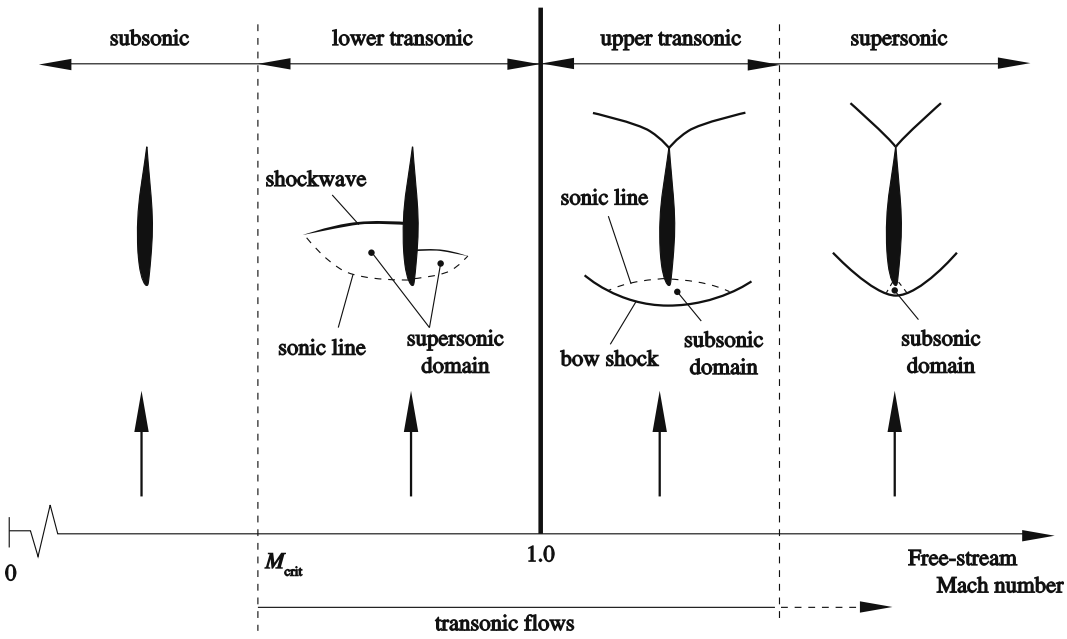

Figure 1.2: Basic types of external transonic flows, Moulden (1984)

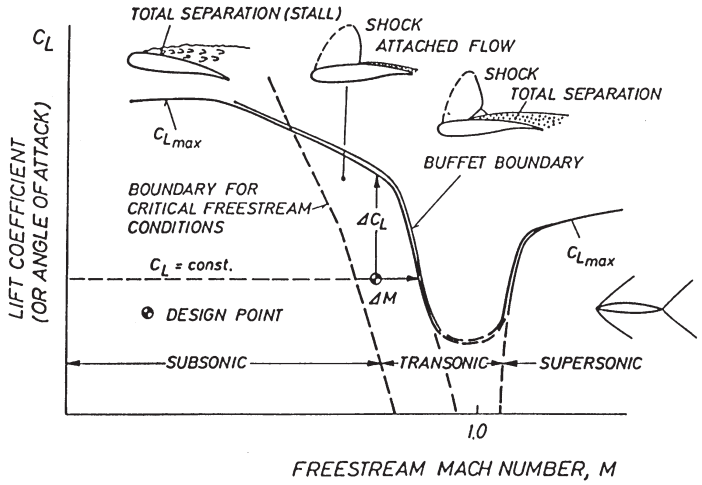

Figure 1.3: Lift coeff. as function of Mach number showing the buffet boundary and the design point safety margins of ΔM and ΔC_L, Stanewsky and Basler (1990)

1.1 Research objectives

The overall aim of the present study is to enhance the understanding of the physical mechanisms behind the buffet phenomenon that are not yet fully understood. In literature different approaches are found that explain the flow development during the buffet oscillatory cycles, however, a lack of knowledge and of agreement between different authors is found when defining the feedback mechanisms, their development and origin. With that purpose, the following research questions are posed, subdivided in several objectives that will ease the development and understanding of the project,

1. To develop an approach to experimentally achieve the unsteady aerodynamic phenomenon of buffet.
2. To study the influence of the Mach number, angle of incidence and boundary layer regime on the development of buffet.
3. To demonstrate the physical feedback mechanism that sustains the buffet motion, by
    - identifying the flow features that play a major role in the cyclic phenomenon;
    - capturing the existence of the so called *upstream traveling waves* and their dynamic behavior, i.e. velocity and frequency,
    - capturing the flow phenomenon or mechanism that acts as the origin of the *upstream traveling waves* and demonstrating their physical link,
    - demonstrating whether or not the vortices shed from the shock foot play a major role in the buffet cycle,
    - developing an explanation for the dynamic development of the buffet phenomenon, based on the previous findings, that includes and links all the flow features.

4. To identify the differences between the buffet development over a symmetric conventional airfoil (NACA0012) and a supercritical airfoil (OAT15A).

1.2 Methodology & Outline

In order to answer to these research questions an experimental study is carried out in the TST-27 transonic-supersonic wind tunnel of the TU Delft High Speed Lab. The study is performed over two different models that are representative of conventional (NACA0012) and supercritical (OAT15A) airfoils, under different flow conditions of angle of attack and Mach number that range in a combination of $\alpha = 0, 2, 3.5, 4$ and $Ma = 0.65 - 0.80$. The techniques used are Schlieren visualization, oil visualization and time-resolved planar particle image velocimetry, that allow to capture the shock position and the velocity fields in the desired flow region together with its temporal variation. The instantaneous and mean velocity maps allow for the identification and comparison of the main features of the flow involved in the buffet cycle development, as the separated region, the shock wave, the vortex shedding and the upstream traveling waves, and for the analysis of their unsteady development. Further information about the experimental approach and methodology is given in Chapter 3.

Chapter 2 gives background information about the state of the art of the research of buffet phenomenon currently available in the literature. An introduction to the phenomenon is given together with the main approaches, theories and conclusions from different authors. Chapter 3 is a description of the experimental techniques used for the research, together with the general experimental setup. Chapter 4 presents a mathematical description of the post-processing and analysis carried out over the experimental results. In Chapter 5 an introduction to the flow field is done. It focuses on the temporal development of the different features that play a role in the buffet phenomenon, and in the comparison of the flow field under different flow conditions (Ma, α, airfoil model, etc). It is mainly done by analyzing the instantaneous, mean and phase-average velocity fields obtained from the PIV measurements. Buffet is an unsteady phenomenon highly affected by pressure disturbances that travel in the upstream and downstream directions in the flow. This motivates an spectral analysis in Chapter 6 of the results obtained from Schlieren visualization of the empty test section with the aim of studying the presence and effect of the pressure waves originated by the wind tunnel noise. In Chapter 7 an spectral analysis of the shock wave motion under different values of Mach number and angle of attack is carried out in order to determine the flow conditions under which the phenomenon is most fully developed. The measurements from both Schlieren and PIV are analyzed and compared. Chapter 8 shows the wave propagation analysis done over the velocity fields obtained from the PIV measurements. The aim of this analysis is to capture the dynamic behavior of the *upstream traveling waves* and the vortex shedding at the separated region. A discussion about the physical mechanisms that sustain the buffet phenomenon is done in Chapter 9. Finally, the main conclusions are gathered in Chapter 10, together with some guidelines and recommendations for future work.

Chapter 2

Literature review

Many experimental and computational studies have been carried out since buffet was first detected more than seventy years ago by Hilton and Fowler (1952). These studies were mostly focused in 3 main topics. Namely, the determination of the aerodynamic conditions under which buffet occurs, the understanding of the physics of the phenomenon and different control methods to avoid it, delay it and diminish the impact of its consequences. An overview of previous relevant work from different authors related to buffet and its development is given in this chapter, basically focusing on the two first main topics, the buffet onset conditions and the physical mechanisms understanding. No research is made in buffet control techniques. The goal is to present the most up-to-date theories that describe the physics of the phenomenon as it is not yet fully understood and some discrepancies can be observed between different authors.

2.1 Buffet physical mechanisms and development

Buffet is an unsteady oscillatory periodic phenomenon characterized by a low-frequency high-amplitude movement of a shock wave over the surface of an airfoil for a specific range of aerodynamic parameters as Mach number, angle of incidence or Reynolds number. The phenomenon induces a complex unsteady coupling of different flow features that normally includes turbulent boundary layer separation and reattachment at the shock foot. This phenomenon is purely aerodynamic and not coupled with any structural behavior. In fact, the coupling of buffet with the structure is known as buffeting, an aeroelastic phenomenon which is out of the scope of this study. Since buffet was first discovered the main issue of most experimental, theoretical and numerical studies has been to understand the physics that define this phenomenon. Great progress has been made on this issue, however, the actual mechanisms that trigger buffet and that make possible the self-sustained motion are not yet completely understood. Several studies are analyzed in this section in order to show different approaches, conclusions and hypotheses that have been developed during the past years.

2.1.1 Shock wave oscillation properties

It has been experimentally proven that buffet occurs for a specific range of aerodynamic conditions and that out of this specific range the unsteady periodic oscillatory behavior disappears. In an experimental study about a thick circular-arc airfoil for $Re = 11 \cdot 10^6$, McDevitt et al. (1976) identified three different ranges in terms of shock wave behavior. The first one is a steady flow for low Mach numbers (found at $Ma_\infty = 0.72$) characterized by a weak quasi-steady shock wave and trailing edge separation of the boundary layer; the second is the unsteady flow range (found at $Ma_\infty = 0.754$), which in turn is characterized by the periodic oscillation of the shock wave both in location and strength and a coupling between the periodic oscillation of trailing edge separation and shock induced separation at the shock foot; the third range refers to the high Mach number domain (found at $Ma_\infty = 0.783$), characterized again by a quasi-steady strong shock that produces shock induced separation of the boundary layer. It was concluded that once the aerodynamic conditions are out of the buffet range the unsteady effects tend to disappear reaching again a steady state. This is a reason why the prediction of buffet onset and range of conditions is of paramount importance for a project that aims to study the buffet phenomenon, since it should focus in this specific range.

The general behavior of the shock wave in the mentioned unsteady domain is characterized by a periodic oscillating movement. There are three different types of shock motions over a surface as discovered by Tijdeman (1977), see Fig. 2.1. The first is type A or sinusoidal shock wave, this type is characterized by an almost sinusoidal motion with small amplitudes. The shock increases its strength when moving upstream reaching a maximum and decreases it when moving downstream reaching a minimum; the type B or interrupted shock wave is characterized by the vanishing of the shock wave in the downstream motion. Again the maximum is reached in the upstream motion; finally, type C or upstream-propagated shock wave is characterized by the upstream propagation of the shock wave from the leading edge with its posterior vanishing. Fully developed buffet conditions are normally associated to type A shock oscillations.

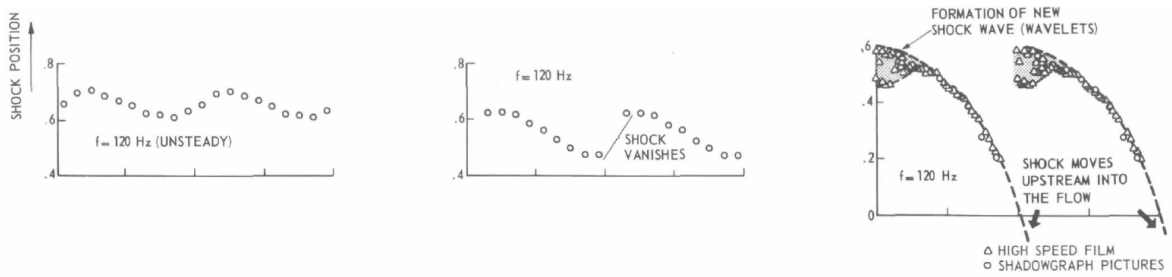

Figure 2.1: Shock movement types A, B and C from left to right presented as shock position (x_s/c) versus time, Tijdeman (1977)

2.1.2 Flow field development description

The first studies of buffet, done during the 70's and 80's, focused on the description of the flow field and the study of the flow parameters variation induced by the unsteady phenomenon of buffet. Most of those and later studies agree on their conclusions about the description of the flow field dynamic development. At certain critical conditions of Mach and Reynolds numbers and angle of attack, separation takes place at the shock foot. This separation is caused by a strong shock wave - boundary layer (SWBL) interaction that creates a recirculation bubble at the shock foot. Under these circumstances the separated region at the shock foot grows and can merge with the separated region in the trailing edge area (depending of the airfoil, this merging process may vary). This separation creates a change of the effective surface geometry in the region after the shock and, furthermore, the upstream shock movement starts. During the upstream motion of the shock, its strength increases due to the increased local Mach number caused by the higher relative velocity between shock and incoming flow. At some point during the upstream travel, the strength of the shock starts decreasing and reattachment occurs. It is then when the downstream motion of the shock occurs up to its original position. Then the cycle just repeats with a self-sustained character. Note that this is a mere description of the evolution of the phenomenon, and the physical causes and consequences of what is happening in every part of the cycle are not explained.

Levy Jr (1978) did a numerical study for steady and unsteady flow fields around a circular arc airfoil of 18% thickness for $Re = 11 \cdot 10^6$ and $Ma = 0.72, 0.754, 0.783$, comparing his results with the experimental measurements from McDevitt et al. (1976) and drawing the same conclusions. McDevitt (1979) showed that the unsteady phenomenon disappears if the communication between upper and lower surfaces over the trailing edge is avoided by using a splitter plate. This fact indeed demonstrates that buffet onset is related with boundary layer separation at the shock foot and trailing edge, and also with a communication process between both surfaces. However, this is not directly stated in these early studies. Roos (1980) performed an experimental study over a transonic Whitcomb airfoil of 11% thickness and a NACA0012 airfoil, both with forced transition at 35% chord. He found that for the NACA0012, separation starts as a recirculation bubble at the shock foot and then for increasing Mach number it grows towards the trailing edge region resulting in full separation. On the other hand, for the supercritical airfoil separation starts from the trailing edge. Roos (1980) also stated that in the region downstream from the shock, disturbances in pressure are convected upstream when the flow is attached and are convected downstream only in the separation region of the flow. As a result of a numerical study, Raghunathan et al. (1998) stated that the shock induced bubble plays a major role in the onset of buffet itself while it is the trailing edge separation behavior and size what affects most its amplitude.

A later experimental study on high subsonic flow over a NACA0012 airfoil was performed by McDevitt and Okuno (1985). It was shown in the Shadowgraph images that just at the buffet onset conditions, shock induced separation was taking place and as so, buffet could be characterized as a shock-induced phenomenon. The conclusions drawn in the study state that the triggering of buffet is the change from a normal shock to a periodic shock-induced separation due to an increase in the local Mach number or incidence angle. This fact would effectively modify the local geometry at the shock foot due to the

presence of a recirculation bubble, and would create an oblique shock. At the same time, the modification of the local curvature of the model would decelerate the flow and force it to recover its original configuration, creating the intermittent flow separation. Most recent studies always agree on the description of the buffet dynamic development, furthermore they focused not only on such description but on finding the physical reasons and mechanisms that cause and maintain such cyclic behavior.

2.1.3 Wave propagation approach for buffet

Following the results from Roos (1980) where it was found that, in the region downstream from the shock, disturbances in pressure are convected upstream when the flow is attached and downstream when the flow is detached, Lee (1989) reached a similar conclusion. Lee discovered the so-called Kutta waves traveling from trailing edge to the shock wave during buffet regime. Following this idea, changes in the wake cannot be communicated to the shock through the boundary layer of the upper surface due to separation and hence, the only way possible is the region outside the separated flow, as was mentioned by Lee (2001). This approach is the most widely used and accepted in the literature, and many posterior studies have focus on its explanation and on capturing the physical mechanisms involved.

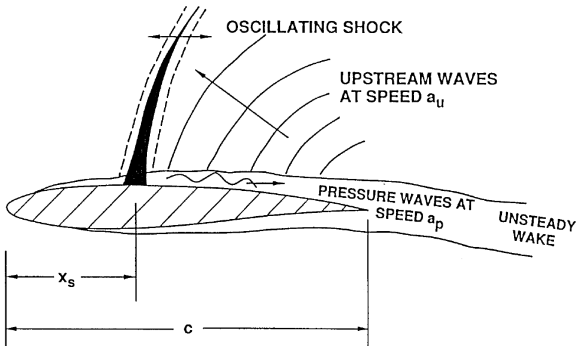

Figure 2.2: Self-sustained shock oscillation mechanism, Lee (1990)

Fig. 2.2 shows how the oscillatory motion of the shock creates the large scale pressure waves that travel downstream through the separated region. When those waves reach the trailing edge they produce small scale waves capable of traveling upstream through the region out of the separated flow. It is believed that these upstream traveling waves, also known as the Kutta waves, are the reason for the self-sustained character of the shock since they collision with it providing energy to maintain the oscillation. Lee stated that the period of the shock movement is the sum of the time it takes for a disturbance from the shock to the trailing edge plus the time it takes for an upstream wave to reach the shock. From reference Lee (2001) the period for a whole buffet cycle is given by,

$$T_P = \int_{x_s}^{c} \frac{1}{U_d} dx - \int_{c}^{x_s} \frac{1}{U_u} dx \tag{2.1}$$

Where U_d is the velocity of the downstream traveling disturbances, U_u is the velocity of the

upstream traveling disturbances and is given by $(1 - M_{loc})a_{loc}$, and M_{loc} is the local Mach number. c represents the trailing edge position and x_s the shock position. U_d was found to be dependent of the Mach number and the angle of incidence and U_u dependent of the frequency. Small scale disturbances travel from the trailing edge to the shock (upstream movement) close to the shear layer between outer flow and separated flow at higher velocities than large scale disturbances, that travel from the shock to the trailing edge (downstream movement) close to the airfoil surface in the detached region and that are produced due to the movement of the shock, Roos (1980). In general, the frequency of the movement of the shock induced disturbances is much lower than the frequency of the shear layer waves, so sufficiently downstream from the airfoil the shock frequencies will not be dominant. This approach is followed by all the studies described next, however, there is some disagreement in the nature and cause of the waves as well as in the computation of the velocities and frequency of such disturbances.

Following the results by Finke (1975) who found upstream traveling pressure waves in the lower surface of a supercritical airfoil at high angle of incidence, Stanewsky and Basler (1990) stated that such pressure waves were capable of creating oscillations in the circulation of the airfoil as they modify the stagnation point and the flow over the upper surface. It was also found a dependency of the buffet frequency with the incidence angle, Mach number and Reynolds number, fact that agrees with later findings by Crouch et al. (2009) and Jacquin et al. (2009). Stanewsky and Basler (1990) also found another important dependency of the buffet mechanisms related to the fluctuations of thickness of the trailing edge boundary layer. They found that the thinning and thickening of the trailing edge boundary layer due to the upstream and downstream shock motion, is in fact the driving mechanism that triggers the upstream traveling pressure waves since it creates an oscillating pressure field.

An explanation about the mechanisms that create the periodic shock oscillation over an airfoil was also attempted by Raghunathan et al. (1998) by means of a computational study over a 18% thickness circular arc airfoil and a NACA0012 airfoil. It was stated in the study that *"the buffet excitation due to shock oscillations is confined to a single frequency"*, assertion that was later demonstrated not to be true. The frequency of buffet depends on the flow parameters, e.g. the Mach and Reynolds numbers and the incidence angle, see refs. Crouch et al. (2009), Jacquin et al. (2009). It was proposed by Raghunathan et al. (1998) that the periodic and self-sustained character of the phenomenon is due to the effect of the downstream and upstream traveling pressure waves found by Lee (1990), the expanding and collapsing character of the separation bubble and the communication between upper and lower surfaces that takes place over the detached wake through the trailing edge.

2.1.4 Recent studies

Studies of buffet from more recent years focus on supercritical airfoils (Brunet et al. (2005), Deck (2005), Crouch et al. (2009), Jacquin et al. (2009), Szubert et al. (2015)), particularly on the OAT15A transonic airfoil developed by ONERA. Jacquin et al. (2009) performed one of the first experimental studies on transonic buffet with this airfoil. His aims were to obtain the exact conditions for the onset of the phenomenon, the physical characterization of the mechanisms that create it and to develop a database that could be used on later numerical

and experimental studies as a reference. The results obtained showed that buffet onset occurs for $Ma = 0.73$ at $\alpha = 3.1°$, so $\alpha = 3.5$ was taken to analyze the results as it is a region of fully developed buffet. In this regime the phenomenon covers almost a 20% of the chord and the separation line over the span is parallel to the leading edge. Fig. 2.3 shows the Schlieren images acquire from Jacquin et al. (2009) for the most upstream and downstream positions of the shock.

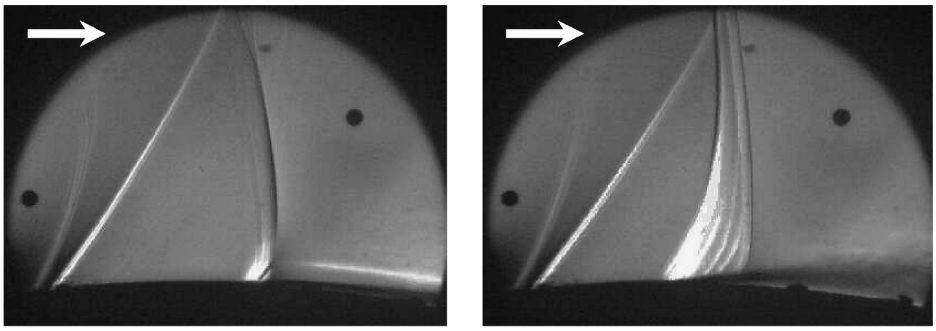

a) b)

Figure 2.3: Schlieren images for OAT15A airfoil at $\alpha = 3.5$ and $Ma = 0.73$, shock most upstream (a) and downstream (b) positions, Jacquin et al. (2009)

The frequency of buffet was found to be near 70 Hz for these conditions ($Ma = 0.73$ and $\alpha = 3.1°$), and it was also found to be dependent of the freestream Mach number. The unsteady pressure measurements showed that there are pressure waves traveling downstream in the upper surface and upstream in the lower one. The speed of the upstream traveling waves was found to be very close to $(a_\infty - U_\infty)$. It was also demonstrated that the phenomenon is time invariant, meaning that the cycles of pressure oscillation are periodic and correlated. LDV measurements corroborated the buffet dynamic description explained before. Jacquin et al. (2009) agrees with Lee's approach of the wave propagation. He states that the buffet process is based on a feedback system in which waves are generated in the shock and travel downstream over the upper surface. At the trailing edge they generate acoustic waves that travel upstream through both the upper and lower surfaces and that eventually hit the shock wave from the front and from behind. He corroborated Eq. 2.1 acknowledging, however, that difficulties arise when trying to compute the propagation velocities of such waves, specially the upstream traveling ones, and that more research is needed on this topic as well.

Deck (2005) arrived to the same conclusions as Lee (1990) for the physical mechanism describing the downstream and upstream traveling waves that maintain the self-sustained character of the oscillation. Furthermore, he established that the origin of the upstream traveling pressure waves is due to an interaction between the shear layer with a sharp edge (trailing edge) as it is explained by Rockwell (1983). Fig. 2.4 shows the numerically computed divergence velocity field over the OAT15A transonic airfoil, both the upstream and downstream pressure waves can be clearly seen traveling through the attached and separated regions respectively.

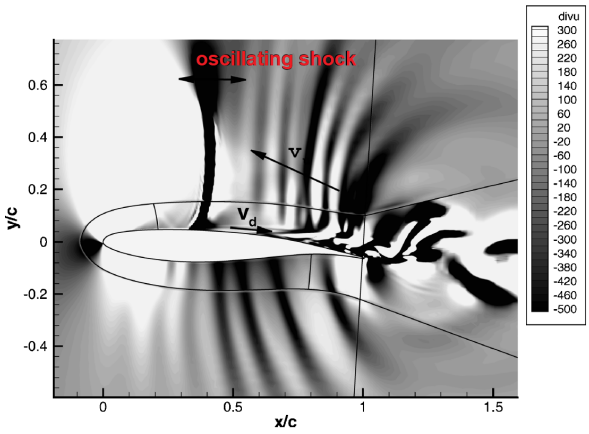

Figure 2.4: Instantaneous divergence of velocity field, Deck (2005)

Deck (2005) agreed with Lee's hypothesis about the time period of the shock movement, i.e. Eq. 2.1. The main difference is that Deck (2005) attributes the origin of the upstream traveling waves to the large structures originated in the shear layer impinging on the sharp trailing edge. Furthermore, a theoretical study based on global stability analysis carried out by Crouch et al. (2009) reached the conclusion that the shock oscillation is phase locked to the shear layer oscillation downstream from the shock. This theoretical approach is in good agreement with the results obtained by Jacquin et al. (2009). The stability analysis shows that the critical incidence angle for buffet onset decreases with increasing Mach number and, on the other hand, the buffet frequency increases for increasing Mach number, this tendencies were experimentally found by Jacquin et al. (2009). Crouch et al. (2009) stated that as the shock moves downstream the shear layer gets closer to the airfoil surface since velocity perturbations in the shock and in the shear layer are in phase, this in turn is in agreement with the fact that in the downstream movement the boundary layer gets thinner and reattachment occurs. Again this study agrees in its results with the mechanism of upstream and downstream traveling waves proposed by Lee (1990).

Hartmann et al. (2013) performed an experimental study over a supercritical airfoil to support the buffet mechanism model from Lee (2001) based on the upstream traveling Kutta waves. The aerodynamic model was the DRA2303 airfoil with 14% relative thickness, 200 mm chord length and fixed transition at $x/c = 5\%$. They studied the pressure waves propagation in the region after the shock using both pressure measurements and particle image velocimetry. Additionally, they used an artificial sound source to interact with the buffet frequency. A cross correlation of pressure and velocity fields in the region after the shock was carried out that showed the upstream and downstream traveling waves velocity for $Ma_\infty = 0.73$ and $\alpha = 3.5°$, see Fig. 2.5.

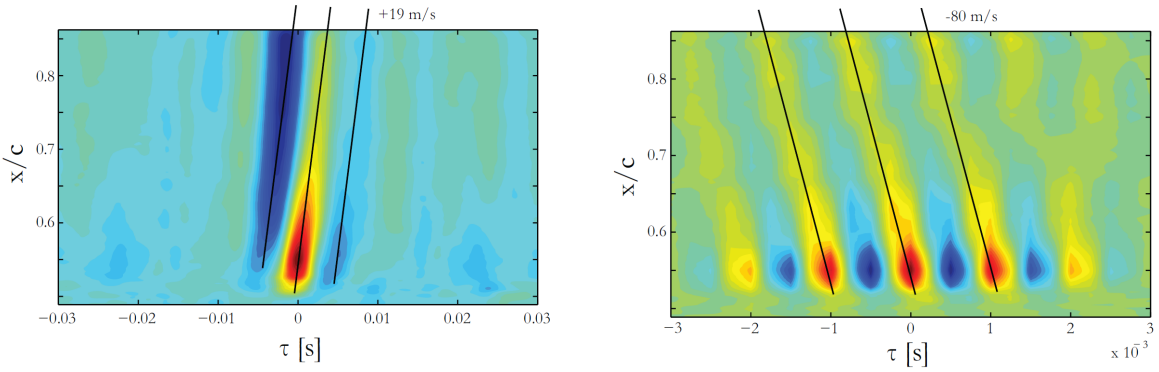

Figure 2.5: Contours of the normalized absolute velocity correlation, low-pass filtered (left) and high-pass filtered (right), Hartmann et al. (2013)

The strong correlation between the measured and the computed frequencies using the approach by Lee (2001) (see Eq. 2.1) led to the main conclusion from this analysis, i.e. the mechanism that mainly sustains buffet is the feedback loop that exist between the shock motion and the noise generation from the trailing edge. The downstream traveling waves impinge in the trailing edge, creating new pressure waves that expand radially and hit the shock wave creating a local increased pressure gradient next to the shock. The shock wave displaces upstream due to this, which at the same time changes the conditions at the trailing edge. Hartmann et al. (2013) also stated that the noise pressure level emitted from the trailing edge depends highly on the size of the separation region due to its influence over the vorticity gradient normal to the surface. Such noise pressure level change influences directly the strength of the upstream traveling waves. At the same time this is translated into a periodic strength gradient of the feedback that the shock wave receives from the trailing edge and, hence, this can be the cause for the oscillatory motion.

Another recent study is the one performed by Szubert et al. (2015), a conceptual and computational work to analyze the mechanisms and characteristics of buffet phenomenon over the OAT15A transonic airfoil based on the experiments from Jacquin et al. (2009). This study complements previous studies focused on describing the shock movement and the flow field properties by focusing instead on the dynamics of three main interactions, namely,

- Shock wave with wake vortices
- Shock wave with boundary layer
- Wake vortices with shear layer

Where the wake vortices correspond to Von Karman instabilities and the shear layer to Kelvin-Helmholtz instabilities. It was shown by Szubert et al. (2015) in a computational study that in the absence of the Von Karman perturbations the buffet phenomenon was importantly mitigated and finally disappeared. Bouhadji (1998) showed that the Von Karman instability (mode I) originates in the wake and travels towards the trailing edge.

When the buffet instability (mode II) appears there is a strong interaction between both modes and mode II is sustained by mode I. The study of these interactions is in line with the progress made by Lee (2001) with its approach involving the Kutta waves. The results obtained by Szubert et al. (2015) fit pretty accurately with the physical explanation given by Jacquin et al. (2009) of the movement mechanism of the shock wave along the chord of the airfoil at buffet conditions, with the additional information that Von Karman instabilities were observed to occur during the upstream movement, giving rise to wake vortex shedding. These instabilities were attenuated during the downstream movement of the shock wave.

There is an important difference between symmetric and non symmetric airfoils, that apply to the present study for the NACA0012 and the OAT15A models. Szubert et al. (2015) found that at high subsonic Mach numbers and moderate angles of incidence, the NACA0012 develops two shock waves and separation occurs alternately between the upper and lower surface, so there is always a thick wake between two shear layers. This fact generates vorticity gradients that induce the Von Karman mode (mode I). On the other hand, the OAT15A only develops a shock wave on the upper side, so the wake disappears intermittently during the reattachment part of the cycle, hence making the Von Karman mode disappear. In fact, an spectral analysis showed that the Von Karman mode frequency (2.6 kHz) and the 33^{rd} buffet harmonic frequency (2.58 kHz) were close enough to cause synchronization of both modes. Furthermore, synchronization was found as well between the vortex shedding due to Von Karman and Kelvin-Helmholtz instabilities, so it was concluded that, indeed, the interaction with these instabilities could create an amplitude modulation of the buffet phenomenon. No physical explanation was given about how the synchronization is possible with such high difference in time scales (more than 1 order of magnitude). The spectral analysis showed that when the shock starts its upstream movement vortices were shed at 4000Hz at small amplitude (Kelvin-Helmholtz instabilities) while during the upstream travel the vortices were shed at 2600Hz (Von Karman instabilities). In the most upstream position the vortices were shed again at 4000Hz and during the downstream travel no separation nor vortex shedding occurred.

2.2 Buffet onset conditions

The buffet onset conditions are the values of the main aerodynamic parameters for which buffet first starts occurring. Usually, these conditions refer to the Mach number, the Reynolds number and the steady mean angle of attack of the airfoil. The finding of these conditions has been one of the main targets of most buffet numerical and experimental investigations for more than forty years, see Finke (1975), Seegmiller et al. (1978) and Levy Jr (1978).

McDevitt and Okuno (1985) and Deck (2005) showed that buffet onset mechanisms are not related with any fluid-structure interaction, but they can cause structural vibrations as the so-called phenomenon buffeting. In general, the phenomenon is tightly related to shock induced separation at the shock foot and with feedback mechanisms from the trailing edge that produce the self-sustained motion. Several methods have been used to determine buffet onset conditions since the phenomenon was first discovered, see Lee

(2001). The divergence of the trailing edge pressure method on a standard airfoil was first used by Pearcey (1958). Divergence occurs when the separation bubble at the shock foot grows and bursts, joining the trailing edge separation region. However, a later study by Roos (1980) demonstrated that this method is not suitable for supercritical airfoils since the divergence of the trailing edge pressure does not evolve similarly to buffet onset. Other methods include the unsteady normal force over the airfoil calculated with pressure measurements or force balances and also boundary layer theory, see Lee and Tang (1989).

The present project focuses in two aerodynamic models, the standard NACA0012 and the supercritical OAT15A. There are several studies in the literature that cover the buffet onset conditions of these airfoils both experimentally and numerically. These studies are used to obtain the range of properties for which buffet develops and that can be used as reference for the experiments.

2.2.1 NACA0012 airfoil

Roos (1980) carried out an experimental study over a supercritical Whitcomb airfoil and a standard NACA0012 at transonic speeds conditions and penetrating into buffet regions for varying c_L and freestream Ma numbers. Pressure, lift force and shock location measurements were made in order to study the unsteady effects and analyze the buffet onset conditions. For the NACA0012 airfoil, a model of 15.24 cm chord and free transition was used. Buffet was found by varying the Mach number at constant $c_L = 0.42$ and $Re_c = 2 \cdot 10^6$. Under these conditions separation first appears at $Ma_\infty = 0.74$ in the form of a separation bubble at the shock foot. For increasing Ma number the bubble grows towards the trailing edge for $Ma_\infty = 0.77$, finally joining it and bursting into a whole separated region at $Ma_\infty = 0.80$. A later experimental study by McDevitt and Okuno (1985) focused on a NACA0012 model with 20.3 cm chord and free transition. In this experiment hot wire anemometry, steady and unsteady pressure measurements were made in order to analyze the unsteady aspects of the flow, in particular, the buffet onset conditions at low transonic Mach numbers for varying angle of attack, Reynolds number and Mach number. The onset angles of attack for different Reynolds numbers (1 to 10 million) and Ma numbers (0.7 to 0.8) were obtained. Special interest was paid to the onset values at high Re numbers since they are more representative of free flight conditions, i.e. $Re \approx 10^7$. Fig. 2.6 shows the experimental results where buffet onset was encountered (solid line).

On the other hand, numerical results for the buffet onset prediction are very sensitive to the numerical models, specially to the turbulence model. Fig. 2.6 shows a comparison between the buffet onset conditions obtained in the previous experimental study from McDevitt and Okuno (1985) (solid line) and the conditions obtained with different turbulence models, namely SA model (crosses) and the non linear $k - \omega$ model (squares), see Barakos and Drikakis (2000). *SIO* stands for Shock Induced Oscillations, i.e. buffet. As it is observed the numerical results fit pretty well with the tendency of the experimental ones, but important differences can be seen between both numerical approaches. Another numerical study from Raghunathan et al. (1998) concluded that buffet for the NACA0012 was fully developed for $\alpha = 6°$, $Ma_\infty = 0.7$ and $Re = 10^7$. Comparing this result with the experimental data from

McDevitt and Okuno (1985) an important difference can be seen in the incidence angle, where $\alpha = 6°$ seems to be overestimated.

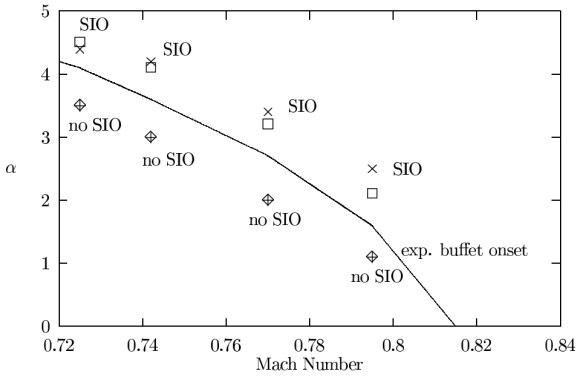

Figure 2.6: NACA0012 experimental and numerical buffet onset conditions at $Re = 10^7$, McDevitt and Okuno (1985) and Barakos and Drikakis (2000)

2.2.2 OAT15A airfoil

For the OAT15A supercritical airfoil, several experimental and numerical studies exist that have studied the buffet onset and the characteristics that define the physical behavior of the phenomenon. The experimental study from Jacquin et al. (2009) is one of the most recent and complete ones. In this study oil visualization, sublimating products, Schlieren visualization, Laser Doppler Velocimetry (LDV) and steady/unsteady pressure transducers were used over a OAT15A model of 230 mm chord length and 780 mm span length. Boundary layer transition was forced by a tripping strip at a distance of 7% chord from the leading edge. The experiments were divided in three sets with fixed $Re = 3 \cdot 10^6$, $P_{st} = 10^5$ Pa and $T_{st} = 300$ K,

- Constant $Ma_\infty = 0.73$ and varying $\alpha = 1.36° - 3.9°$
- Constant $\alpha = 3°$ and varying $Ma_\infty = 0.7 - 0.75$
- Constant $\alpha = 3.5°$ and varying $Ma_\infty = 0.7 - 0.75$

Most of the analysis was done for the first set. It was found that the buffet onset occurs at $\alpha = 3.1°$ and $Ma_\infty = 0.73$ for this particular case. At $\alpha = 3°$ no unsteady behavior is observed in the flow; for $\alpha = 3.1°$ the first unsteady perturbations are detected, weak in amplitude; for $\alpha = 3.25°$ the pressure signal is periodic but with changing amplitude in each cycle, which means that the phenomenon is not yet fully established; finally, for $\alpha = 3.5°$ the phenomenon is fully developed and it covers about 20% of the chord length for $\alpha = 3.9°$, with a traveling wave from $x/c = 0.3$ to $x/c = 0.48$. This is the reason why most part of the study was focused in this particular configuration of $Ma_\infty = 0.73$ and $\alpha = 3.5°$, so that the buffet phenomenon was visible and fully developed but not yet near the upper limit

where it disappears due to a too large incidence angle. The study also demonstrated that the oscillation frequency is not constant. Instead, it grows for increasing Mach number as was measured $f = 65Hz$ for $Ma_\infty = 0.72$ and $f = 77Hz$ for $Ma_\infty = 0.74$.

Most theoretical and numerical studies of buffet over the OAT15A model are based on the experimental results by Jacquin et al. (2009) (see Crouch et al. (2009), Brunet et al. (2005), Deck (2005) and Szubert et al. (2015)). Mostly, these studies use the experimental data to verify different numerical schemes and theoretical approaches. For instance, global-stability theory is applied by Crouch et al. (2009) to predict buffet at conditions near buffet onset. The theoretical results and the experimental data show agreement for the onset of buffet and the general flow structure, see Fig. 2.7.

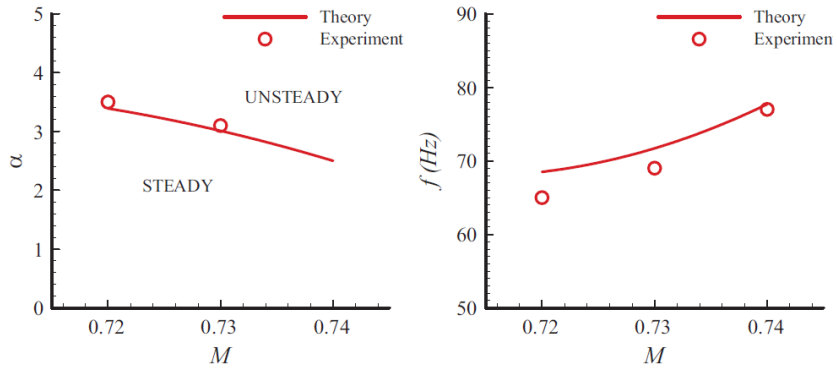

Figure 2.7: OAT15A buffet onset conditions (left) and oscillation frequency at $\alpha = 3.5$ (right), see Crouch et al. (2009)

Chapter 3

Experimental Setup

This chapter presents the experimental setup used for the study and analysis of transonic buffet over an airfoil. The facilities chosen for this experimental project are located in the High Speed Lab (HSL) of the Aerospace Faculty at Delft University of Technology. The wind tunnel specifications, the aerodynamic models descriptions, the main test conditions and the measurement techniques that were used are described in detail in the following sections. The experimental techniques sections focus on the presentation of the actual setups that were used for this project instead of the explanation of the working principles and physical and mathematical backgrounds of the techniques. For further information about any technique in particular, the reader is referenced to specific manuals and practical guides available in the open literature.

3.1 Test facility

The transonic-supersonic wind tunnel TST-27 at the High Speed Lab of TU Delft Aerospace faculty was used for the experiments, a blow down type facility able to generate flows ranging in Mach number between 0.5-0.85 (high subsonic and transonic regimes) and 1.15-4.2 (supersonic regime) in the test section. The supersonic Mach numbers are set by an adjustable throat with flexible nozzle walls while the subsonic Mach is controlled by a variable choke section in the outlet diffuser that corrects small deviations. This control system enables the Mach variation during a run. The maximum running time of the test is about $\sim$ 300 seconds and it is designed for high stagnation pressures. The maximum Reynolds number for transonic conditions that can be achieved is near $\sim$ 38 million per meter.

The wind tunnel is connected to a 300 m^3 storage vessel. This vessel typically stores at a pressure of 40 bars and supplies dried and filtered air up to 20 bars due to structural fatigue reasons. The drying system ensures a moisture of about 10 parts per million of vapor whereas $5\mu m$ high-pressure dust filters are installed between vessel and wind

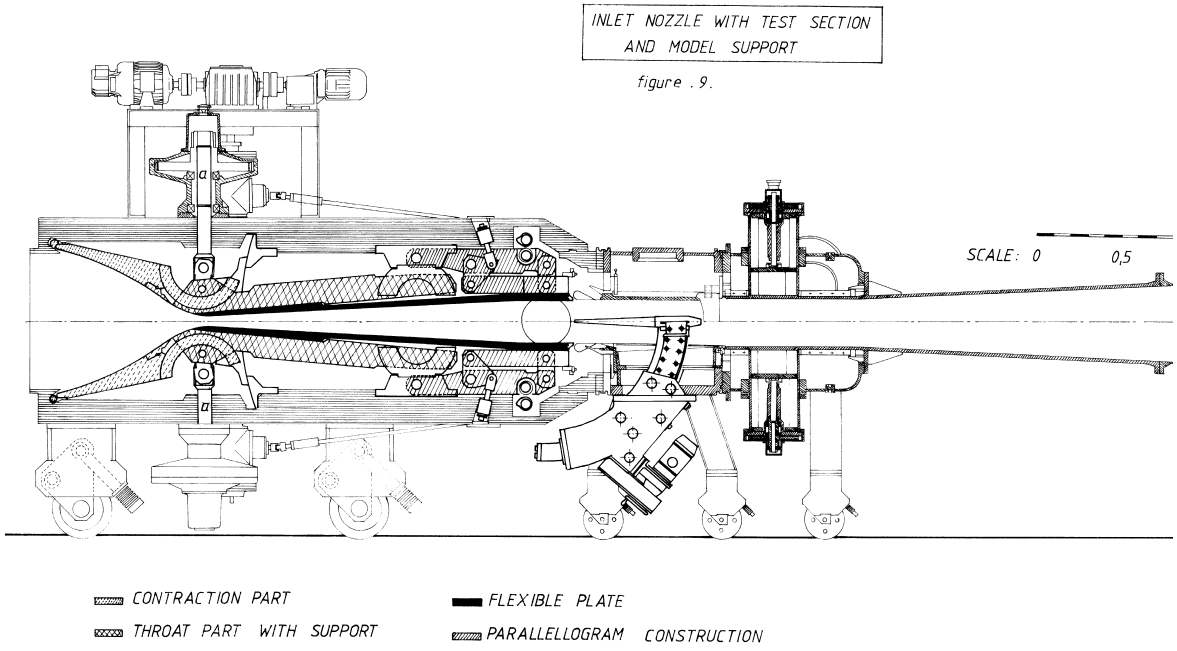

Figure 3.1: TST-27 wind tunnel

tunnel to avoid dust erosion. The vessel also contains a heat regenerator that consists of a bed of ceramic pebbles that maintains a nearly constant temperature.

The TST-27 is comprised of four main parts. The settling chamber or reservoir, that can be set at pressures of 2 to 4 bars, has access for seeding particle system and ensures a low turbulence level of around 1%. The reservoir is connected to the adjustable nozzle that adjusts the supersonic Mach numbers. The tunnel consist of several modules downstream from the nozzle section that can be connected by quick-lock coupling and that allow to use two different test sections, one transonic with slotted walls and one supersonic with solid walls.

Despite the availability of the slotted walls test section and the detrimental influence of solid walls in transonic regime, the solid walls test section was chosen for the experiments. The main reason is that the transonic test section may not be optimum for the PIV technique and also that it has 2 overlapped windows (one for the test section and another one for the plenum and adjacent to the first), which is very detrimental for the optics (illumination and imaging) of the PIV measurements. Also logistic reasons were involved in the decision, since the mounting and dismounting of the test section for every experimental campaign is a very hard and time consuming task for the technicians. The solid walls test section has dimensions of 280×250 mm (Width x Height) and lateral optical access through two glass windows of 160 mm diameter. The windows are equipped with the appropriate mechanical orifices and bearings for the installation of the airfoils, that need to be placed exactly in between the glass surfaces. Both windows are connected to a mechanical control system for the angle of attack that is regulated manually. In order

to avoid torsional loads that can break the glass, it is of paramount importance that the windows are properly aligned with each other and also with the angle of attack control system.

The last part of the tunnel is the diffuser that connects the test section with the exterior and decelerates the flow. It contains the variable choke, see Figs. 3.2 and 3.3, that is in charge of controlling subsonic Mach numbers and correcting small Mach deviations during the run by adjusting the cross sectional area.

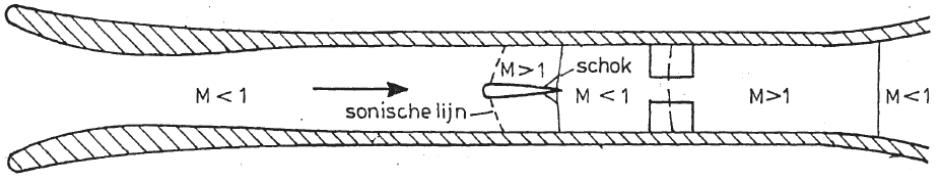

Figure 3.2: TST-27 in subsonic flow regime, Bannink (1987)

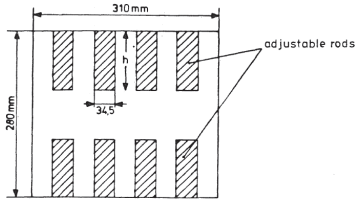

Figure 3.3: Detailed choke mechanism, Bannink (1987)

3.2 Aerodynamic models

The airfoils chosen for this project are the NACA0012 as a representative model for a conventional symmetric airfoil and the supercritical OAT15A airfoil from ONERA as a representative model for a non-symmetric transonic airfoil more suitable for the Mach number range to be analyzed and for the expected flow phenomena. A comparison between these two characteristic models is intended in order to study the differences in the flow behavior due to the model geometry. The reason to choose the NACA0012 is that it is a widely used airfoil about which a lot of data is available. The choice for the supercritical OAT15A is motivated due to the fact that it is the most used airfoil in recent experimental and numerical studies on the buffet topic from previous years. The most current experiments and theories have been evaluated over this specific model and there is also data available for comparison, for instance in the experiments by Jacquin et al. (2009).

The aerodynamic models are manufactured on steel and their dimensions are 100 mm of chord length and 280 mm of span, which gives an aspect ratio $AR = 2.8$, exactly fitting the width of the test section and allowing a two-dimensional analysis. The NACA0012 has a 12% thickness-to-chord ratio at $x/c = 32\%$ from leading edge and a trailing edge thickness of 0.7% relative to the chord, whereas the OAT15A has a 12.3% thickness-to-chord ratio and a trailing edge thickness of 0.75%. The angle of attack of the model is set by means of the wind

tunnel angle of attack control mechanism and using a digital level box with an error of $\pm 0.05°$.

Figure 3.4: OAT15A airfoil

Figure 3.5: NACA0012 airfoil

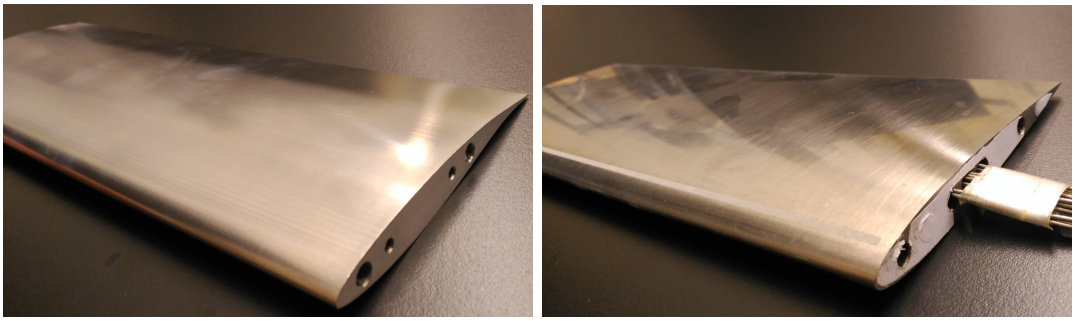

Figure 3.6: Steel aerodynamic models of OAT15A (left) and NACA0012 (right)

3.3 Transition trips

Two types of transition trips were tested, zig-zag trips and carborundum (SiC) trips, placed at $x/c = 7\%$, with a total width of 2 mm for the Carborundum trips and 11 mm for the zig-zag. The main objective was to find the best device to trigger transition of the boundary layer over the airfoils. Three main considerations must be taken into account for the design of grit type transition trips as described in Braslow et al. (1966), namely,

- The roughness element has to be narrow. Wide bands increase drag unnecessarily.
- Roughness has to be homogeneously and sparsely distributed, avoiding high density areas since they will act as a two dimensional trip, i.e. a step.
- The glue should not form thick or multiple layers, to avoid ridges that will act as two dimensional trips.

For the oil flow visualization measurements, the Carborundum trips used were of 4 different sizes, namely Carborundum 150, 320, 400 and 500, and also a zig-zag transition trip. For

the Schlieren and PIV measurements only the Carborundum 500 transition trip was used, as it was demonstrated to be the best option.

The carborundum numeric label refers to the amount of particles that fit in a surface unit, so the higher the number is, the finer the particles are, see Table 3.1. The zig-zag transition trip has a thickness of 0.2 mm, and its size and shape is presented in Fig. 3.7.

ANSI Grit	Particle size $[mm]$
150	0.075
320	0.0295
400	0.0183
500	0.0139

Table 3.1: Particle size of the ANSI Grits used for the transition trips

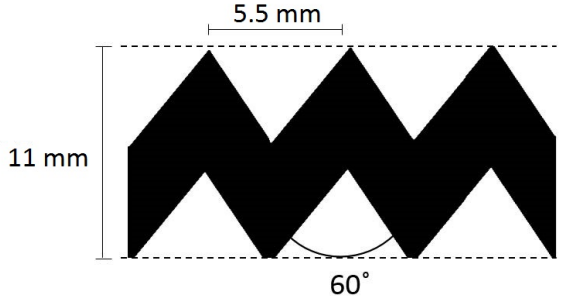

Figure 3.7: Zig-zag strip dimensions

3.4 Experimental campaigns & Test conditions

The experiments for the present project were divided into four experimental campaigns, the first set (campaigns 1 and 2) was performed on the NACA0012 model and the second one (campaigns 3 and 4) mainly on the OAT15A supercritical model. In both cases the objectives of the sets were the same and hence, the approach and methodology performed in the first set was reproduced in the second one. Furthermore, the test matrices were similar for both airfoils since the conditions for buffet are achieved in a specific range of aerodynamic parameters (i.e. Mach number, angle of attack, Reynolds number) that is only slightly affected by the geometry differences between the models tested.

Each campaign of a set had a specific purpose and hence, a different approach and experimental techniques were used depending on the aimed results. The first campaign had the main goal of finding the range of Mach number and angle of attack values for a fixed Reynolds number for which buffet is fully developed by means of Schlieren visualization. This result is needed as an input for the second campaign. The following objectives were

also pursued in the first campaign,

- Influence of the varying aerodynamic parameters (Ma, α) over buffet development.
- Influence of the nature of the boundary layer over buffet.
- Influence of the geometry of the airfoil over buffet
- Effect of the presence of the laser probe over buffet (needed for PIV measurements), placed downstream of the airfoil.

Oil and time resolved Schlieren visualization were used to fulfill these objectives in the first campaign of both sets. The Schlieren technique allows for a visual analysis of the overall flow field and the flow features taking place. Since it is time resolved also an spectral analysis can be performed about the shock motion in order to establish the conditions for which buffet is more fully developed. The oil visualization allows the analysis of the features that take place near the surface of the airfoil, as for instance the nature and location of transition, a rough estimate of the position of the shock wave and the effect of the tunnel solid walls over the flowfield. Once the conditions for fully developed buffet have been set, they are reproduced in the next campaign. The second campaign is performed using time resolved particle image velocimetry (PIV) technique. Its main purpose is to obtain the velocity flow field about the airfoil in order to analyze its physical behavior and development in time as well as the features that characterize the shock motion and create the sustainable cyclic movement.

3.4.1 Test conditions

The experimental conditions in the wind tunnel are given by three main parameters, namely the total pressure in the reservoir, the Mach number in the test section and the total temperature in the reservoir. The first two are controlled by the wind tunnel operator, whereas the total temperature is just measured before the run. The Mach number in the test section is computed using static and total pressures, obtained ahead of the test section in the undisturbed region, see Bannink and Bakker (1983). Once these parameters are set and known, the rest of the test conditions can be computed assuming an isentropic expansion from the reservoir to the test section and using Sutherland's law of viscosity, see Appendix B. Table 3.2 shows the results of these calculations for a reference test case.

The parameters of velocity and Mach number used throughout the present document are not corrected because the corrected parameters would be necessary only for a comparison with the cases studied in the literature. Nevertheless, a rough first order estimation of the corrected Mach number is computed here. The expression for the corrected parameters is as follows,

$$U_{corr} = U_\infty \cdot (1+\epsilon), \qquad M_{corr} = M_\infty + M_\infty \cdot \epsilon \cdot \left(1 + \frac{\gamma-1}{2} \cdot M_\infty^2\right) \tag{3.1}$$

Parameter	Symbol	Value	Units
Free stream Mach	Ma_∞	0.7	-
Total temperature	T_0	283	$[K]$
Total pressure	P_0	1.98	$[bar]$
Static temperature	T_s	257.7	$[K]$
Static pressure	P_s	1.43	$[bar]$
Density	ρ_∞	1.95	$[kg/m^3]$
Dynamic viscosity	μ_∞	$1.58 \cdot 10^{-5}$	$[kg/(ms)]$
Free stream velocity	U_∞	225.3	$[m/s]$
Unit length Reynolds	Re/L	$\sim 2.8 \cdot 10^7$	$[1/m]$

Table 3.2: Reference test conditions

Where U_{corr} and M_{corr} refer to the actual conditions that would be achieved in free-flight. The correction parameter ϵ is obtained as,

$$\epsilon = \epsilon_m + \epsilon_w, \tag{3.2}$$

where ϵ_m accounts for the model blockage and ϵ_w for the wake blockage. Note that in the present case, under unsteady buffet conditions the wake develops in time changing size and shape and it is highly affected by the presence of a shock wave, i.e. a proper estimate may not be possible with the available data. The blockages coefficients are computed as,

$$\epsilon_m = \frac{\pi^2}{12}\left(\frac{t}{h}^2\right)\lambda \cdot \left(1 + 1.2 \cdot \beta\frac{t}{c}\right) \cdot \left(1 + 1.1 \cdot \alpha^2\frac{c}{t}\right), \tag{3.3}$$

$$\epsilon_w = \frac{1}{4}\frac{c}{h}c_d, \tag{3.4}$$

where t stands for the airfoil thickness, h for the test section height, λ is an airfoil constant based on geometrical parameters, equal to 3.8 for the NACA0012 airfoil, c is the chord length, α accounts for the angle of attack of the airfoil and c_d the drag coefficient. Nevertheless, the same $\lambda = 3.8$ and $c_d = 0.02$ values will be applied for both airfoils even tough they belong to the NACA0012. Note that this correction factor is valid for incompressible cases, if compressibility effects should be added, then the Prandtl-Glauert rule is necessary,

$$\epsilon_{m_c} = \frac{\epsilon_m}{\beta^3} = \frac{\pi^2}{12}\left(\frac{t}{h}^2\right)\frac{\lambda}{\beta^3} \cdot \left(1 + 1.2 \cdot \beta\frac{t}{c}\right) \cdot \left(1 + 1.1 \cdot \alpha^2\frac{c}{t}\right), \tag{3.5}$$

$$\epsilon_{w_c} = \frac{\epsilon_w}{\beta^2} = \frac{1}{4}\frac{c}{h}\frac{c_d}{\beta^2}, \tag{3.6}$$

where $\beta = \sqrt{1 - M_\infty^2}$. Finally the total correction factor to be applied is,

$$\epsilon = \epsilon_{m_c} + \epsilon_{w_c} = \frac{\pi^2}{12}\left(\frac{t}{h}^2\right)\frac{\lambda}{\beta^3} \cdot \left(1 + 1.2 \cdot \beta\frac{t}{c}\right) \cdot \left(1 + 1.1 \cdot \alpha^2\frac{c}{t}\right) + \frac{1}{4}\frac{c}{h}\frac{c_d}{\beta^2}. \tag{3.7}$$

Note that this is an average correction, meaning that it is used in all the flow region under study since it does not consider local effects, hence appropriate to be used for integral

quantities. These corrections consider the blockage of the model and the wake, accounting for the angle of attack. Nevertheless, they are vague since only the blockage effect of the NACA0012 airfoil is used, and assumed to be similar as to the OAT15A. It is expected then that the real Mach number is even higher than the corrected values obtained from this rough estimation. Table 3.3 shows the corrected values that correspond to the Mach numbers and angles of attack used in the present experiments. Note that they are only listed here, and that the values used throughout the document are not corrected. For further information about wall corrections see Ewald (1998).

α \ Ma_∞	0.65	0.68	0.70	0.73	0.75	0.77	0.80
0	0.665	0.698	0.720	0.754	0.777	0.800	0.838
2	0.666	0.698	0.720	0.754	0.777	0.801	0.838
3.5	0.666	0.698	0.721	0.754	0.778	0.801	0.839
4	0.666	0.699	0.721	0.755	0.778	0.802	0.839

Table 3.3: Corrected Mach numbers

3.4.2 Test matrices

The experiments of this project are divided in four different campaigns. In all of them the reservoir pressure is kept constant $P_0 = 2$ bar, and variations in the angle of attack of the airfoil ($\alpha = 0, 2, 4°$ for NACA0012, $\alpha = 0, 2, 3.5°$ for OAT15A) and the test section Mach number ($Ma = 0.65 - 0.80$) are performed. Table 3.4 shows a summarize test matrix in which the main conditions of all the tests can be found. For further information, the complete test matrices of the experiments can be found in Appendix A.

Campaign	Airfoil	Technique	α	Ma
1	NACA0012	Sch.	0	0.65, 0.70, 0.75, 0.78, 0.80
			2	0.65, 0.70, 0.73, 0.75, 0.77, 0.80
			4	0.65, 0.68, 0.70, 0.72, 0.75, 0.80
	No model	Sch.	-	0.75, 0.80
2	NACA0012	PIV	0	0.78
			2	0.70, 0.75
			4	0.70, 0.75
3	OAT15A	Sch.	0	0.73, 0.75, 0.77, 0.80
			2	0.65, 0.67, 0.70, 0.73, 0.75, 0.77
			3.5	0.63, 0.65, 0.67, 0.69, 0.70, 0.71, 0.73, 0.75
	No model	Sch.	-	0.70, 0.75, 0.80
4	OAT15A	PIV	0	0.78
			2	0.70, 0.73
			3.5	0.70, 0.73

Table 3.4: Summarized test matrix

3.5 Schlieren visualization

Schlieren photography is a non-intrusive flow visualization technique used to obtain diagnostic information of the flowfield based on refraction index measurements. This technique consists in general of a simple setup compared to other techniques, and it gives direct qualitative information of the flow field. The density of a fluid is function of its refractive index, so Schlieren is normally most commonly used for compressible flows, heat convection phenomena and acoustics, since the density gradients are usually associated to compressible effects, thermal effects and mixing of fluids with different densities. Schlieren photography relies on the principle of light refraction due to variations of the refraction index, phenomenon that is described by Snell's Law as,

$$n_1 \cdot sin\alpha_1 = n_2 \cdot sin\alpha_2 \tag{3.8}$$

Where 1 and 2 refer to different physical mediums, n_i is the refraction index and α_i is the incidence angle of the light beams. This equation states the change in the direction of light when entering a medium with a different refraction index as depicted in Fig. 3.8.

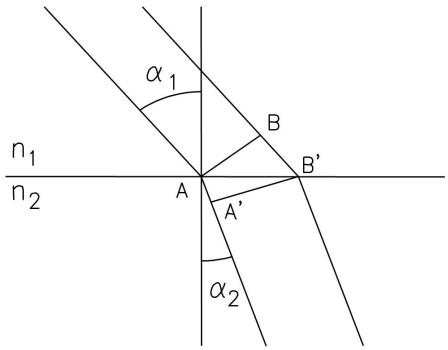

Figure 3.8: Refraction effect of light

In this experimental technique the refraction index gradients are directly caused by density gradients in the flow field. The general relation between a fluid, liquid or gas, and its refractive index is given by the Clausius-Mosotti equation, a relation that involves certain molecular constants of the fluid and which is not very handy to work with. A simpler form is known as the Gladstone-Dale relation for gases, Eq. 3.9, that shows the dependency of the refraction index n as a function of the density and wavelength λ for a specific gas.

$$n(\rho, \lambda) - 1 = K(\lambda) \cdot \rho \tag{3.9}$$

Where $n - 1$ is known as the refractivity of a fluid, $K(\lambda)$ is the Gladstone-Dale constant dependent on the wavelength and ρ is the local density (typically $n_{air} = 1.0003$). So variations in the density field are translated into variations of the refraction index, changing the direction of the light beams that cross that region. The measured quantity in a Schlieren system is the gradient ∇n that in the flow field corresponds to $\nabla \rho$, so the light intensity gradients $(\Delta I/I)$ obtained from the Schlieren images are directly related to the density gradients in the flow

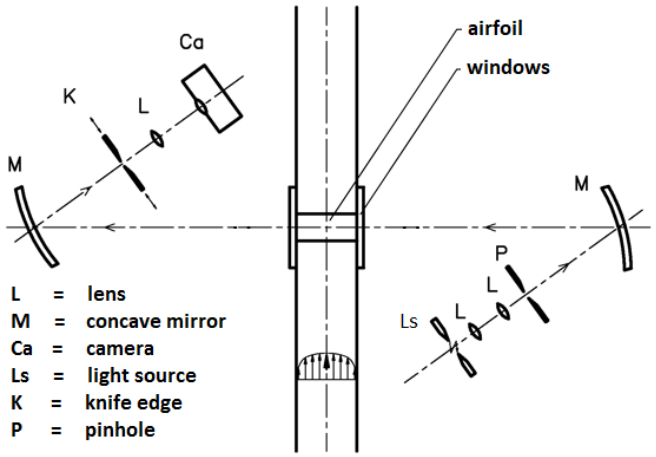

Figure 3.9: Schematic representation of a Toepler Schlieren system

field as,

$$\frac{\Delta I}{I} \propto \frac{K f_2}{s} \int_{z_1}^{z_2} \frac{\partial \rho}{\partial x} dz, \tag{3.10}$$

where f_2 is the focal length of the Schlieren concave mirrors and s is the light offset.

3.5.1 Schlieren system arrangement

Figure 3.9 is an schematic representation of a Toepler Schlieren system. The light beams from a incoherent light source go through two biconvex lenses and a slit or pinhole, which in the present experiments is covered with transparent adhesive tape to obtain diffused light. The pinhole is placed in the light beam waist, in such position that the reflection on the first concave mirror forms parallel beams that go through the test section and are reflected into the second concave mirror. From this mirror they are sent to the Schlieren knife edge, which is placed at the focal point so that the whole light beam is practically converged to a light spot, and then to another biconvex lens and the recording system. In the present experiments a set of small mirrors to control the direction of the light beams towards the concave mirrors was used for convenience. The recording system used the Imager Pro HS 4M High speed camera from LaVision, with a total resolution of 2016x2016 pixels up to 1.3 kHz, a maximum frame rate of 150 kHz and a pixel size of 11x11 μm.

The Schlieren system used for the experimental campaigns of this project is a Toepler system as the one presented in Fig. 3.9 with two small mirrors added to redirect the light beam towards the big concave mirrors. The light comes from a continuous light source, chosen due to the high acquisition frequencies. The Schlieren knife edge is placed in vertical position so that the horizontal density gradients of the flow field are obtained. It slightly covers a $5 - 10\%$ of the inner light circle so that the pressure waves downstream from the shock wave can be acquire. The pinhole has an aperture of 2 mm and is covered with

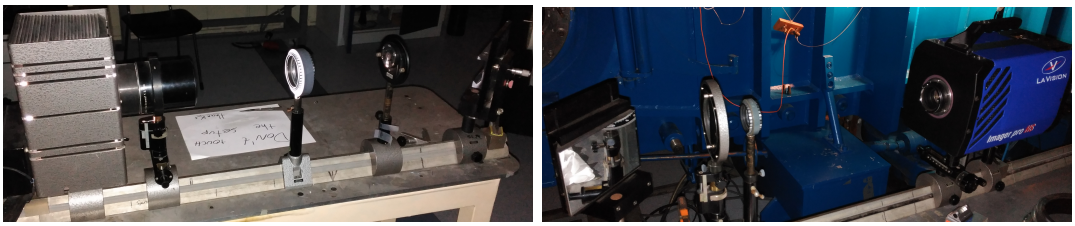

Figure 3.10: Schlieren system arrangement

transparent tape to enhance the image quality. An exposure time $t_{exp} = 10\ \mu s$ is used for the recording. The acquisition frequencies chosen vary between 1500 Hz, 3000 Hz, 4000 Hz and 8000 Hz so that a better spectral analysis of the shock motion can be performed from the instantaneous images.

Parameter	Value	Unit
Light source	Continuous	-
Pinhole aperture	2	$[mm]$
Mirror focal length	3.5	$[m]$
Knife	Vertical	-
Exposure time	10	μs
Frame rates	1.5, 3, 4, 8	$[kHz]$
Camera resolution	864x864	$pixel$
Measurement time	1	$[s]$

Table 3.5: Parameters of Schlieren configurations

An important intrinsic effect of the Schlieren technique that needs to be taken into account is the three dimensional effect. This is a line-of-sight method, so the results obtained from this technique are two-dimensional, however the light beam goes through the whole third dimension (span wise direction) of the test section. This means that all the phenomena is integrated along the light direction through the fluid as part of the two-dimensional map. The effect of this issue over the results can be clearly observed in any of the following images. While it is known that the thickness of a normal shock wave is of the order of 1 mm, the images show thicknesses of $\sim$ 20 mm. The reason is that the normal shock is not exactly parallel to the span wise direction and as result a thickening effect is observed. This effect can be enhanced by reducing the sensitivity of the system.

3.5.2 Setup modifications and their effect

Knife depth and orientation

Following the light path presented in figure 3.9, when the beam crosses the test section it is deflected due to the density gradients occurring that create a gradient in the refraction index

of the medium. The Schlieren knife edge is placed in such a way that it will block part of the deflected light beams by cutting off part of the light spot. The sensitivity of the system depends precisely on the percentage of the spot that is blocked. From the experiments it was observed that the light spot is actually formed by two different parts, an outer part and a brighter inner part.

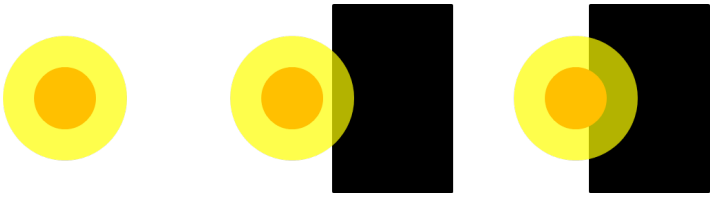

Figure 3.11: Schlieren knife edge positions

Figure 3.11 shows the light spot morphology (left) and two different positions of the knife edge, *open knife*, covering part of the outer circle (center), and *deep knife*, covering part of outer and inner circles (right). A great difference in the system sensitivity can be observed between these two configurations by looking at figure 3.12 that represents a test run with the exact same aerodynamic conditions of Re, Ma and α. The left image was obtained with the *open knife* configuration, whilst in the right image the *deep knife* configuration was used. Note that the sensitivity is decreased by opening the knife, as it is observed in the absence of pressure waves downstream from the shock in the left image. The reason is that as the knife moves out only stronger deflections of the light will be covered, which means that only stronger density gradients will be captured by the system. So opening the knife increases the lower limit of the visible density gradients.

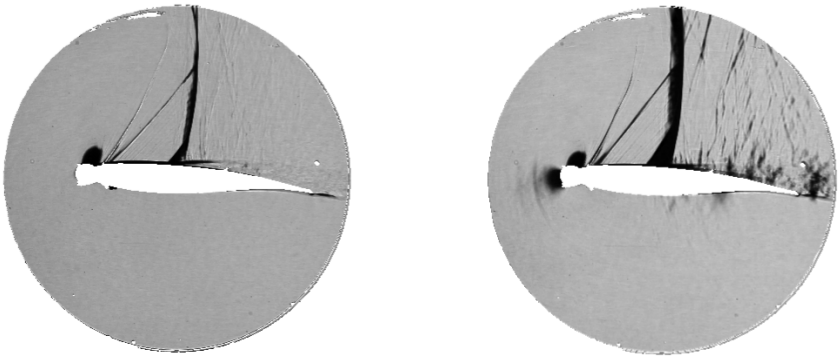

Figure 3.12: Schlieren sensitivity comparison between open (left) and deep (right) knife positions

Also the orientation of the knife is of great importance. Depending whether the knife is vertical or horizontal, the density gradients to be measured will be different. An horizontal density gradient deflects the light in the horizontal plane, so a vertical knife is needed to cut off those deflected beams and show the horizontal gradient. In general, the density gradient direction measured by the system is normal to the knife position.

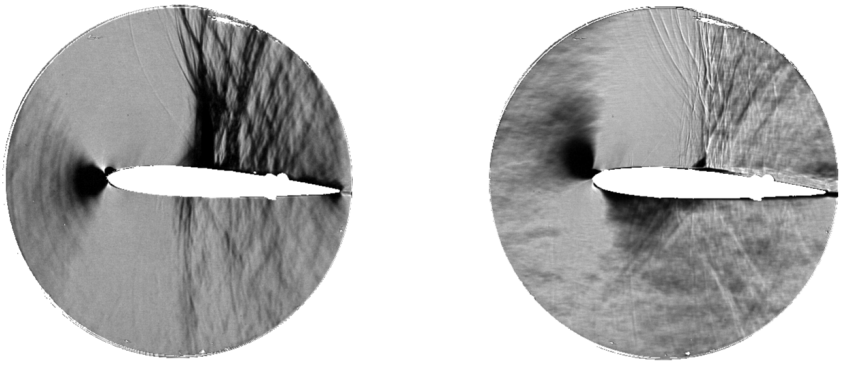

Figure 3.13: Schlieren setup comparison between vertical (left) and horizontal (right) knife orientation

As an example, in Fig. 3.13 both vertical and horizontal knife results are visualized. The shock wave that appears over the airfoil surface is a quasi-normal shock, so it presents an horizontal gradient of the density field. As shown in the figure a vertical knife (left image) captures better such gradient. However, the separation region is better visualize in the horizontal knife case, since it presents a vertical density gradient with respect to the outer flow.

Light diffusion at the pinhole

Using transparent adhesive tape in the pinhole in order to diffuse the light beam becomes important when trying to enhance the system. Some experiments were performed to compare the quality improvement achieved. The results can be observed in Fig. 3.14. Diffusion of the light beam using the tape enhances the sharpness of the image, while not using it results in blurry edges. It was finally decided to use the tape for the experimental campaigns given the improvement it produces.

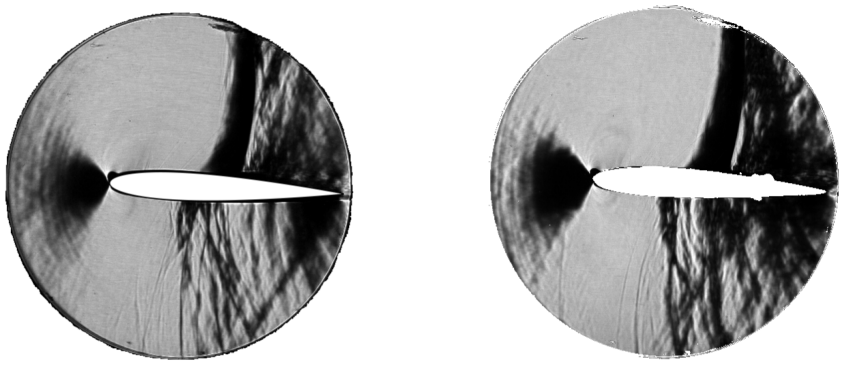

Figure 3.14: Schlieren setup comparison with tape (left) and without tape (right) in the pinhole

Exposure time

Another important parameter, maybe more related to the acquisition device rather than the Schlieren system itself, is the camera exposure time. This parameter affects the quality of the image as too long exposure times will lead to blurry results due to big particle displacements, and too short ones will importantly decrease the average light intensity of the images.

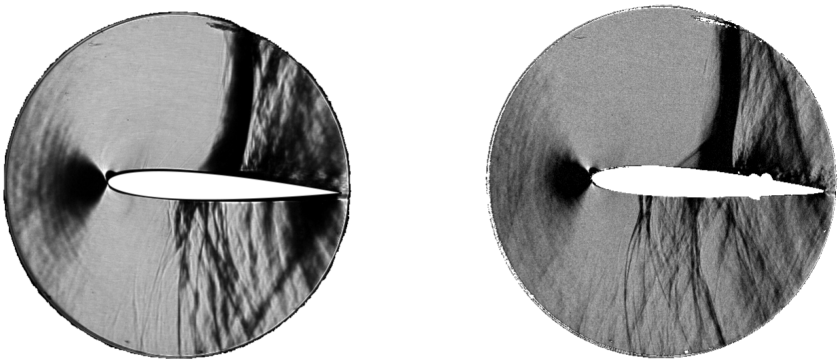

Figure 3.15: Schlieren setup comparison with $t_{exp} = 10\mu s$ (left) and $t_{exp} = 2\mu s$ (right)

As it can be observed in Fig. 3.15, exposure times of $2\mu s$ gives sharper results than $10\mu s$. In the former, the flow field looks almost instantaneous, while in the latter small displacement lines can be observed. Despite this, the case for $t_{exp} = 10\mu s$ was chosen for the experiments because such an improvement in the quality of the Schlieren results is not really needed for the present study.

3.6 Oil visualization

Oil flow visualization is an experimental technique widely used in the aerodynamic field that relies on the mechanical interaction between the fluid flow and a thin layer of oil applied to the model previous to the experiment. The oil is mixed with a fine powder pigment that stands out against the background. During the experiment the friction between air and the mixture carries away the oil leaving a pattern on the model surface. The pattern topology depends on the flow features that occur near the surface of the model and its interpretation is tightly related with how the pattern was formed. Once the experiment is over, the model is usually extracted from the wind tunnel in order to record and photograph the results and proceed to the analysis.

Many manuals, instructions and guidelines about the preparation and use of this technique are available, not only in the open literature but also as unpublished laboratory documents and procedures. The mixture needs specific physical properties as viscosity, density, vapor pressure or melting point, depending on the kind of experiments it will be used for. Also, note that an important requirement for the pigment is to highlight the pattern against the model background. For this reason, in this project titanium dioxide (TiO_2) has been chosen

as pigment.

This is an intrusive technique since the no-slip condition of the flow over the model surface is affected by the presence of the oil film. In the interaction between air and oil the velocity of both fluids is the same and different from zero. Notwithstanding the foregoing, a study from Squire (1969) showed that in general the velocity in the interface is very small and the effect of the presence of the oil film can be neglected. This, however, is not the case in regions of flow separation or reattachment or under the presence of a shock wave, conditions under which the uncertainty of the method increases and careful has to be taken when interpreting the results. The present experiments are characterized by the presence of such regions where the uncertainty may be high enough not to rely on quantitative results from the oil visualization. However, the purpose of this experiments is of a qualitative nature, just to study the state of the boundary layer under certain conditions, so no specific measures or considerations are taken into account.

The aim of this technique in the present experiments is to study the boundary layer development under the influence of different transition trips attached to the model. The presence of natural transition is analyzed in the clean airfoil for both models and the occurrence of forced transition is analyzed under the influence of different transition trips, namely Carborundum 150, 320, 400 and 500 and Zig-zag trip of 0.2 mm thickness.

3.7 Particle Image Velocimetry

Particle image velocimetry, also known as PIV, is nowadays one of the most advanced measurement techniques in experimental aerodynamics that allows to acquire velocity fields of specific regions of the flow. It is a non-intrusive technique and as so it allows for its application in regions and flow regimes that otherwise would be problematic, as high speed flows with shock waves, or regions near the boundary layer. An important characteristic of this technique is that it is a whole-field technique, i.e. it provides information of relatively large areas or volumes of the flow as opposed to other techniques that only give information at discrete locations. However, despite the relatively high spatial resolution of this system, the time resolution is bounded by current technological restrictions.

The working principle of this technique can be briefly explained as follows. The flow is seeded with reflective particles, capable of scattering light and truthfully follow the flow motion without introducing a large disturbance in it. The desired region of the flow (FOV) at which the recording system is targeting is then illuminated by means of a laser pulse. When the particles are inside this region, several consecutive images separated by a known Δt are taken in which the particles positions are captured due to the laser light they scatter in the cameras direction. The frames obtained from this recording are then equally discretized in the so called interrogation windows, and by means of a cross correlation analysis between pairs of consecutive images, the mean average displacement of the particles is estimated in every interrogation window. This displacement is taken from the correlation maps as the distance between the origin and the peak of largest correlation value. Knowing the

displacement and the time lapse between the images, this allows for the computation of the velocity of the particles in every interrogation window, i.e. the output of this analysis is one velocity vector per interrogation window that indicates an estimate of the velocity of the flow. This procedure is shown by steps in Fig. 3.16. Further information about the PIV technique, its working principles, physical and mathematical background, image evaluation and data post-processing can be found in the PIV practical guide from Raffel et al. (2013).

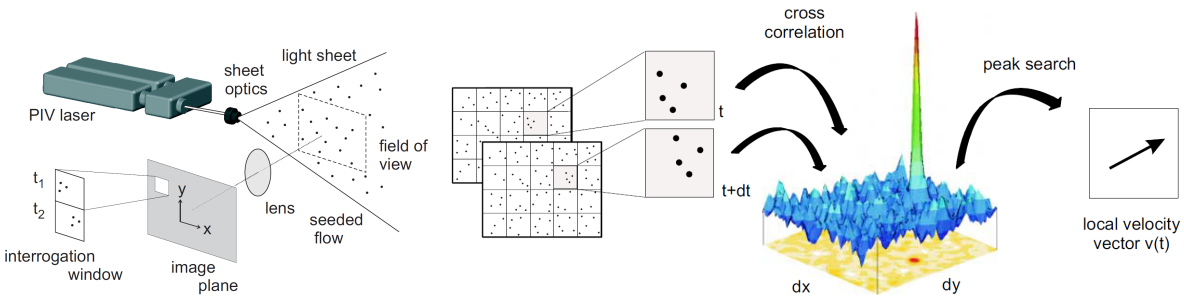

Figure 3.16: PIV working principle, LaVision (2015)

3.7.1 Motivation

In order to answer the main objectives of this project, information about the velocity field in the region after the shock wave is needed. It is not intended to obtain the instantaneous pressure field of the flow, so the aim of the PIV experiments is the 2-component velocity field. Firstly, a relatively large area needs to be studied that expands from the shock motion region to the trailing edge and up to a certain height from the airfoil chord. The reason for this is that in order to study the buffet phenomena and its feedback mechanisms, which are known to be related with the flow separation region, an overall view of the rear airfoil flow field is needed to be able to study the development of the shock motion and to link it with the behavior of the wake. One important requirement for the measurement process is that it needs to be non-intrusive. Since the region of interest after the shock is subsonic, the presence of any device downstream from the airfoil would act as a noise source, generating pressure waves that would travel upstream and interfere with the shock wave. Relatively high spatial resolution is needed in order to properly capture the phenomena close to the boundary layer as it develops at the shock foot and in the downstream region. Furthermore, high temporal resolution is desired in order to time resolve the shock motion and the development of the flow features that it causes. Note that it is not necessary, nor even possible, to temporally resolve the flow itself at speeds close to sonic conditions with the available hardware, however the requirement is to do it for the shock motion which has expected frequencies of $\sim 160Hz$. The planar PIV technique fulfills perfectly these requirements and provides the 2-component velocity fields necessary for a complete analysis of the flow field. Furthermore, the Aerodynamics high speed lab of TU Delft has the necessary tools, hardware, software and experience to apply this technique.

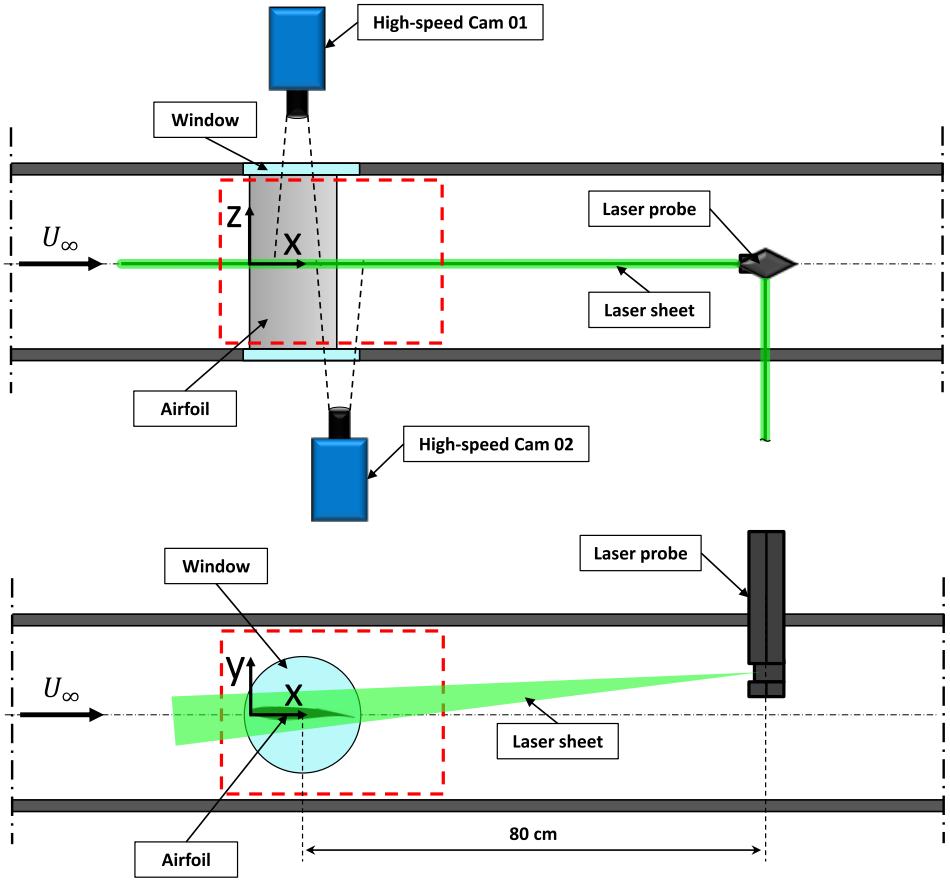

Figure 3.17: Plan view (top) and side view (bottom) of the PIV setup

3.7.2 PIV arrangement

Fig. 3.17 shows the planar PIV setup used in this project. This setup was the same in the two different experimental campaigns done over the NACA0012 and OAT15A airfoils. Note that the high speed laser does not appear in the sketches, it was mounted in a metal structure above the wind tunnel. The cameras were placed at 90° with respect to the flow direction and the laser probe was introduced in the tunnel in two different configurations. The first one with an insertion length of 17 cm for the NACA0012 experimental campaign, and the second one of 4 cm for the OAT15A experimental campaign, measured from the inside top wall of the wind tunnel.

3.7.3 Seeding system

The seeding system of the TST-27 wind tunnel consists of a hose that communicates the seeding generator with the seeding rake placed in the reservoir. This rake is one third the size of the settling chamber diameter and it consists of several outputs that eject the particles into the stream tube. The hose has a control valve that allows to modify the seeding density

in the flow from the control room. The seeding generator is a high-pressure cyclone separator operated at 10 bar. Note that the seeding is generated and released online, i.e during the run and not before.

The main requirement for the seeding particles is that they trace the flow accurately, characteristic that is normally measured by means of the particle relaxation time τ_p and the characteristic flow timescale τ_f. The relation between these two parameters is the Stokes number S_k. Specially challenging situations in high speed flows are encountered across shock waves or in thin shear layers, for instance downstream from strong separation points, where $S_k >> 1$. The flow field studied in this project is indeed characterized for the presence of these kind of regions where the seeding quality may lead to measurement errors, hence a high-quality seeding material is needed. Fine grade Titanium Dioxide (TiO_2) solid particles were used, suitable for high speed flows with a response time of $\sim 0.56\ \mu s$, see Ragni et al. (2011). The particles of a mean diameter of 50 nm are able to generate a seeded stream tube of approximately 10 cm diameter in the test section that trace the flow accurately and with relative small uncertainty if compared to other seeding materials available in the lab as the Di-Ethyl-Hexyl-Sebacat (DEHS). One of the main drawbacks for the use of TiO_2 is the hazard they pose to health due to their small size, e.g. they can penetrate organic tissue.

Figure 3.18: Seeding generator

3.7.4 Illumination system

Two different high speed lasers were used for the PIV campaigns. For the NACA0012 campaign the Mesa^{TM} PIV Nd:YAG dual-cavity laser was used operating in dual pulse mode at 8 and 20 kHz repetition rates. The laser emits a collimated monochromatic beam with a pulse duration of ∼150 ns and a wavelength of 532 nm, i.e. visible green light, at 18 mJ and 6 kHz. On the other hand, due to logistic reasons the laser had to be changed for the OAT15A PIV experimental campaign. Instead, the Quantronix Darwin Duo Nd:YLF laser was used operating in dual pulse mode at 8 kHz repetition frequency. The laser also emits a collimated monochromatic beam with a pulse duration of ∼210 ns and a wavelength of 527 mm at 22 mJ and 1 kHz. In both cases the lasers were mounted on top of a metallic structure in order to reduce the optical distance from laser to model. By doing so, the divergence of the light beam was reduced and its quality enhanced.

The laser beam was inserted inside the wind tunnel from the top by means of a hollow metallic probe that contains an optical system to reshape and resize it. Two different configurations for the laser probe were used in the experiments, the first one (50% configuration) with an insertion length of 17 cm, mostly used for the NACA0012 experimental campaign and the second one (10% configuration) with an insertion of 4 cm, for the OAT15A campaign. The reason for this reduction in length was that, after the NACA0012 experiments, it was discovered that there was an influence of the probe over the shock motion and the buffet phenomenon. Note that the names assigned to both configurations (10% and 50%) simply refer to an approximation of the tunnel height covered by the probe length.

Since the PIV experiments were two dimensional, a laser sheet was used with thickness of ∼1.5 mm that covered the desired flow region, located approximately in the spanwise mid position of the model. The light sheet was created by means of the optical system inside the metallic probe. The output is an expanding-height contracting-thickness sheet that needs to be adjusted to the model. Note that typically the thickness waist should be placed beyond the model to avoid optical sources of error.

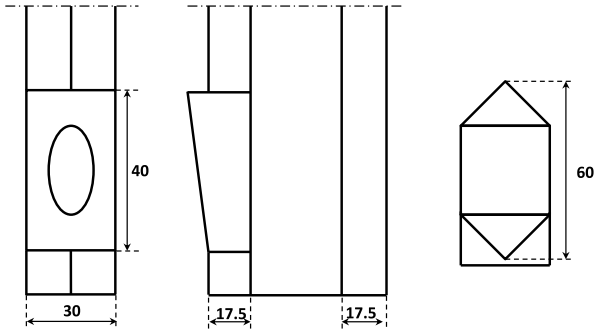

Figure 3.19: PIV laser probe: front (left), side (center) and top (right) views, [mm]

3.7.5 Imaging & timing setup

The recording system consisted of two high-speed cameras as shown in Fig. 3.17 and a high-speed controller unit to synchronize them with the laser. The cameras were Photron FastCAM SA1 (12-bit dynamic range) CMOS with a maximum resolution of 1024x1024 pixels and a pixel size of 20 μm. The total memory is 8 GB and the frame rate at full resolution is 5400 fps, however for the experiments a higher acquisition frequency was needed, hence the resolution was decreased. Two Nikon lenses of 105 mm focal length were used with $f_{\#} = 8$.

Three PIV configurations were used in the experiments, each of them consisting of two different fields of view (FOV). The frame rate was taken as the dominant parameter, so the final size and resolution of the FOVs was conditioned by the cameras performance. The first two configurations (Config. I and II) at $f_{acq} = 8$ kHz, with two FOVs of physical size of 40x24 mm (W x H) and a resolution of 768x480 pixels each. This leads to a magnification factor of 0.384 and a digital resolution of 19.2 pix/mm. These are the main configurations for the experiments, configuration I over the NACA0012 and configuration II over the OAT15A.

The third configuration (Config. III) was recorded at $f_{acq} = 20$ kHz, with FOVs of actual size of 24x15 mm (W x H) and a resolution of 448x288 pixels each. The magnification factor of this configuration is 0.390 and the digital resolution is 18.7 pix/mm. Config. III was used on the NACA0012 model. These parameters are gathered in Table 3.6 and a graphical representation of the different configurations and fields of view is given in Fig. 3.20.

The mathematical relations and the procedure to compute the parameters shown in Table 3.6 are presented next, exemplified for Config. I. In the first place, the frame rate is taken as the dominant parameter, 8 kHz in this case. This leads to the maximum resolution at which the cameras are able to record at such frequencies, 768x480 pixels. Once the resolution is known, the FOV physical size can be decided taking into account the resulting digital resolution, 19.2 pix/mm. Note that small values of digital resolution will lead to large uncertainties in the results, whereas too high densities would mean a reduction of the physical size of the FOV. The magnification factor can be computed as

$$M = \frac{\text{pixel size} \times \text{FOV resolution}}{\text{FOV length}} = \frac{20 \cdot 10^{-6} \times 768}{40 \cdot 10^{-3}} = 0.384. \tag{3.11}$$

And considering a particle diameter (d_p) of 2 pixels to avoid peak locking, the $f_\#$ parameter follows,

$$f_\# = \frac{d_p}{2.44 \cdot \lambda \cdot (1 + M)} = \frac{2 \cdot 20 \cdot 10^{-6}}{2.44 \cdot 532 \cdot 10^{-9}(1 + 0.384)} \approx 22. \tag{3.12}$$

Note that this $f_\#$ value is too high for the lenses. In the experiments $f_\# = 8$ is used, which leads to a particle diameter of $d_p \sim 0.7$ pixels. However this may cause peak locking since the size of the particle falls inside one pixel, loosing subpixel accuracy. The solution for this is to move the plane of focus beyond the FOV plane, so the effective particle diameter increases to about 2 pixels.

Property	**Units**	**PIV config. I**	**PIV config. II**	**PIV config. III**
Airfoil	-	NACA0012	OAT15A	NACA0012
f_{acq}	kHz	8	8	20
Δt	μs	2.5	2.5	2.5
FOV length	mm	40x24	40x24	24x15
Resolution	pixel	768x480	768x480	448x288
Magnification factor	-	0.384	0.384	0.390
$f_\#$	-	8	8	8
Image pairs	-	7761	7761	20000
Measuring time	s	0.97	0.97	1
FOV A	-	$0.4 \leq x/c \leq 0.8$	$0.3 \leq x/c \leq 0.7$	$0.4 \leq x/c \leq 0.64$
FOV B	-	$0.8 \leq x/c \leq 1.2$	$0.7 \leq x/c \leq 1.1$	$0.64 \leq x/c \leq 0.86$
FOV overlap	mm	4	4	2
Digital resolution	pix/mm	19.2	19.2	18.7

Table 3.6: Parameters of PIV configurations

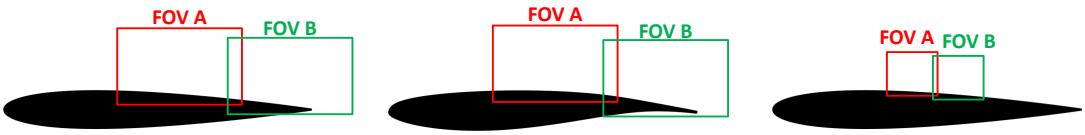

Figure 3.20: PIV Config.I (left), Config.II (center) and Config.III (right)

The timing sequence of the system, i.e. laser synchronized with cameras, is presented in Fig. 3.21. A pulse separation of $\Delta t = 2.5\ \mu s$ was used between frames, which leads to an average particle displacement of $\Delta x \approx 13$ pixels and to a minimum window size of 24x24 pixels. The laser pulse duration is $\Delta t_p = 200$ ns, ensuring a particle displacement of less than a pixel, resulting in sharp images.

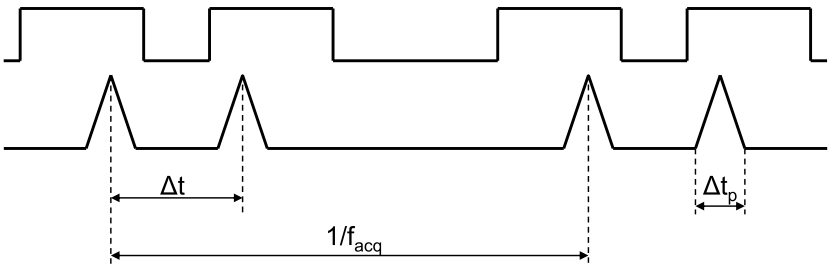

Figure 3.21: Timing sequence of cameras (top) and laser (bottom)

3.7.6 DaVis data processing

Here, the steps followed for the preprocessing of the experimental data from the planar PIV are explained along with the parameters used for the computation of the velocity vector fields. This data processing is done using the software DaVis.

Firstly, the data preprocessing is necessary to *clean* the images taken by the PIV system. This means the reduction of the noise and reflections captured by the cameras and the increase of the contrast of the seeding particles against the background. This enhances the quality of the results since the velocity computations are based on the contrast of the seeding particles. Several steps are taken for this preprocessing procedure and are explained next.

1. Obtain the minimum and subtract it from all the images. The minimum is obtained at every pixel of the field of view, and it is the minimum amount of light obtained time wise in each pixel. The result is a single image.

2. Compute the average of the field of view. It is obtained by averaging time wise the light intensity information in each pixel, the result is a single image.

3. Normalize the images. This is done by multiplying every image by a constant factor and then dividing it by the average field. The aim of this step is to normalize the level

of light intensity throughout the total field of view. It is important since the average light intensity before and after the shock may be different.

4. Mask out the regions that correspond to the airfoil surface or where the reflections are too high.

Fig. 3.22 shows the original and processed images for comparison.

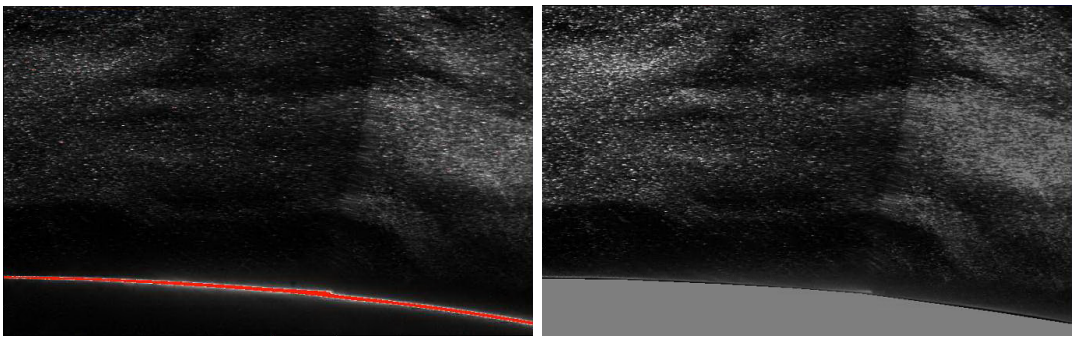

Figure 3.22: Raw images of FOV A before (left) and after (right) the preprocessing procedure

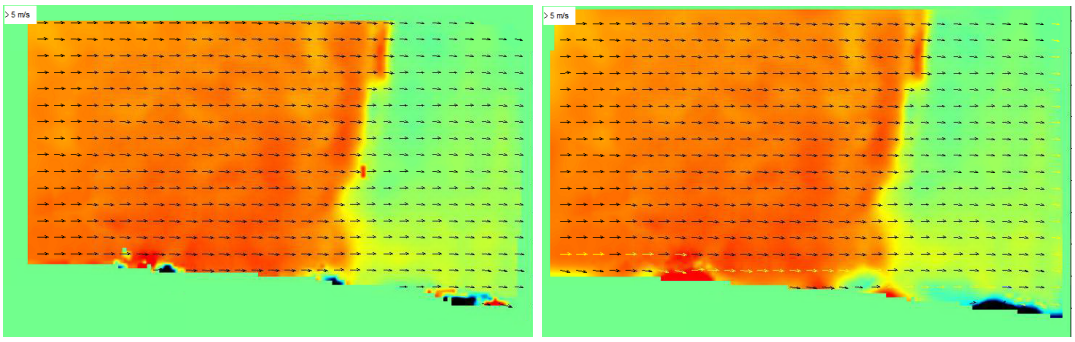

Figure 3.23: Vector field of FOV A before (left) and after (right) the outlier detection postprocessing

Secondly, once the original images are preprocessed the calculation of the velocity vector fields takes place. This computation is done with DaVis, using a cross-correlation analysis between the two frames of every instantaneous image. These frames are spatially discretized in the so called interrogation windows and the correlation is done for each of these windows. The output is a displacement vector that together with the time difference between the frames ($\Delta t = 2.5\mu s$) defines the estimated velocity of the flow at that window. The computation is done with a multi-pass approach of decreasing size. It starts with a windows size of 96x96 pixels for the first pass, with a total overlap of 75% and with a window squared shape. This is an iterative process that refines the results increasing its accuracy. The last passes are done for windows sizes of 24x24 and 16x16 depending on the case, 75% overlap and an automatized window shape, which optimizes the shape as a function of the expected particle displacement. The multi-pass post-processing uses the function *universal outlier detection* of

DaVis, which detects the vectors out of the standard deviation of a predefined filter region of 5x5 pixels. The vector computations requires a previous calibration of the system. Two different calibrations were used with a maximum RMS of 0.18 pixels for both airfoils.

Finally, after the vector calculation is complete, a postprocessing procedure of the vector fields is done in order to remove possible outliers. For that, the *universal outlier detection* of DaVis is used again with the same parameters as during the vector calculation, only this time groups of vectors with less than 5 elements are removed and replaced by averaged vectors considering the neighbor elements. Fig. 3.23 shows the result of the vector field computation of the right image in Fig. 3.22 with and without the the outlier detection postprocessing.

3.8 PIV Uncertainty analysis

For a proper evaluation of the measurements obtained in experimental studies, an uncertainty analysis of the results is needed in order to account for the errors that make such results deviate from the actual real values. There are several sources of uncertainty that affect the present PIV measurements and that will be explained and defined in this section. There are, of course, other sources that are not taken into account as they are considered to have a negligible effect over the results, as for instance temperature variations along the tunnel and during its operation.

3.8.1 Uncertainty in average fields due to ensemble size

This uncertainty is of statistical nature. The mean flow and more specifically the phase average flow are studied in detail in this project. To create these fields a finite number of images is used, this leads to an uncertainty error that is defined, following the work by Benedict and Gould (1996), as

$$\epsilon_{\bar{u}} = \frac{\sqrt{\overline{u'^2}}}{\sqrt{N}} = \frac{\langle u' \rangle}{\sqrt{N}}, \qquad \epsilon_{\bar{v}} = \frac{\sqrt{\overline{v'^2}}}{\sqrt{N}} = \frac{\langle v' \rangle}{\sqrt{N}}, \tag{3.13}$$

for both the horizontal and vertical velocity components. N is the ensemble size, i.e. the amount of data used for the average procedure and $\sqrt{\overline{u'^2}}$ is the root mean square (RMS) of the velocity fluctuations. This statistical uncertainty is computed for every phase-average velocity field.

3.8.2 Uncertainty from PIV cross-correlation

This uncertainty is associated to the PIV system. The error from the cross-correlation procedures of the digital images obtained from the PIV measurements was estimated by Humble

et al. (2009), who conservatively gave the values

$$\epsilon_{corr} = \begin{cases} 0.1 \quad pixel & \text{for planar PIV} \\ 0.2 \quad pixel & \text{for tomographic PIV} \end{cases}$$

And the associated uncertainty is computed as,

$$\epsilon_{cc} = \frac{\epsilon_{corr}}{\kappa \Delta t}, \tag{3.14}$$

where Δt refers to the time delay between pulses and κ to the digital resolution of the images, given in *pix/mm*.

3.8.3 Uncertainty from PIV seeding particles slip

The seeding particles used for the PIV measurements are supposed truthfully the flow along their movement, however there is always a small deviation or lag due to the inertia of such particles. In order to account for this deviation, the uncertainty of the particles slip is computed. The particles slip velocity can be derived as

$$\vec{u}_{slip} \approx \tau_p \cdot \vec{a}_p, \tag{3.15}$$

where τ_p is the particle response time and a_p the particle acceleration. The particles used in the experiment was TiO_2-50, with a response time of $\tau_p \sim 0.56 \mu s$ as measured by Ragni et al. (2011). From Melling (1997) and Sun (2014) it is known that the equation for the particles acceleration can be simplified if the particle density is larger than that of air as

$$\frac{d\vec{u}_p}{dt} = \frac{\vec{u}_p - \vec{u}_f}{\tau_p}, \tag{3.16}$$

being u_p and u_f the instantaneous velocities from particles and flow respectively. If steady flow is further assumed, Eq. 3.16 reduces to $\vec{a}_p = \vec{U} \cdot \nabla \vec{U}$ as demonstrated by Ragni (2012). Introducing this into Eq. 3.15 it follows,

$$\epsilon_{slip} = \vec{u}_{slip} \approx \tau_p \cdot (\vec{U} \cdot \nabla \vec{U}) = \tau_p \cdot \vec{U} \cdot \left(\frac{\partial u}{\partial x} + \frac{\partial v}{\partial y} \right) \tag{3.17}$$

This approximation is valid for regions of the flow where there are not strong vortices. It is expected that the highest value of this uncertainty occurs in the region where the strongest velocity gradients are located, i.e. the shock wave region. This assumption can be used as there are no vortices at the shock wave. The acceleration estimated for the flow at the shock region is of the order of $-30 \cdot 10^6$ m/s, computed assuming a shock thickness of the order of 1 mm (given by the smallest scale of the spatial resolution) and a maximum velocity gradient of ~ 100 m/s at the shock. This leads to a maximum slip velocity of $\vec{u}_{slip} \approx \tau_p \cdot \vec{a}_p \approx 16.8$ m/s in the shock wave region.

3.8.4 Uncertainty from PIV spatial resolution

The uncertainty from the spatial resolution is determined by a normalize window size, defined as the ratio between the actual window size (WS) and the wave length of interest (λ), i.e. WS/λ. This leads to a dependence of the uncertainty with the actual final interrogation windows. In the present experiments, the highest WS was of 24x24 pixels. The ratio of the measured velocity and the real velocity (u/u_0) can be estimated with the *sinc* function, see Schrijer and Scarano (2008), as follows,

$$\epsilon_{sr} = \frac{u}{u_0} = sinc\left(\frac{WS}{\lambda}\right). \tag{3.18}$$

The wavelength of the largest vortices shed in the separated region is used to compute this uncertainty.

3.8.5 Uncertainty values

The values obtained from the uncertainty analysis are gathered in Tables 3.7 and 3.8. Note that the highest statistical uncertainties are found during the upstream travel of the shock wave (phases 1 to 5) at the shock foot region, due to the strong separation, the presence of the shock and the airfoil surface.

	Phase							
Parameter	1	2	3	4	5	6	7	8
$\epsilon_{\bar{u}}$ [m/s]	≤ 10	≤ 7.5	≤ 11.1	≤ 10.5	≤ 13.9	≤ 6.5	≤ 4.3	≤ 3.8
$\epsilon_{\bar{v}}$ [m/s]	≤ 4	≤ 3	≤ 3	≤ 3	≤ 3.8	≤ 2.5	≤ 2	≤ 1.7

Table 3.7: Statistical uncertainty values

Uncertainty source	Parameter	Value
Cross-correlation	ϵ_{cc}	≤ 2.1 [m/s]
Particle slip	ϵ_{τ_p}	≤ 16.8 [m/s]
Spatial resolution	ϵ_{sr}	$\leq 1\%$

Table 3.8: PIV related uncertainty values

Chapter 4

Post-processing methodology

The present chapter gives a mathematical description and explanation of all the steps followed during the post-processing procedure of the results from both the Schlieren visualization and the particle image velocimetry. The aim is to show what was the approach followed and all the steps involved in the data analysis so that the reader has a clear idea of what are the expected results. Fig. 4.1 shows the scheme of the analysis done for the PIV data, which basically can be divided into two different branches. The first branch (blue boxes) is used for the results from both the Schlieren and the PIV data, it is the spectral analysis of the shock location in time. The second branch (green boxes) is used only for the PIV data and it consists of the velocity field decomposition in its different components ($\vec{u}(x,t) = \bar{u}(x) + \tilde{u}(x,t) + u'(x,t)$) and the correlation of the velocity fields with the purpose of capturing different periodic flow phenomena. All the post-processing explained in this chapter as well as the graphics and velocity fields are done using Matlab.

The results obtained from the Schlieren measurements can be directly introduced into the post-processing procedure without any processing, i.e. the raw images obtained from the experiments are directly analyzed. On the other hand, the PIV results first need to be processed. This processing consists of the image correlation using DAVIS which is explained in Chapter 3, and the merging of the velocity fields. The merging procedure,see Fig. 4.2, combines both fields of view in order to have an instantaneous overview of the overall measured flow field. This process is automatically ran over the almost 8000 instantaneous images per case, where an overlap in y and x directions is computed and optimized for every case. Once the velocity fields are properly merged, the results are ready to be used in the post-processing procedure.

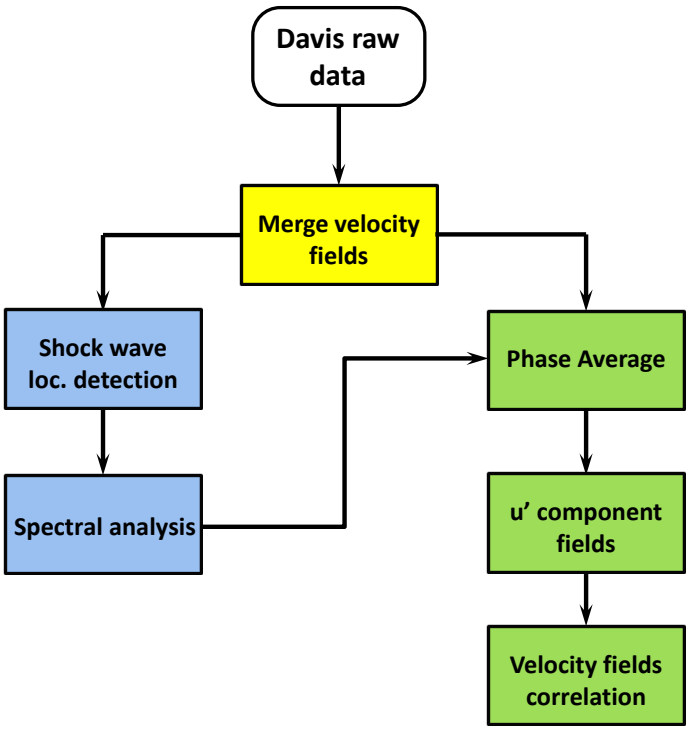

Figure 4.1: Post-processing scheme of the PIV results

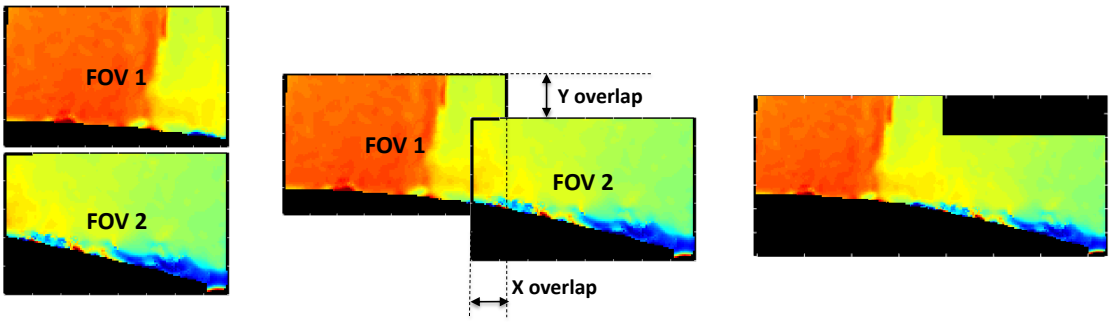

Figure 4.2: Merging of PIV velocity fields procedure

4.1 Spectral analysis

The spectral analysis is done for the results obtained from both the Schlieren and the PIV measurements. In both cases, the analysis consists of two main steps,namely

1. Detection of shock wave chordwise location as function of time
2. Spectral analysis of the shock location signal.

The shock wave detection procedure differs between the Schlieren and PIV cases, whereas once the shock location signals are obtained, the spectral analysis is exactly the same for both cases. The reason why the shock detection is different is due to to the nature of the results obtained from both techniques. The Schlieren results are matrices that gather the light intensity in every pixel of the image, whereas the PIV gather the numerical value of the velocity in every correlation window.

4.1.1 Shock wave detection

The shock wave detection procedure consists of the following steps,

1. Several lines parallel to the chord (Schlieren case) or streamlines (PIV case) are depicted on the suction side of the airfoil, at a certain distance from the surface. These lines are parametrized so that the number of lines, distance and location can be controlled. The reason why straight lines are used in Schlieren is because the streamlines cannot be computed.
2. The values of light intensity (Schlieren case) and horizontal velocity (PIV case) are acquired at the location of such lines and their spatial gradients are computed as

$$\nabla \vec{u} = \frac{\partial u}{\partial x}\vec{i} \approx \frac{u_{i+1} - u_i}{x_{i+1} - x_i}\vec{i},$$

   where u stands for the light intensity or the horizontal velocity, in the horizontal direction.
3. The shock wave produces a decrease in both light intensity and velocity that can be easily detected. The shock location is detected by locating the maximum value of the gradients along the lines. Furthermore, in the PIV case a prediction algorithm is used that bounds the searching region based on previous results for the sake of computational costs optimization. The result is presented in Fig. 4.3.

Once the shock locations are detected and stored timewise, a statistical analysis is performed over the position-time signals to obtain the mean shock positions and its standard deviation and to correct possible errors using the 3-sigma rule, see Fig. 4.4. This rule establishes an

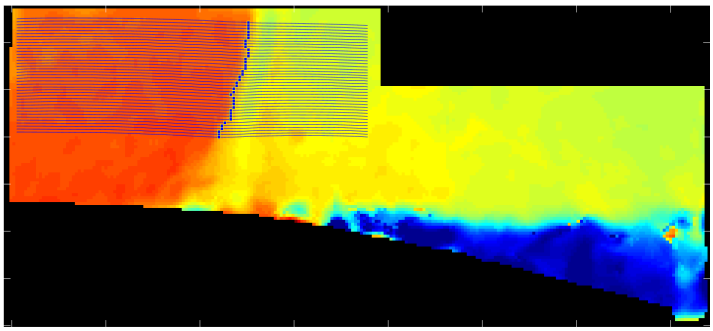

Figure 4.3: PIV shock detection result

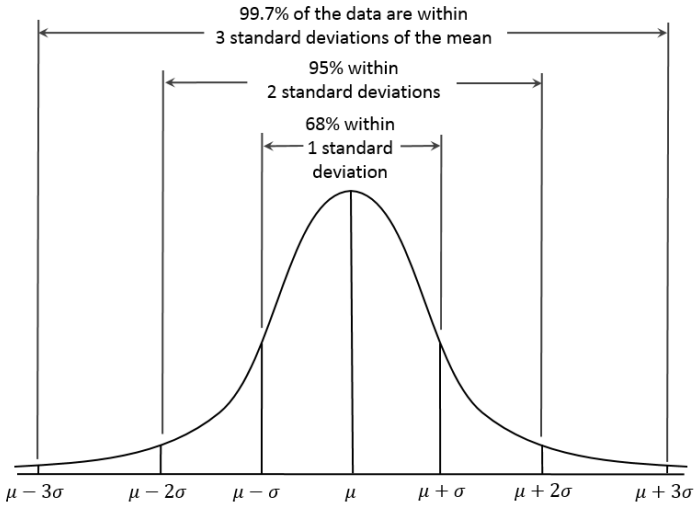

Figure 4.4: 68-95-99.7 rule of a normal distribution, μ stands for the average value and σ for the standard deviation

interval around the mean value of a normal distribution with a width of 3 standard deviations in which the data is considered to be correct. All the measurements that fall out of this interval are considered invalid and approximated as the mean average between the adjacent values. In mathematical notation this rule is

$$Pr(\bar{x} - 3\sigma \leq x \leq \bar{x} + 3\sigma) \approx 99.7\%,$$

where σ is the standard deviation of the signal and $\bar{x}$ its mean value. This means that the 99.7% of the data is inside the 3σ interval. Finally, after the all the values are enclosed under the 3σ interval, a single shock location is needed per time instant, the median of the values presented in Fig. 4.3 is taken as the final shock position. The result of the shock detection procedure is a single function position-time as the one presented in Fig. 4.5, that will be the input for the spectral analysis.

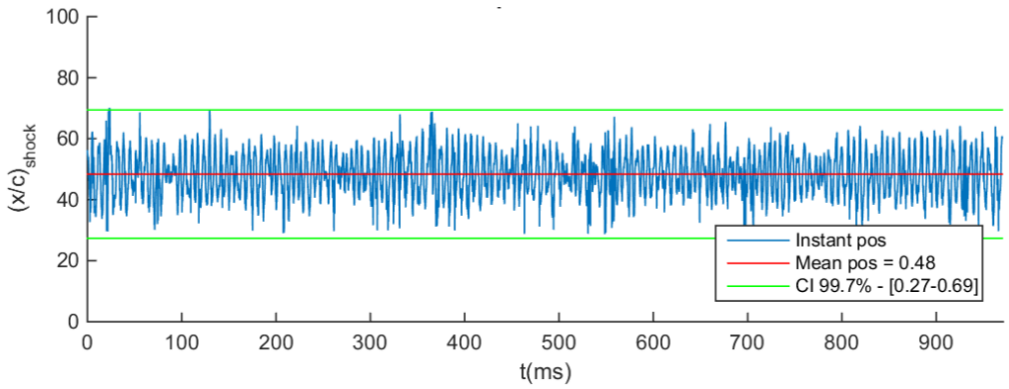

Figure 4.5: Shock location vs time signal for both the Schlieren and PIV cases

4.1.2 Spectral analysis

The aim of spectral analysis, also known as spectral density estimation of frequency domain analysis, is the decomposition of a certain complex signal into a series of simpler weighted sinusoids that allows to determine the frequency content of that particular signal, i.e. whether the signal is concentrated in specific ranges of frequencies or, on the contrary, it is spread. Ultimately, this allows to detect any periodicities in the signal, represented as peaks in the frequency spectrum at the frequencies that correspond to such periodic phenomena. The reason why this analysis is applied over the results from this experimental project is to analyze if there is any periodic effect involved in the shock motion and to obtain the dynamic properties of those effects, i.e. its frequency. This results will be compared with the estimated buffet frequencies from the literature to corroborate whether buffet is taking place over the selected airfoils. Spectral analysis can be divided in two main branches as stated by Solomon Jr (1991), namely,

- The Fourier transform, mostly used when there is no noise or random effects contained in the signal.
- Power spectral density (PSD) when the noise or random effects mask or cover the real phenomenon. In this case a smoothing procedure is needed. Note that PSD uses the Fourier transform.

The current case of study corresponds to the case of having noise and random effects from the shock position fluctuations that can mask the real behavior. This is why the PSD approach is used in order to get rid of that noise. The Fourier transform $X(f)$ of a time dependent signal $x(t)$ is mathematically defined as

$$X(f) = \int_{-\infty}^{\infty} x(t) e^{-i2\pi f t} dt.$$

However, in practice the Discrete Fourier Transform (DFT) is used instead, as the signals being analyzed are discrete as well. The DFT is mathematically represented as

$$X_k = \sum_{n=0}^{N-1} x_n \cdot e^{-i2\pi kn/N} dt,$$

where N is the amount of samples. The DFT is computed in Matlab by a fast Fourier transform algorithm (FFT). The Fourier transform produces a signal in the frequency domain that contains the amplitude and phase of each frequency component. Now, if instead of the amplitude, the squared amplitude (or power) is considered then the resulting function is referred to as power spectrum or Power Spectral Density (PSD). The PSD (P(f)) defines how the power of a signal is distributed in the frequency. Note that *power* can be actual physical power, but usually it just refers to the square of the units of the original signal and it is called *power* for convenience. The PSD is mathematically derived from Parseval's theorem as

$$\begin{cases} \int_{-\infty}^{\infty} x(t)^2 dt = \int_{-\infty}^{\infty} |X(f)|^2 df \\ \frac{1}{T}\int_0^T x(t)^2 dt = \int_{-\infty}^{\infty} P(f) df \end{cases} \quad \Rightarrow \quad P(f) = \frac{|X(f)|^2}{T} \quad [m^2/Hz],$$

where T refers to the period. In the current study, the spectral analysis is done using Welch's method, a PSD-based approach characterized for its noise reduction (signal variance reduction) and that it is used to estimate the power of the signal as function of its frequency. Welch's method divides the original signal into overlapping time segments with a certain overlap (from 0% to 50%). Then these segments are windowed in the time domain and the PSD is computed in each segment by applying a discrete Fourier transform and then computing the square of the result. The individual PSDs are then averaged, reducing the variance of the result. This averaging and the windowing of the segments is what makes of this method a *modified periodogram* or *averaged periodogram*. For further information about the mathematical description and main characteristics of this method, the reader is referred to Solomon Jr (1991).

Welch's method is applied over the shock position versus time signal using an inner Matlab function *pwelch* in which the amount of segments to discretize the signal and the overlap between them are parameters to be introduced. These parameters are chosen as default, i.e. 8 segments and an overlap of 50%. All the analysis of the experimental campaigns are done consistently maintaining these parameters fixed to allow for a proper comparison of the results. The result from the Welch's analysis over the time signal shown in Fig. 4.5 is presented in Fig. 4.6. Note that the vertical axis is multiplied with the frequency so that its units are those of the original signal squared, i.e. proportional to the energy of the signal at every frequency. This is usually known as the premultiplied power spectrum.

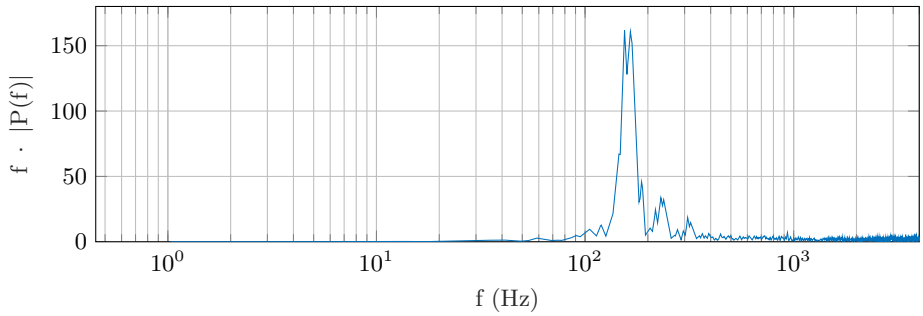

Figure 4.6: Result of Welch's method applied to the signal in Fig. 4.5

4.2 Correlation analysis

The correlation analysis is done exclusively over the velocity fields obtained from the PIV measurements. The aim of this analysis is to capture the existence and the dynamic characteristics of periodic features taking place in the velocity fields, specifically the upstream traveling waves and the shedding vortices. The necessary inputs for this analysis are the merged velocity fields and the results from the shock position procedure and its statistical analysis. The correlation analysis is divided into 3 main steps, namely

1. Computation of the phase average fields,
2. Computation of the turbulent velocity component fields,
3. Velocity fields correlation.

The correlation analysis is done over the fluctuating or turbulent velocity component u' to increase the sensitivity of the analysis. The reason is that the phenomena desired to be captured create weak disturbances that are precisely contained in this component. The average of the velocity fields, or more specifically, the phase average needs to be previously removed in order to obtain these velocity component fields. Again, all these steps are implemented in Matlab and coded so that they can be applied to all the different test cases independently.

4.2.1 Phase averaged velocity fields computation

For a periodic phenomenon, the information of the velocity contained in the instantaneous fields can be organized using the classical triple decomposition first introduced by Hussain and Reynolds (1972) and schematically plotted in Fig. 4.7,

$$\vec{u}(x,t) = \bar{u}(x) + \tilde{u}(x,t) + u'(x,t). \tag{4.1}$$

Where $\vec{u}(x,t)$ is the instantaneous velocity, $\bar{u}(x)$ is the time average or mean velocity component, $\tilde{u}(x,t)$ is the oscillatory or cyclic component and $u'(x,t)$ refers to the turbulent

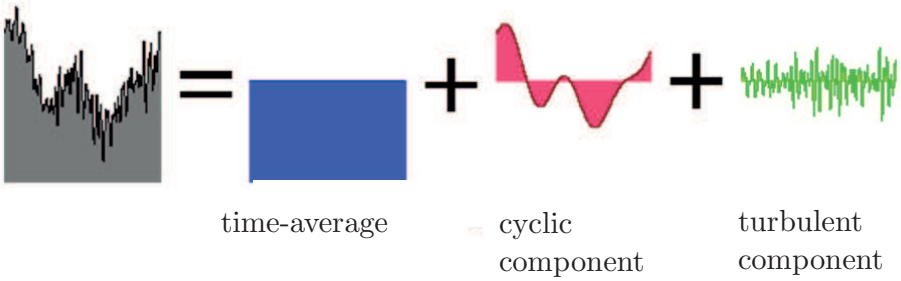

Figure 4.7: Unsteady flow velocity triple decomposition

or random component. This decomposition leads to different options to analyze the flow field and its development in time. Firstly, the average velocity field or mean flow, is represented by the term $\bar{u}(x)$. However, it is not useful if the aim is to study the unsteady development. For that, the phase average is used. It divides the flow development in phases that contain the time instants that belong to specific parts of the cyclic movement. This phase average contains the terms $\bar{u}(x) + \tilde{u}(x,t)$, which are the average term and the oscillatory component of the flow. This average shows the cyclic non-random velocity information. The higher the discretization is (amount of bins), the higher the accuracy, but there is a maximum that depends on the data acquisition frequency. Finally, the turbulent component $u'(x,t)$ can be computed as well just by subtracting the phase average fields to the instantaneous fields.

In order to compute the phase average fields, each buffet cycle has to be isolated and discretized in N phases. In the current analysis $N = 8$ has been chosen as the amount of phases due to acquisition rate limits, i.e. there are some cycles in which the amount of images is not superior to 8. Phase number 1 represents the most downstream shock position, phases 2, 3 and 4 the upstream travel of the shock wave, phase 5 the most upstream shock position and phases 6, 7 and 8 the downstream travel of the shock. As depicted in Fig. 4.8, the numeric labels for the phases actually correspond to a phase delay that is expressed, from 1 to 8, as 0, $\pi/8$, $\pi/4$, $3\pi/8$, $\pi/2$, $5\pi/8$, $3\pi/4$ and $7\pi/8$, however in the present document the numeric label is used for simplicity.

The information of the shock position in time obtained previously is needed to obtain the phase average. The first step is to isolate all the buffet cycles captured during the measuring time. In order to do so, an algorithm is created that looks for the local maximum and minimum points in the shock position signal by analyzing the gradients sign. A change of sign in the gradient indicates the presence of a local extreme. Once these peaks are found, they are labeled depending whether they are maximums (most downstream position of the shock) or minima (most upstream position of the shock). Now, taking all the data points between these peaks, they can be distributed in different subsets of data points that will define each of the phases. Fig. 4.9 shows the result of the isolation of the buffet cycles, where each of the detected peaks are signaled with a circular mark, most upstream positions marked in purple and most downstream positions in red. Furthermore, Fig. 4.10 displays the same information, but only during 20 ms, where the clear periodicity of the shock motion is observed. Finally, once all the available data are distributed over the 8 phases, they are averaged. The result from this averaging can be seen in Figs. 5.9 and 5.10. It

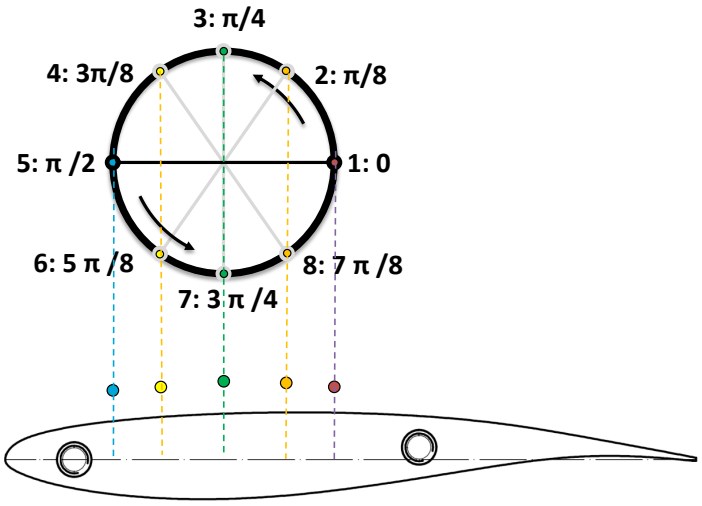

Figure 4.8: Discretization of a buffet cycle in 8 phases

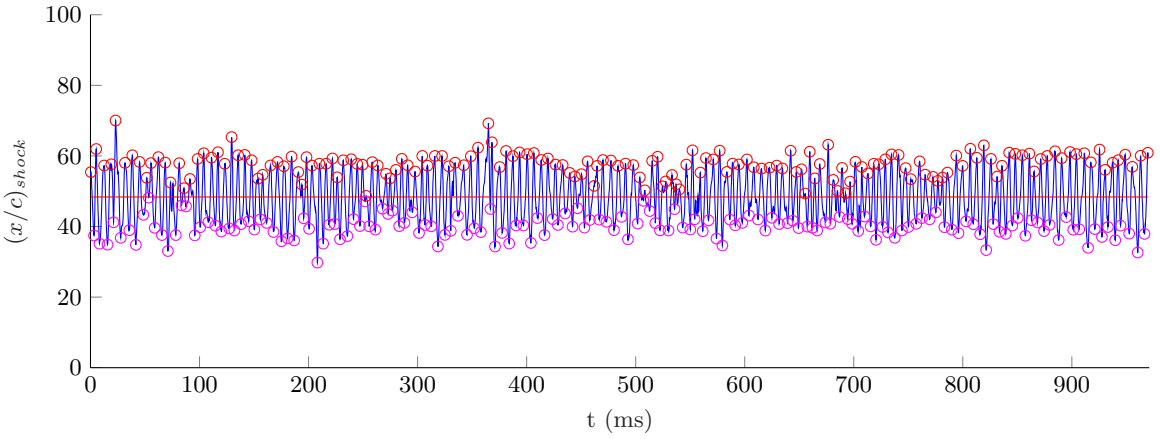

Figure 4.9: Buffet cycles isolation in the shock position signal

was estimated that all the phases contain about N/7 elements, except for phases 1 (most downstream position) and 5 (most upstream position) that contain N/16 elements, being N the total amount of samples. The reason is the way the coding has been implemented. Being $N \approx 8000$ this leads to ~ 1140 measurements per phase, except the most extreme positions that contain ~ 500 elements (quantities are approximate).

4.2.2 Computation of the *u'* velocity fields

As mentioned before, the u' velocity component is chosen as the velocity field over which the correlation analyses will be computed. The reason is that it only shows the velocity fluctuations with the large scale cyclic behavior removed, hence greatly enhancing the contrast

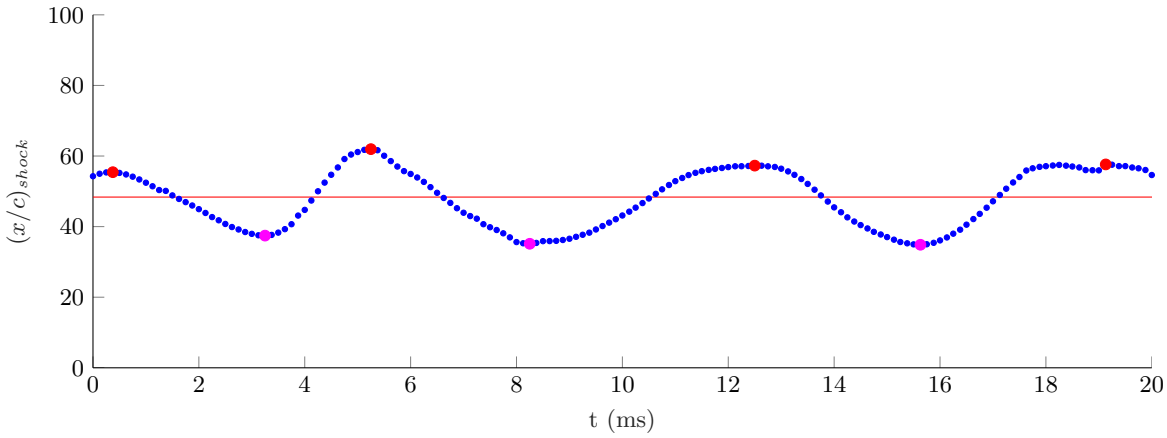

Figure 4.10: Buffet cycles isolation in the shock position signal

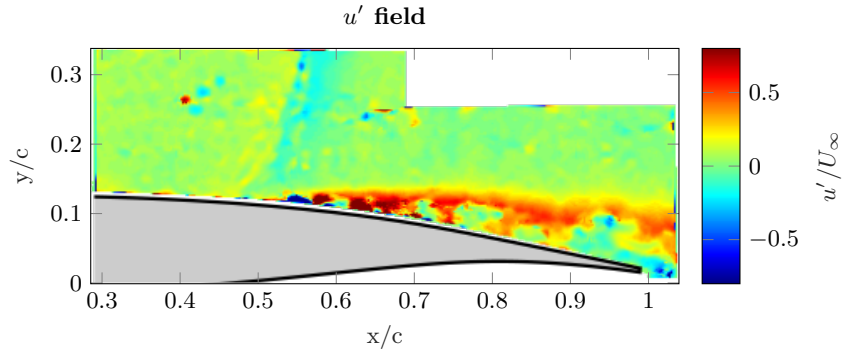

Figure 4.11: u' velocity field example

of small fluctuations and thus the sensitivity of a posterior correlation analysis of the flow phenomena. The computation of these velocity fields is straightforward once the phase average fields have been obtained, mathematically it can be expressed as,

$$u'(x,t) = \vec{u}(x,t) - [\bar{u}(x) + \tilde{u}(x,t)], \tag{4.2}$$

which basically states that the u' fields are computed by subtracting the corresponding phase average fields to the original or complete velocity fields. A sample result from this procedure can be observed in Fig. 4.11.

4.2.3 Correlation of the velocity fields

Three different correlation analyses are performed, each of them with a particular aim.

1. Firstly, with the objective of capturing the upstream traveling waves in the outer flow and their dynamic properties (velocity and frequency), a correlation analysis is done over a particular streamline.

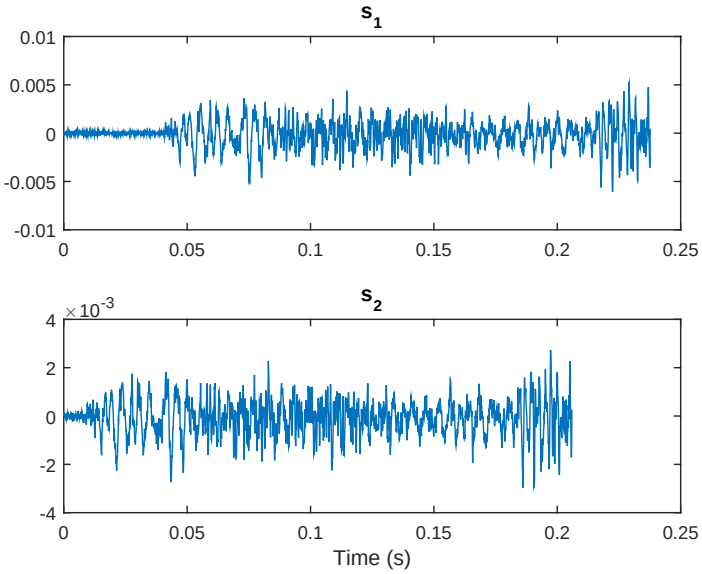

Figure 4.12: Two similar signals s_1 and s_2 delayed in time

2. Secondly, with the aim of capturing the convection velocity of the vortices shed at the wake, a cross-correlation analysis is done between pairs of images in the separated region of the flow.

3. Finally, with the aim of capturing the frequency of such vortices, an auto-correlation analysis is done over the same separated region as before.

In general terms, the correlation analysis is governed by the following standard correlation function,

$$R(\tau) = \int_{-\infty}^{\infty} \frac{s_1(t) \cdot s_2(t+\tau)}{\sqrt{s_1(t)^2 \cdot s_2(t+\tau)^2}} dt, \tag{4.3}$$

where $R(\tau)$ is the function that contains the correlation parameters, and $s_1(t)$ and $s_2(t)$ the functions to be correlated between each other. Given, for instance, two similar signals s_1 and s_2 like the ones presented in Fig. 4.12 that are delayed in time, the correlation analysis will show a maximum peak at the value of the delay in time (τ) that both signals are shifted with respect to each other, see Fig. 4.13. This is the basic idea behind cross-correlation analysis, however the procedures applied in this project differ slightly and have some application particularities, they are explained next.

Streamline velocity correlation analysis

The analysis of the upstream traveling waves is done by means of a correlation of the turbulent component of the velocity fields, i.e. $u'(x,t)$. The correlation of the velocity values

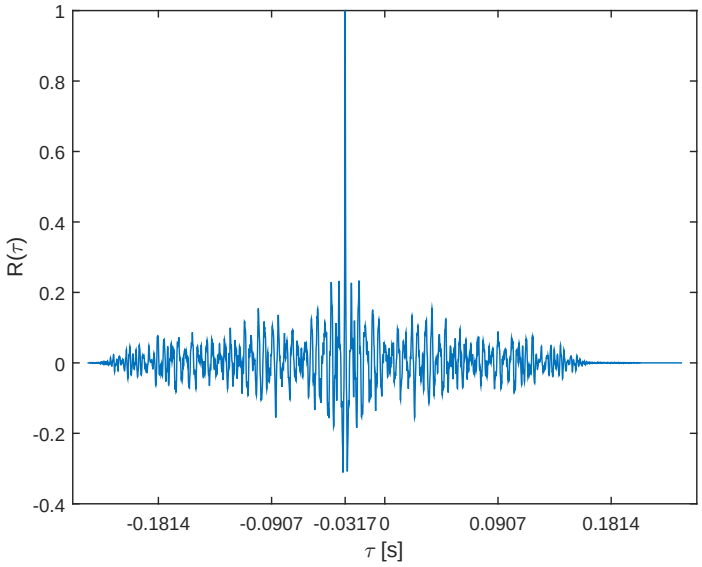

Figure 4.13: Cross-correlation function of s_1 and s_2

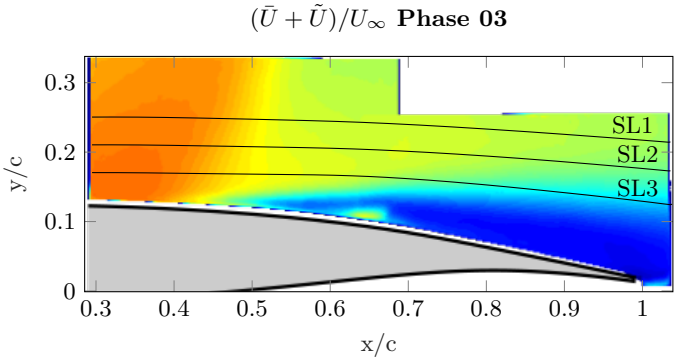

Figure 4.14: Streamlines used for the correlation analysis over the phase averaged flow field.

is done over the streamlines depicted in Fig. 4.14. These streamlines belong to the averaged flow field, so in reality they are not actual streamlines of the instantaneous velocity fields, this procedure has been chosen following the study by Hartmann et al. (2013) where they also used the averaged streamlines. Both the horizontal and the vertical velocity components are analyzed separately (u and v) as they provide different information of the phenomena occurring in the flow.

The correlation analysis follows the relation

$$R(x_0, x_1, \tau) = \int_{-\infty}^{\infty} \frac{U'(x_0,t) \cdot U'(x_1, t+\tau)}{\sqrt{U'(x_0,t)^2 \cdot U'(x_1,t+\tau)^2}} dt, \tag{4.4}$$

where two functions $U'(x_0,t)$ and $U'(x_1,t)$ are correlated with each other using a time delay τ, note that the mean value was previously subtracted from them. These functions contain the turbulent velocity variation in time at two specific locations on a streamline (x_0 and x_1), being $x_0 = x_{ref}$ the reference position. This procedure outputs a function $R(x_0, x_1, \tau)$ that

contains the correlation parameter as a function of the delay τ and that is associated with the location x_1. Now, this procedure is done not only over one particular location x_1 but it is extended through the streamline correlating all the x positions with x_{ref}, so that the final results is a whole 2D map in which for every x-location a correlation function exists that contains the correspondent correlation parameters as function of a time delay τ. Note that the reference location $x_{ref} = x_0$ is fixed and only x_1 varies along the x direction of the streamline as $0.3 \leq (x_1/c) \leq 1$. From this analysis it is expected to capture the phenomena of the flow that has a periodic nature that repeats over time at a specific frequency. Also note that there is a variation of these results depending of three main parameters, namely the streamline that is being analyzed, the velocity component (horizontal or vertical) and the reference location x_{ref}.

The upstream traveling waves are a phenomenon that creates very weak disturbances in the velocity field, therefore a direct detection of the waves is challenging and thus a statistical correlation approach is used to detect their occurrence. This is the main reason why the turbulent component of the velocity (u') is being analyzed instead of the complete velocity. It is known that these pressure waves have a characteristic frequency of about one order higher compared to buffet, so that by removing the average ($\bar{u}$) and the oscillatory ($\tilde{u}$) components the low frequency signals are largely removed and the sensitivity of the correlation analysis is increased. Furthermore, the influence of any other stronger phenomenon in the flow could mask the detection of the upstream traveling waves. In order to have an optimal detection of these waves, the proper parameters for the correlation have to be found. Firstly, the streamline SL1, see Fig. 4.14, is the best option as it is located furthest away from the influence of the pulsating separated region, while SL2 and SL3 are reached by this region when the shock moves upstream. The influence of the separated flow introduces very strong disturbances that mask the weak upstream traveling waves. Furthermore, for the correlation analysis the region of the shock wave is as well avoided, starting the correlation at horizontal positions downstream from the shock region. Secondly, these waves produce a disturbance mainly in the horizontal direction of the velocity, whereas the vertical direction is barely influenced, so a better detection of the UTW is expected from the analysis of the horizontal component of the velocity (u). Finally, the reference location x_{ref} should not be influenced by the shock wave motion as well, which means that it should be downstream from the most downstream position of the shock.

In order to further avoid the influence of the relatively low frequency flow features that are present during the buffet oscillatory motion, a high pass filter is applied. Both the shock wave motion and the pulsating character of the separated region are the features that more strongly modify the velocity fields, furthermore they both have the characteristic buffet frequency ($\sim$ 160 Hz for this experimental setup). Hence, their influence over the correlation analysis can be greatly reduced using a high pass filter, unmasking weaker disturbances. Furthermore, the instantaneous velocity fields directly obtained from the PIV post-processing show upstream traveling disturbances very clearly during the downstream shock motion, however it is barely possible to observe them during the upstream shock motion due to the presence of the largely separated flow from the shock foot. This fact suggests that there may be an actual difference in the detection, or even in the presence, of the pressure waves between both flow states. In order to account for this, the whole range of acquired velocity fields is divided in two different phases, one that corresponds to

all the time instants in which the shock is moving upstream and one for its downstream movement. By doing so it is possible to see the actual differences in the flow field between both phases. Moreover, a low-pass filter is applied too in order to analyze the flow features at frequencies near the buffet frequency. This would allow to capture the shock motion and the wake development, and to compare its behavior with that obtained from the spectral analysis.

The filter used to process the velocity signal is a Butterworth filter designed by means of Matlab inner functions. The function *butter* generates a transfer function that can be then introduced in the function *filter* to filter a signal. The Matlab inner function *butter* allows for the design of low-pass, high-pass and band-pass filters. The required input for this function is the order of the desired transfer function and the cutoff frequency, the output are the coefficients a and b of the designed transfer function that is of the form

$$H(z) = \frac{B(z)}{A(z)} = \frac{b(1) + b(2)z^{-1} + ... + b(n+1)z^{-n}}{a(1) + a(2)z^{-1} + ... + a(n+1)z^{-n}}. \tag{4.5}$$

These coefficients are inserted in the Matlab inner function *filter* that uses the transfer function $H(z)$ generated from the previous coefficients to filter the desired signal. For further information about the working principle of the Butterworth filter, the reader is referenced to Butterworth (1930). The transfer function used is of order 3 and the cutoff frequencies are 1200 Hz for the high-pass filter and 500 Hz for the low-pass filter. The value of these frequencies was chosen similarly to the study of Hartmann et al. (2013) and considering the expected frequencies of the features to be analyzed.

Wake cross-correlation analysis

For the cross-correlation analysis over the separated wake region a study area is chosen that contains the vortices traveling downstream inside the wake, see Fig. 4.15 where this area is depicted. Note that in the correlation previously done for the upstream traveling waves, the function to be correlated was a one-dimensional vector containing all the velocities in time at a specific location. However, the present cross-correlation analysis differs from the previous one. Now the function to be correlated is two-dimensional, i.e. a matrix that contains all the velocity values inside the correlation area depicted in Fig. 4.15. The correlation relation for this 2D input is slightly different, as follows

$$R(\Delta x, \Delta y, t_{i+1}) = \int_{x_a}^{x_b} \int_{y_a}^{y_b} \frac{U'(x, y, t_i) \cdot U'(x + \Delta x, y + \Delta y, t_{i+1})}{\sqrt{U'(x, y, t_i)^2 \cdot U'(x + \Delta x, y + \Delta y, t_{i+1})^2}} dxdy, \tag{4.6}$$

where $U'(x, y, t_i)$ and $U'(x, y, t_{i+1})$ are the velocity matrices from two consecutive instants of time, namely t_i and $t_{i+1} = t_i + \Delta t$ respectively. x_a, x_b, y_a and y_b indicate spatial boundaries. The result will be a 2D matrix that shows the correlation parameter values as function of the spatial delay in both the x and y directions, e.g. Δx and Δy respectively. This cross-correlation between image pairs is done over time varying $0 \leq t_i \leq t_f$, where t_f is the measuring time. All correlation maps obtained are then averaged and scaled to get a single final correlation map.

By correlating the velocity matrices at two consecutive instants of time it is possible to obtain the total displacement of the elements inside the correlation area. This allows

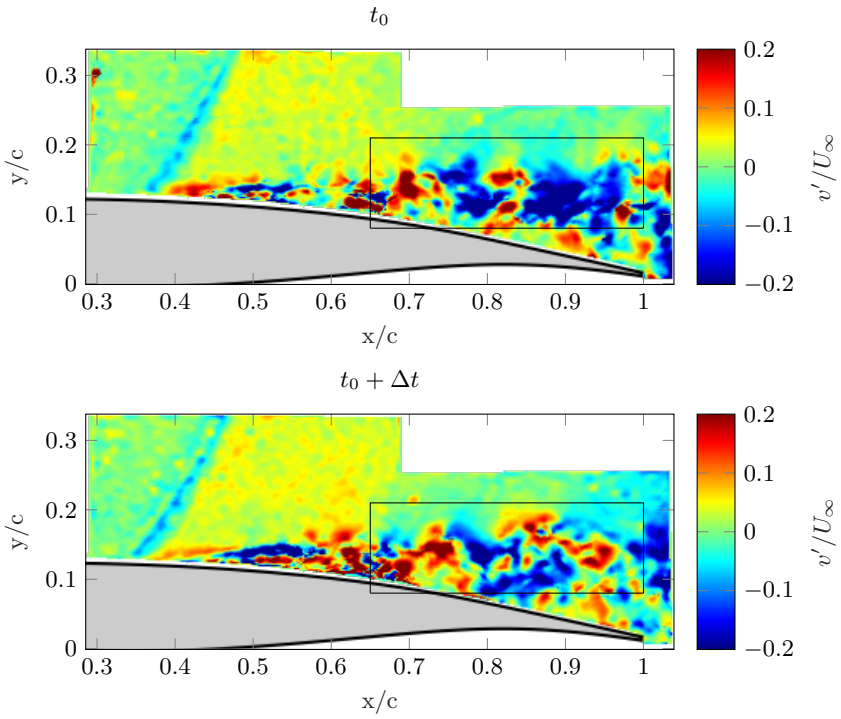

Figure 4.15: Example of the cross-correlation area of the separated region

for the computation of an estimated velocity for the displacement of the vortices, i.e. the velocity at which the vortices are convected downstream.

Wake auto-correlation analysis

Similarly to the previous cross-correlation analysis, the auto-correlation analysis of the separated wake region is done over a study area chosen as it is done in each of the images of Fig. 4.15. The only difference is that for the auto-correlation only one instant of time is used, and the matrix of velocities obtained from the study area is correlated with itself. This leads to the following correlation function,

$$R(\Delta x, \Delta y, t_i) = \int_{x_a}^{x_b} \int_{y_a}^{y_b} \frac{U'(x, y, t_i) \cdot U'(x + \Delta x, y + \Delta y, t_i)}{\sqrt{U'(x, y, t_i)^2 \cdot U'(x + \Delta x, y + \Delta y, t_i)^2}} dx dy. \tag{4.7}$$

The aim of this analysis is to capture the distance between the vortices present in the wake at one particular instant of time. The auto-correlation map will show a maximum peak at the origin, i.e. at $\Delta x = 0$ and $\Delta y = 0$, since the maximum auto-correlation parameter of a function is with itself. Furthermore, a second weaker peak is expected that shows the distance between two vortices present in the study area. As it can be expected, this analysis will show good results only in the cases where the vortices are really well defined against the background of the image. In order to get an average distance, the analysis is done over all the time instants available in the data set and then averaged.

Chapter 5

Flow field description

Before starting the detailed explanation of the analysis performed over the results and before immersing the reader into the mathematical and physical procedures used to study the phenomena taking place in the flow, this chapter presents a description of the overall flow field. The aim is to introduce the main features of the flow and, hence, to ease the understanding of the different steps taken during the project and the reasons that led to this particular direction. Firstly, a study of the boundary layer transition over the airfoil surface is included, as this phenomenon is of paramount importance for the development of buffet. Secondly, a description is made of the overall flow field development, then an analysis of the unsteady flow behavior is done, focusing on the description of the instantaneous buffet cycles and the phase-average fields. Furthermore, the features of the flow where the analysis is focused are described and reasoned.

Table 5.1 shows the cases studied with PIV where the shock wave is unsteady. It contains the mean shock position, its standard deviation and the shock motion character (periodic or non periodic). From this table it is concluded that the present chapter will focus on the case of the OAT15A at $\alpha = 3.5^\circ$ and $Ma = 0.70$, since it presents a periodic shock wave motion with the highest standard deviation. This is the case where buffet is more fully developed, as it is corroborated in Chapter 7 by means of a spectral analysis of the shock motion.

	NACA0012 $\alpha = 0°$			OAT15A $\alpha = 0°$		
Ma	$(\bar{x}/c)_s$	$(x/c)_{rms}$	Shock motion	$(\bar{x}/c)_s$	$(x/c)_{rms}$	Shock motion
0.78	0.55	3.58%	Periodic	0.68	3.01%	Periodic
	NACA0012 $\alpha = 2°$			OAT15A $\alpha = 2°$		
Ma	$(\bar{x}/c)_s$	$(x/c)_{rms}$	Shock motion	$(\bar{x}/c)_s$	$(x/c)_{rms}$	Shock motion
0.70	-	-	-	0.48	5.30%	Periodic
0.73	-	-	-	0.55	4.60%	Periodic
0.75	0.63	3.00%	Periodic	-	-	-
	NACA0012 $\alpha = 4°$			OAT15A $\alpha = 3.5°$		
Ma	$(\bar{x}/c)_s$	$(x/c)_{rms}$	Shock motion	$(\bar{x}/c)_s$	$(x/c)_{rms}$	Shock motion
0.70	0.52	2.64%	Periodic	0.48	7.01%	Periodic
0.73	-	-	-	0.48	3.85%	Periodic
0.75	0.71	4.07%	Periodic	-	-	-

Table 5.1: Shock motion characteristics based on the PIV results

5.1 Airfoil transition analysis

Boundary layer transition from laminar to turbulent regime over the airfoil surface plays an important role in the present experiments as it greatly influences the shock wave-boundary layer interaction, hence influencing buffet itself. For the analysis of buffet, a transitioned boundary layer is desired due to its stronger stability and span wise homogeneity. The NACA0012 model is expected to present natural transition near the leading edge, whereas the behavior of the OAT15A boundary layer is not known. This led to this airfoil transition analysis in which the aim was to analyze by means of oil flow visualization the nature of the boundary layer under the influence of different transition trips. The main goal was to make a decision about which tripping device should be applied in the experiments.

In order to estimate an approximate boundary layer thickness (δ) at the tripping device location ($x/c = 7\%$) it is possible to use integral analysis over a flat plate as an approximation. The aim is to have an idea of the limiting values for the thickness of the tripping device. In order to compute such estimation for the present experiments, the following relation is derived in Appendix B, and using the standard conditions presented in Table 3.2 as follows,

$$\delta = \frac{5\sqrt{x \cdot c}}{\sqrt{Re}} = \frac{5\sqrt{0.007 \cdot 0.1}}{\sqrt{2.763 \cdot 10^6}} \approx 0.08 \quad [mm] \tag{5.1}$$

Note that the small order of magnitude of the length that results from this approach, 0.08 mm, makes complicated to measure this exact thickness on the airfoil models. Looking at Table 3.1 it is observed that the Carborundum that fits the size requirements is carborundum 150 with a particle size of 0.075 mm, however note that the carborundum transition trips are directly glued over the surface by means of spray glue, which leads to an extra thickness due to the glue layer. Since this thickness cannot really be controlled it was decided as a solution to try different carborundum sizes and to analyze the result by means of oil

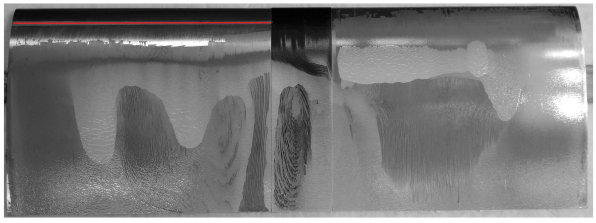

Figure 5.1: Oil visualization of NACA0012 at $\alpha = 4$ and $Ma = 0.70$. Fixed transition with Carborundum 500 (in red) on the left, free transition on the right. Leading edge at the top.

visualization to obtain a qualitative verification of the transition process over the OAT15A model. Carborundum 150, 320, 400 and 500 were tested, with particle sizes that vary from 0.075 mm to 0.0139 mm, furthermore a zig-zag trip of 2 mm thickness was tested. Moreover, the carborundum 500 was also tested over the NACA0012 in order to check the actual free transition of the boundary layer. Note that in the following images the leading edge is on the top and the trailing edge on the bottom.

Starting with the NACA0012 airfoil, Fig. 5.1 shows the model at flow conditions of $\alpha = 4°$ and $Ma = 0.70$. Carborundum 500 has been used to fix transition at $x/c = 7\%$ on the left half-span region, whereas free transition occurs on the right half-span region. Both regions are separated by black dc-fix foil. It can be observed in the image, by looking at the most upstream region, that transition occurs indeed on both sides under these particular flow conditions. This is concluded knowing that under laminar boundary layer conditions, the shear stress between the flow and the oil is less than under turbulent conditions. This entails that turbulent boundary layers wash down the oil more effectively, as seen in the figure. On the right side it is observed that actually transition starts before $x/c = 7\%$, so the presence of the transition trip is not really necessary for transition purposes.

Focusing now on the OAT15A airfoil at $\alpha = 3.5$ and $Ma = 0.71$ (Fig. 5.2), it can be observed in a) that free transition does not occur, i.e. the boundary layer remains laminar up to the shock foot. In this image (a), the effect of the walls can be clearly observed, the flow has a decreasing velocity towards the walls which tends to move the shock wave upstream on the airfoil. This translates into the straight lines that appear at around 45° with respect to the flow direction and that mark the shock wave location. Furthermore, the neat oil visualization achieved in this case shows the bi-dimensional character of the buffet flow, with a quasi straight shock line in the span direction. However, it is observed that a 3D effect is taking place in the separated region after the shock, caused by the wall effect.

Since transition does not occur freely, different carborundum trips are tested in order to check the different effects they have over the flow. Images b), c), d) and e) represent the carborundum 150, 320, 400 and 500 respectively, note that only in image b) the trip covers all the span length, whereas in the rest the trip is placed on the right side of the model. All the trips trigger transition as expected, and actually there is not an observable difference between the four different cases. It is also interesting to see how the free transition side of these images (left side) present turbulent spots (dirt particles) near the leading edge that

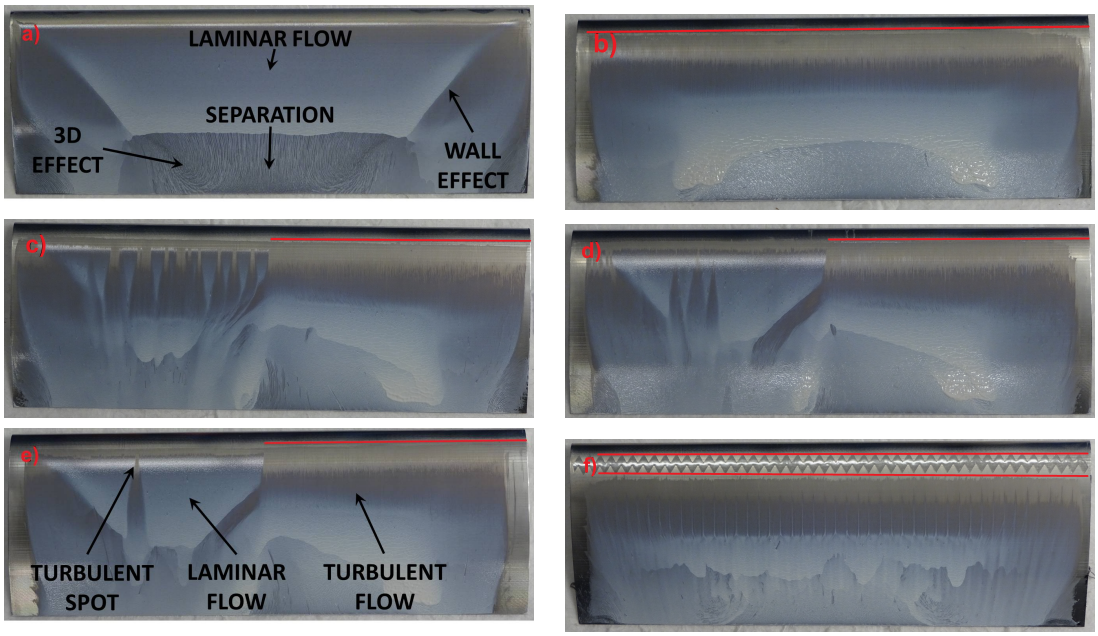

Figure 5.2: Oil visualization of OAT15A at $\alpha = 3.5$ and $Ma = 0.71$. a) Free transition, b) Carb. 150, c) Carb. 320, d) Carb. 400, e) Carb. 500 and f) Zig-Zag. Leading edge at the top and transition trip in red.

automatically trigger a strong transition. This is an important reason why to use trips, since the laminar boundary layer is very unstable and highly affected by these dirt particles.

Finally, the zig-zag trip with a thickness of 2 mm was tested to corroborate the hypothesis that such a large thickness falls outside of the boundary layer and not only causes transition but it affects the outer flow. In image f) it is observed that the trip actually acts as a vortex generator, so it cannot be used for transition purposes unless with a reduced thickness.

5.2 Flow field general overview

The aerodynamic conditions of Mach number, Reynolds number and angle of attack that are objective of this research project define a flow field that is enclosed in the compressible lower transonic regime as it was described in Fig. 1.2, since it is precisely in this regime where the unsteady phenomenon of buffet occurs. Fig. 5.3 presents the basic flow field development as a function of the Mach number for values comprised between $Ma = 0.5$ and $Ma \approx 1$ inside the lower transonic regime. The expected flow state for the present experimental project is the one that coincides with the cases $Ma = 0.77$ and $Ma = 0.82$ in Fig. 5.3, where a normal shock wave is observed in the suction side of the airfoil, with the possible presence of a secondary and weaker normal shock in the pressure side.

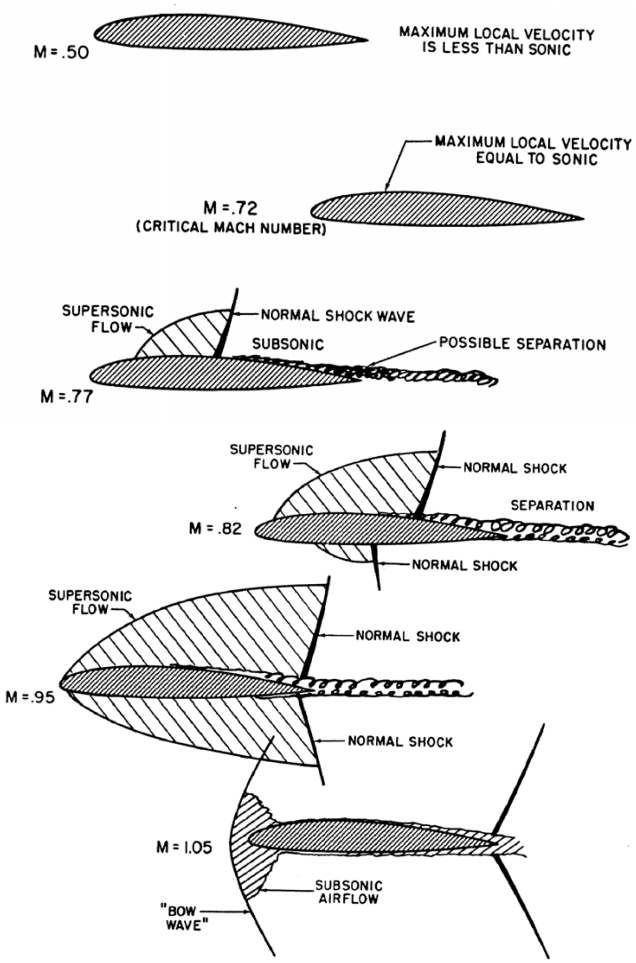

Figure 5.3: Lower transonic flow development

In this regime a supersonic region is expected to appear above the upper surface of the airfoil (also in the lower surface under certain conditions). The supersonic region starts near the leading edge during the expansion of the flow and it is terminated downstream by a normal shock wave. The mean shock position depends on the free stream Mach number, for increasing Mach it moves downstream, eventually reaching the trailing edge. Under buffet conditions it is known that the position of this normal shock is not steady but it oscillates in cycles about the mean position. In order to corroborate whether the actual flow obtained in the experiments agrees with this flow description Fig. 5.4 shows a Schlieren image and its corresponding velocity field obtained by PIV under the same aerodynamic conditions. The OAT15A airfoil is shown at $\alpha = 3.5$ and $Ma = 0.70$ by means of Schlieren visualization on the left and particle image velocimetry on the right. The Schlieren image also shows the fields of view used for the PIV measurements, region of the flow that coincides with the PIV image.

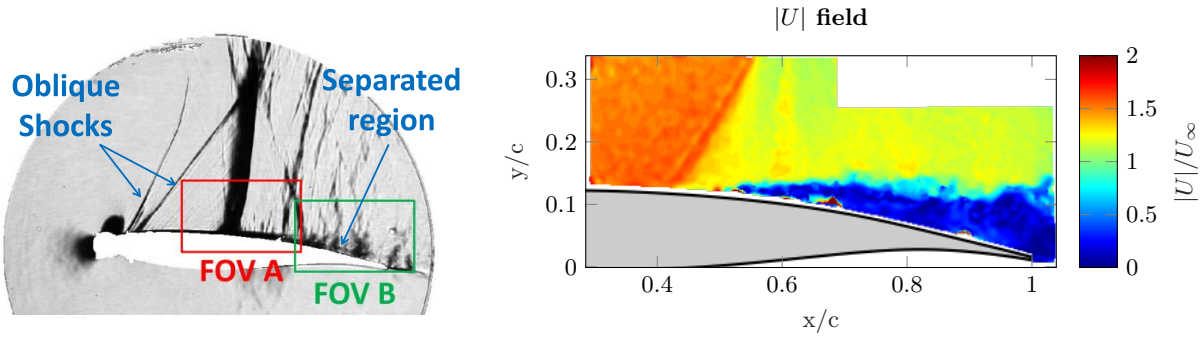

Figure 5.4: Instantaneous flow field over OAT15A. Schlieren image with PIV FOVs sketches (left) and PIV image (right)

It is observed in Fig. 5.4 the presence of a supersonic region on the upper surface terminated by a quasi-normal shock wave positioned at about 50% of the chord. The supersonic region is more clearly depicted in the PIV image, where a strong and almost instantaneous velocity gradient is observed. Note that in the Schlieren image the presence of two additional oblique shocks is observed which are caused by the presence of the carborundum strip that is installed to force boundary layer transition. The importance of these shocks is actually negligible as demonstrated by Jacquin et al. (2009), however they are very prominent in the Schlieren image due to the spanwise integration of the light deviation, that tends to amplify the contrast. For the present conditions no shock wave is observed on the lower side, this however may be different for other free stream Mach numbers and angles of attack. Furthermore, in both images separation takes place from the shock foot and it extends beyond the trailing edge, however for lower shock strengths (different Mach, α) the flow may remain attached. Note the presence of sound pressure waves that travel upstream in the outer region downstream from the shock wave in the Schlieren image.

The analysis of the buffet phenomenon entails dealing with highly unsteady flow fields due to the shock motion and the evolution of the separated region. The flow just described is an instantaneous image from a particular flow case studied, so it does not provide much information about the flow development itself. In order to address that aspect, the next sections focus on the description of the flow taking into account its unsteady behavior.

5.3 Unsteady flow behavior

The buffet phenomenon consists of an oscillatory periodic motion of the shock wave around a mean position at a certain frequency that depends on the flow conditions. This shock motion is actually part of a feedback loop that includes other features. These are the periodic development of the separated region, the shedding of vortices from the shock foot and the development of upstream traveling waves. These waves are originated at the trailing edge and impinge on the shock wave from behind, allegedly forcing its movement. This section shows the images obtained from Schlieren and the velocity fields from PIV that describe the

cyclic and periodic motion of the phenomenon, including all the features that form part of the feedback loop just described. The aim is to demonstrate and investigate the existence of such feedback loop components and to ease its understanding for a posterior deeper analysis, focused on the actual physical link between them that permits the self-sustained character of the phenomenon.

The section is divided in three parts that are linked with different descriptions of the velocity fields that can be made based on this triple decomposition. The first part is dedicated to the description of the mean flow, i.e. $\bar{u}(x)$. The second part focuses on the analysis of the instantaneous velocity fields, i.e. $\vec{u}(x,t)$. Finally, the last part describes the phase average flow fields, i.e. $\bar{u}(x) + \tilde{u}(x,t)$.

5.3.1 Mean flow $\bar{u}(x)$

The average flow velocity field or mean flow computed from PIV results over a fully developed buffet case, i.e. the flow over the OAT15A at $\alpha = 3.5$ and $Ma = 0.70$ with fixed transition at $x/c = 7\%$, is shown in Fig. 5.5. It can be noted that there is not a sharp shock location as could be expected in a steady case where the shock would not change its location and the separated region would have a constant size. Instead, a progressive gradient of velocity is observed in the downstream direction, that develops between an upstream supersonic region and a downstream subsonic region, as a consequence of the shock cyclic motion. Another important feature is the smeared separation region, in average starting from the shock foot and extending up to the trailing edge, a very characteristic property of fully developed buffet flows. The separated region from shock foot to trailing edge is described in the literature as a necessary condition for buffet phenomenon to occur, at least during the part of the cycle when the shock wave moves in the upstream direction.

The average velocity flow field does not give enough information about the buffet characteristics as it is time independent and the unsteady information is lost in the average. For a deeper analysis of the characteristics that define the shock motion cycles and their effect over the rest of the flow, the instantaneous and the phase average flow fields are analyzed next.

5.3.2 Instantaneous flow fields $\vec{u}(x,t)$

In order to see the effect of the buffet phenomenon it is interesting to look at the instantaneous flow field over an oscillation cycle for fully developed buffet conditions. A proper analysis of this instantaneous field is important as it should contain the actual physical evolution of every feature involved in the feedback loop of the phenomenon. The features of the flow that play a major role in the buffet cyclic development can be listed as

- the shock motion,

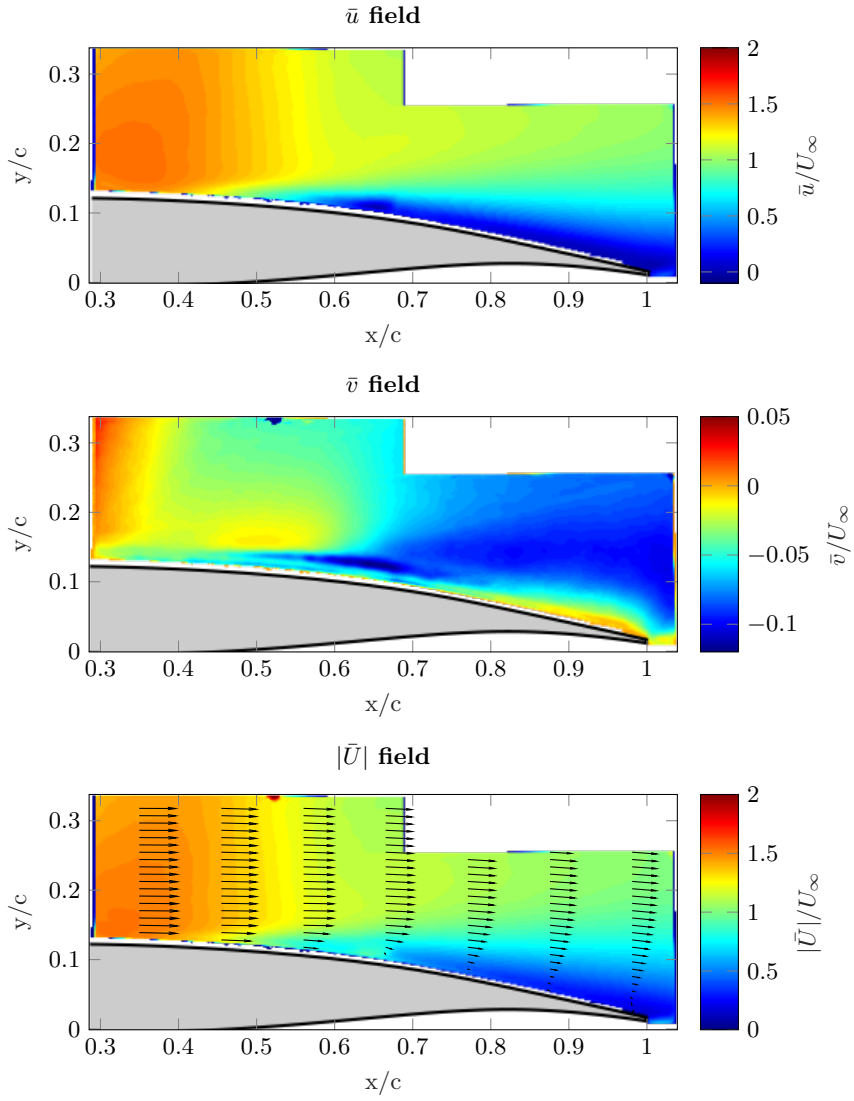

Figure 5.5: Average flow field over OAT15A at $\alpha = 3.5°$ and $Ma = 0.70$, horizontal $\bar{u}$ (top), vertical $\bar{v}$ (middle) and total $|\bar{U}|$ (bottom) velocities

- the shock wave-boundary layer interaction (SWBLI),
- the evolution of the separated region,
- the vortex shedding,
- the creation and evolution of the upstream traveling waves (UTW) and
- the interaction between UTW and shock wave.

All these features are physically linked creating a closed self-sustained cycle. Such physical relations have been studied in the literature over the years, however some of them are not yet fully clear and understood. For instance the relation between the vortex shed and the upstream traveling waves with the shock motion, phenomena whose characteristic frequencies differ in order of magnitude. Furthermore, there is not much research behind the UTW that fully demonstrates and explains their real effect.

The instantaneous flow fields in Figs. 5.6 and 5.7 show a complete buffet cycle over the OAT15A airfoil at $\alpha = 3.5°$ and $Ma = 0.70$ with transition triggered at $x/c = 7\%$, conditions under which buffet is fully developed. The flow field is shown by means of Schlieren visualization images (Fig. 5.6) and velocity fields from the time-resolved planar particle image velocimetry (Fig. 5.7). The cycle is shown in 8 steps, the first one (t_0) related to the most downstream position of the shock, then three more showing the upstream travel of the shock wave. After them, the most upstream position of the shock ($t_0 + 13\Delta t$ in Fig. 5.6, and $t_0 + 27\Delta t$ in Fig.5.7) and finally three more frames showing the downstream travel of the shock wave. Note the different magnitude of Δt for the Schlieren and PIV images, 0.25 ms in the former and 0.125 ms in the later, i.e. exactly half as the PIV acquisition frequency used was 8 kHz while for Schlieren it was set to 4 kHz. It is observed from both the Schlieren and the PIV flow fields how the shock position develops in time, traveling upstream from the most downstream position at about $x/c = 60\%$ (at t_0) to the most upstream position at about $x/c = 37\%$ (at $t_0 + 13\Delta t$ in Fig. 5.6, and $t_0 + 27\Delta t$ in Fig.5.7) and then, traveling downstream to complete one buffet cycle. During this cycle, not only a development in time of the shock position is observed, but also of the rest of features involved that were previously mentioned. In the literature the frequency of the phenomenon is usually computed by analyzing the varying pressure values in time at specific points of the flow field. Taking, for instance, the results from Jacquin et al. (2009) over the same aerodynamic model, the OAT15A, his results can be used to make an estimate of the expected frequency for the buffet phenomenon in the present study, by computing the Strouhal number (Str). In his experiments, Jacquin et al. (2009) used an airfoil with a chord length of $L_{Jac} = 230$ mm and at $\alpha = 3.5$ and $Ma = 0.73$ he measured a buffet frequency of $f_{Jac} = 69$ Hz. For the present experiments, the same airfoil with a chord length of $L = 100$ mm has been used. If one considers the same flow conditions, the Strouhal number is constant and hence the expected frequency for buffet is computed as,

$$Str = \frac{f \cdot L}{U_\infty} \quad \Rightarrow \quad \frac{Str_{Jac}}{Str} = \frac{f_{Jac} \cdot L_{Jac}}{f \cdot L} \quad \Rightarrow \quad f = \frac{f_{Jac} \cdot L_{Jac}}{L} \approx 160 \quad Hz. \tag{5.2}$$

Where the subscript Jac refers to the results obtained by Jacquin et al. (2009). Hence, a frequency of the order of 160 Hz is expected for the buffet phenomenon in the present

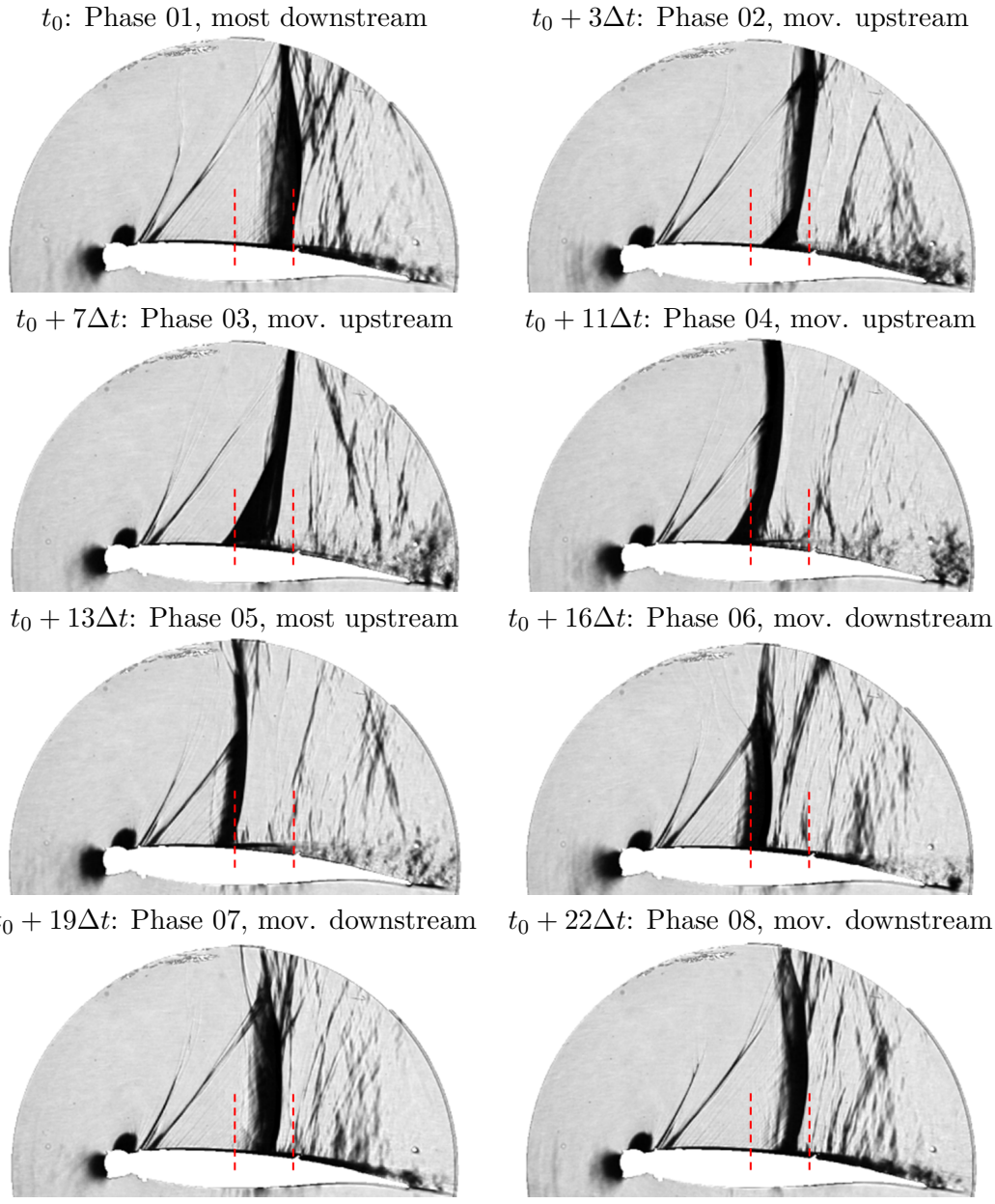

Figure 5.6: Flow field at buffet flow for one oscillation cycle over OAT15A at $\alpha = 3.5°$ and $Ma = 0.70$, $\Delta t = 0.25$ ms. Most upstream and downstream shock positions marked in red.

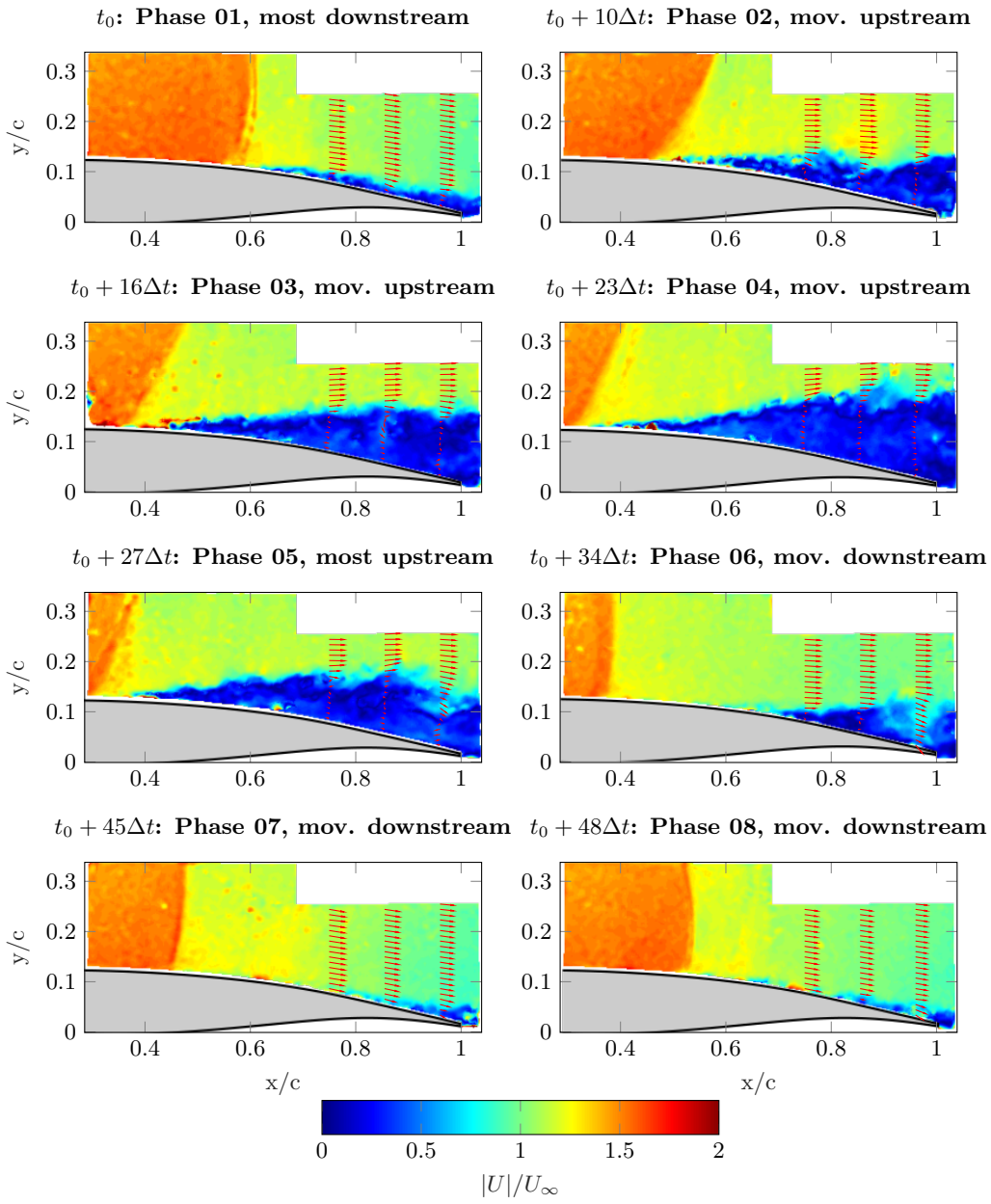

Figure 5.7: Instantaneous velocity field $|U|$ at buffet flow for one oscillation cycle over OAT15A at $\alpha = 3.5°$ and $Ma = 0.70$, $\Delta t = 0.125$ ms.

experiments. Note that this frequency entails a period of $T = 1/f = 6.3$ ms for a buffet cycle, which in turn is in quite good agreement with the time period of the cycles described in Figs. 5.6 and 5.7. The period in Fig. 5.6 is $\sim 0.25 \cdot 25\Delta t \approx 6.3$ ms, and in Fig. 5.7 is $\sim 0.125 \cdot 50\Delta t \approx 6.3$. Nevertheless, the actual buffet frequency will be obtained and studied with a proper frequency analysis in Chapter 7.

Analyzing the shock motion, a remarkable difference can be noticed between the upstream and the downstream movements. During the upstream travel, the shock moves as an oblique shock whereas during the downstream movement it does as a quasi-normal shock. This can be corroborated by the actual flow deflection that occurs through the shock wave during its upstream travel, observable in Fig. 5.10 by a dramatic increase of the vertical velocity component. This fact has indeed noteworthy importance as it demonstrates that there is a substantial difference between the nature and causes of the upstream and downstream movements, in contra position with some of the hypothesis developed in the literature. The difference between these natures is related to the link of the shock motion with the rest of the features involved.

Starting from the most downstream position of the shock wave and during its upstream movement, the shock wave-boundary layer interaction plays a role of great importance. This interaction falls in the category of a strong interaction as it clearly produces a massive separation at the shock foot that extends up to the trailing edge, this is observable in both the Schlieren and the PIV results. Focusing on the development of the upstream motion, the shock is quasi-normal at its most downstream position. However, separation is suddenly triggered from the shock foot creating a massive separated wake that changes the effective geometry of the surface. This forces a flow deflection after the shock, that can only be achieved by a deflection of the shock wave itself, becoming an oblique shock. This oblique character is maintained during the whole upstream movement, until it weakens, and reattachment occurs near the most upstream shock position. It is then when the shock returns to its quasi-normal character. Now, it is not clear how the massive separation affects the upstream movement of the shock.

The shock wave has velocity zero at its most upstream and downstream locations, while its velocity is maximum about halfway of its upstream and downstream travel. The difference in direction of the shock motion causes that its relative velocity with respect to the flow is maximum during the upstream travel and minimum during the downstream travel, see Fig. 5.8. This translates at the same time into a modulation of the shock strength, that will be higher during the upstream movement than during the downstream one. This is the reason why during most part of the upstream travel the separated region grows bigger, due to an increasing shock strength and a stronger SWBL interaction. While traveling upstream the shock encounters regions of decreasing pressure and higher flow speeds that, eventually, will force the shock motion to stop. At this point the shock strength has decreased as well as the size of the separated region. Under these conditions the shock starts its downstream travel.

When the shock starts moving downstream its strength decreases due to a decreasing relative speed of the flow. This entails that the SWBL interaction gets weaker and reattachment occurs at the shock foot. Under these conditions the shock tends to return to its original position moving downstream as a quasi-normal shock. Note that the oblique

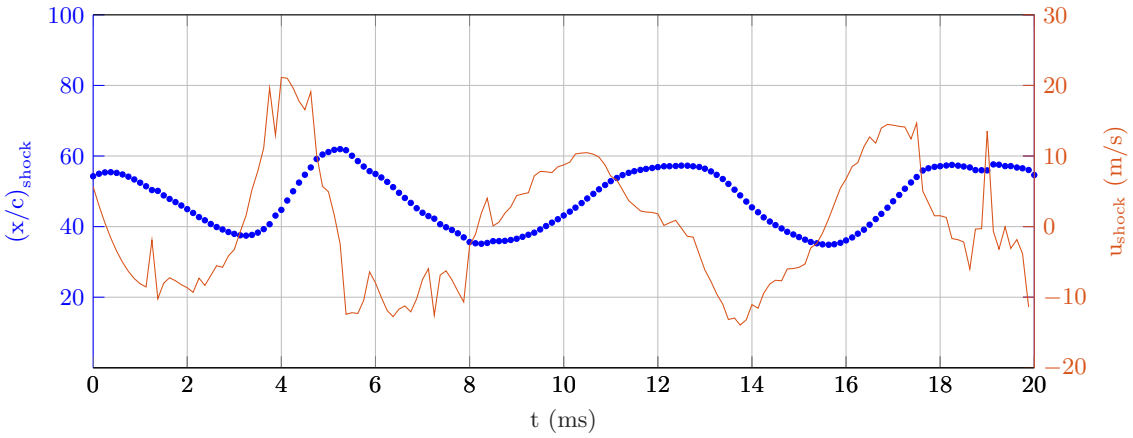

Figure 5.8: Shock position and velocity in time for 3 oscillations of OAT15A at $\alpha = 3.5°$ and $Ma = 0.70$

character of the shock is lost as soon as reattachment takes place at the shock foot, this can be observed in image $t_0 + 34\Delta t$ of Fig. 5.7. Furthermore, note in the images that separation still exists at the trailing edge region, but it does not reach the shock foot. Then, once the shock reaches its most downstream position the cycle starts all over again in a self-sustained manner. It is precisely this point of the cycle, the triggering of the upstream movement, where the upstream traveling waves, originated at the trailing edge of the airfoil, play a major role as demonstrated by Hartmann et al. (2013). These waves are powerful enough to force the shock wave out of its equilibrium state and to start the self-sustained cycle.

5.3.3 Phase-average flow fields $\bar{u}(x) + \tilde{u}(x,t)$

The instantaneous flow fields presented before show the information for a specific instant of time, however, normally it is of great importance to analyze the average flow field as it gives clear information of the general state of the flow. Nevertheless, when the phenomenon is unsteady but periodic as in this case, the normal average flow field (Fig. 5.5) is not the best option, since the cyclic information is lost. For this purpose the phase-average is introduced. The phase-average velocity fields contain two components of the velocity triple decomposition, namely $\bar{u}(x) + \tilde{u}(x,t)$, the average component and the oscillatory component that is time dependent. This field is needed in order to obtain the turbulent component $u'(x,t)$ for a posterior correlation analysis.

Fig. 5.9 shows the phase-average fields of the horizontal velocity component $\bar{u}(x) + \tilde{u}(x,t)$, Fig. 5.10 shows the vertical velocity component $\bar{v}(x) + \tilde{v}(x,t)$ and Fig. 5.11 shows the total velocity $\bar{U}(x) + \tilde{U}(x,t)$ (where $U = \sqrt{u^2 + v^2}$) for the same aerodynamic case, the OAT15A at $\alpha = 3.5$ and $Ma = 0.70$ with forced transition at $x/c = 7\%$. Note that in the images $\bar{x}$ refers to the mean shock position and Δx to its standard deviations. Fig. 5.9 shows a very similar flow description as the instantaneous flow field showed in Fig. 5.7. It is observed how

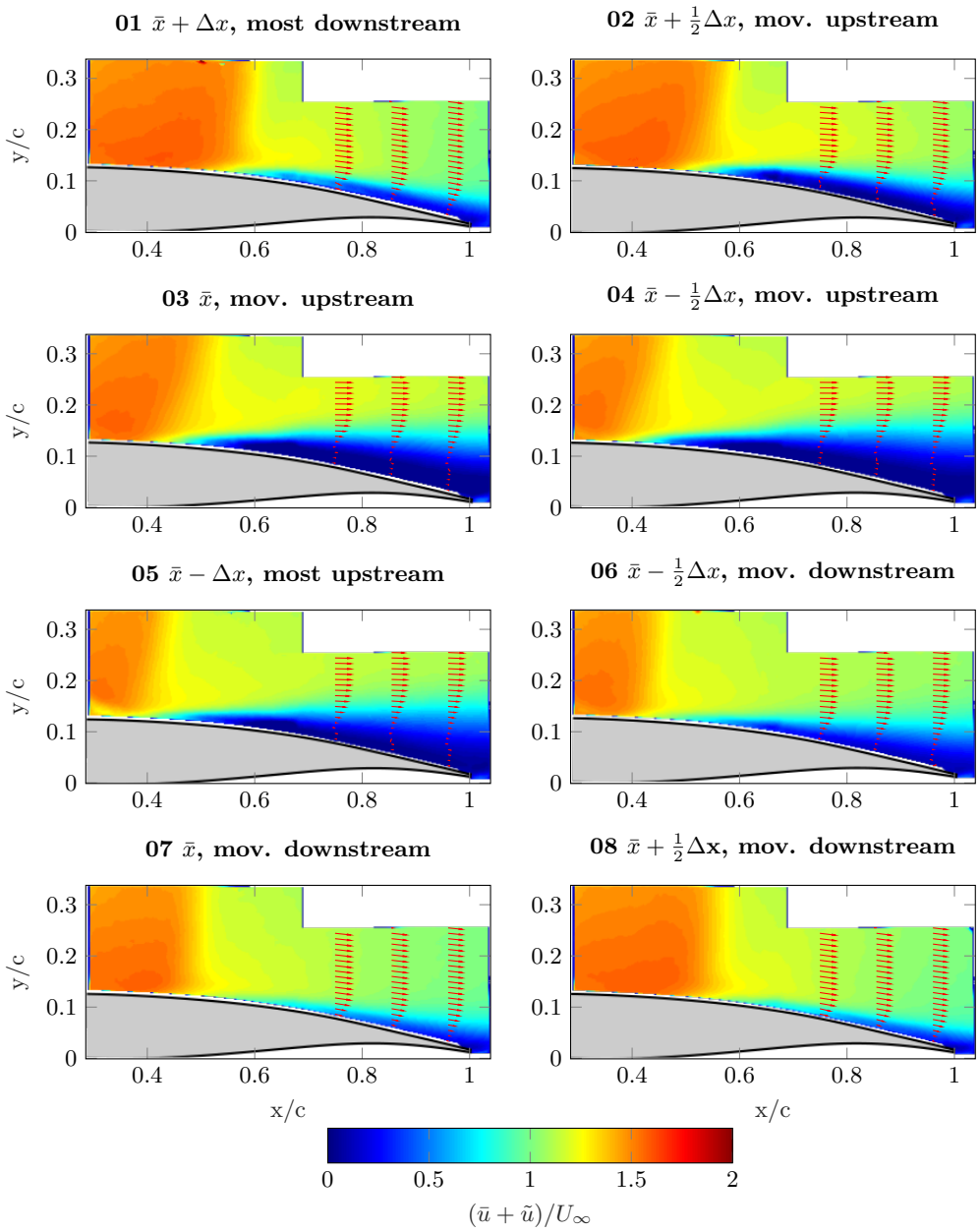

Figure 5.9: Phase average horizontal velocity field $(\bar{u} + \tilde{u})$ over OAT15A at $\alpha = 3.5°$ and $Ma = 0.70$. Phase 01) most downstream position; Phases 02, 03, 04) upstream travel; Phase 05) most upstream position; Phases 06, 07, 08) downstream travel of the shock wave.

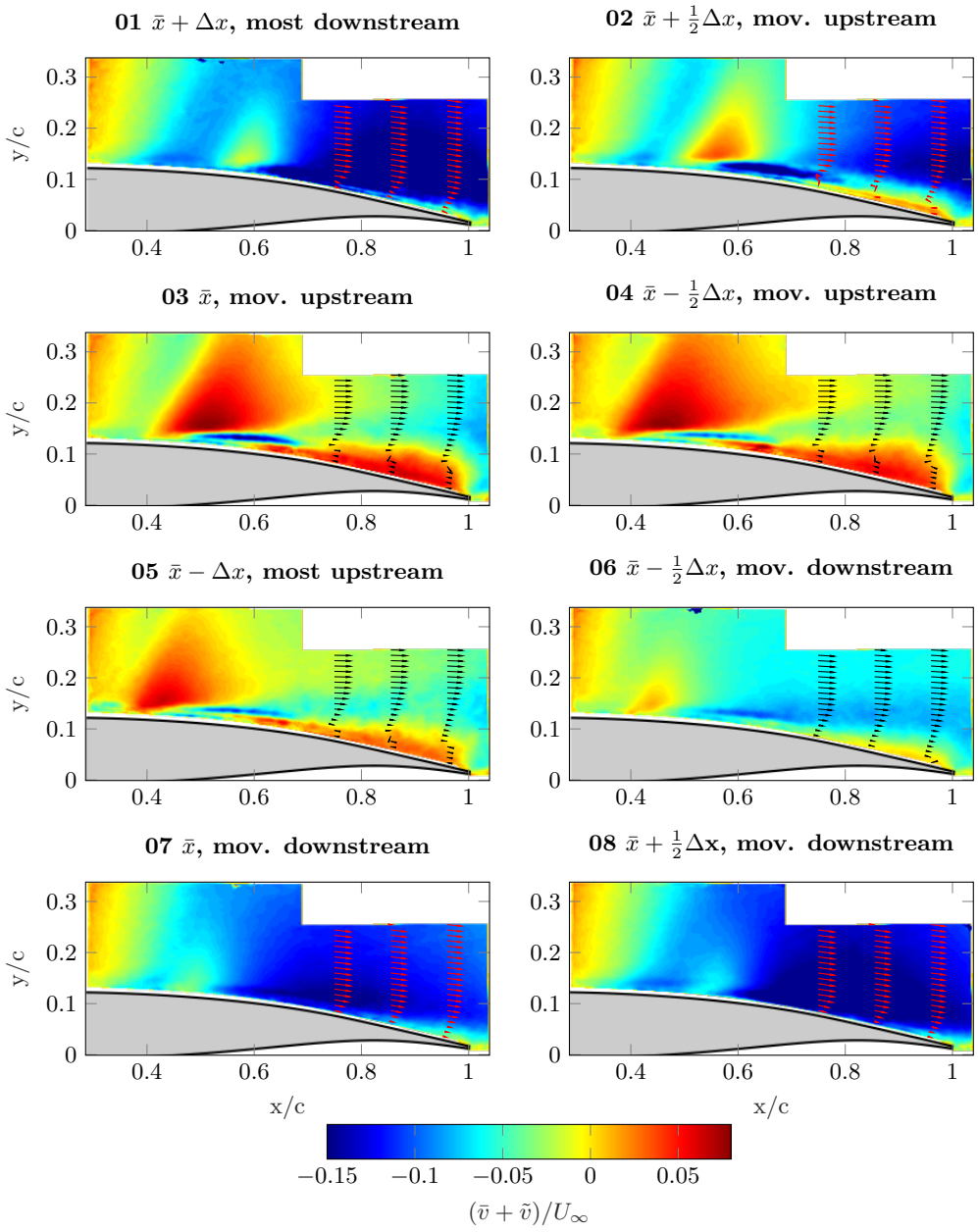

Figure 5.10: Phase average vertical velocity field $(\bar{v} + \tilde{v})$ over OAT15A at $\alpha = 3.5°$ and $Ma = 0.70$. Phase 01) most downstream position; Phases 02, 03, 04) upstream travel; Phase 05) most upstream position; Phases 06, 07, 08) downstream travel of the shock wave.

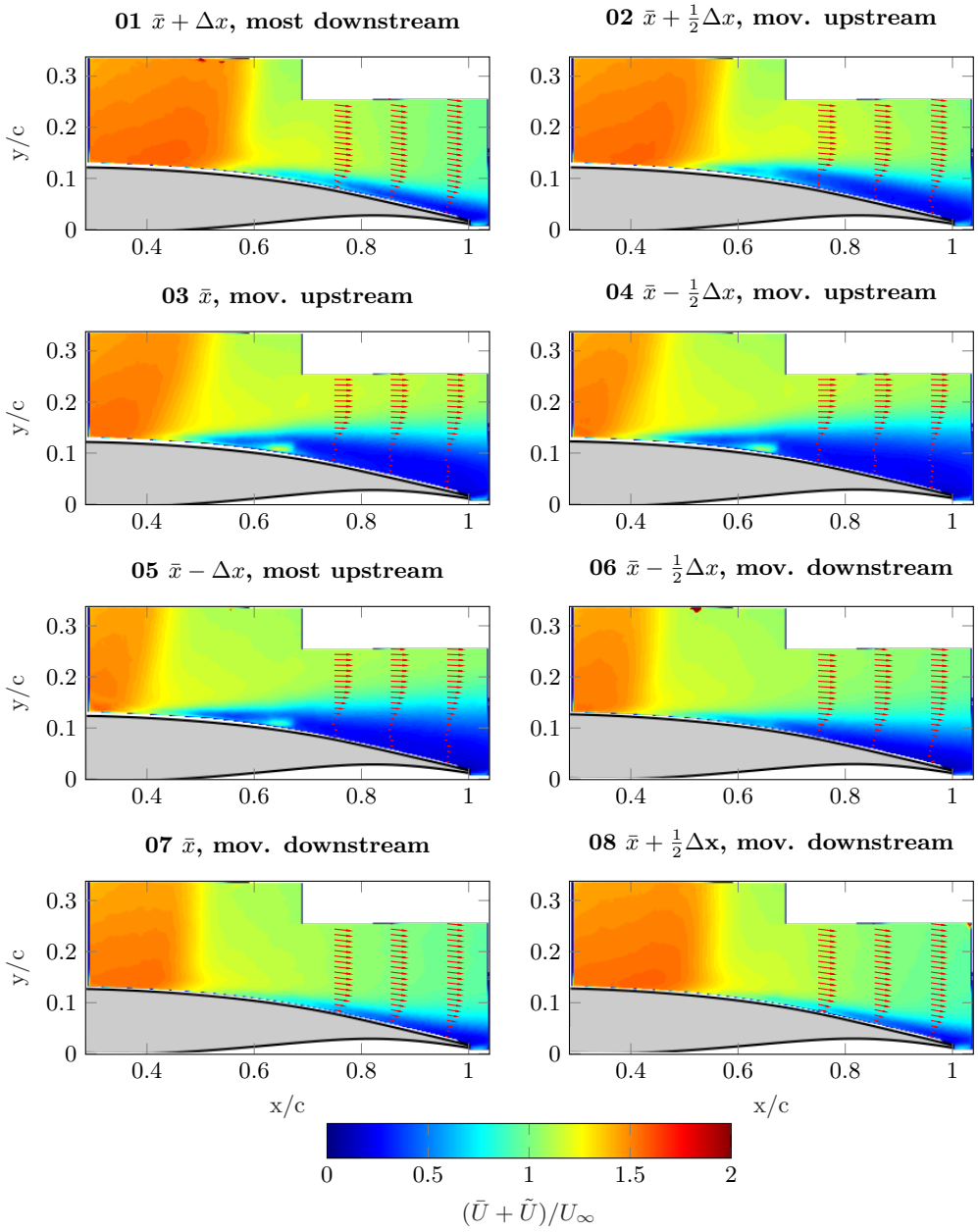

Figure 5.11: Phase average total velocity field ($\bar{U}+\tilde{U}$) over OAT15A at $\alpha = 3.5°$ and $Ma = 0.70$. Phase 01) most downstream position; Phases 02, 03, 04) upstream travel; Phase 05) most upstream position; Phases 06, 07, 08) downstream travel of the shock wave.

the separated region grows during the upstream travel of the shock wave and then decreases with reattachment at the shock foot during the downstream travel. Note that the largest separated region occurs in the phase just before the most upstream shock position, i.e. phase 04. This means that it is precisely in this phase when the strongest vortices are being shed into the flow from the shock foot. On the other hand, Phases 07 and 08 show the smallest separated region, which means weaker vortices being shed. In general, the phase-average of the horizontal velocity corroborates all the conclusions drawn over the instantaneous flow field from Fig. 5.7. Note in Fig. 5.11, that the total velocity field is basically dominated by the horizontal component, while the vertical component is important only at the shock foot and the separated regions. In this figure, a recirculating bubble is observed between $x/c = 0.6 - 0.7$ during the upstream motion of the shock wave (phases 2 to 5).

On the other hand, a very interesting effect appears in the phase-average vertical velocity fields. It can be observed in Phases 02 to 05 that when separation appears at the shock foot and it increases in size, the effective geometry of the airfoil changes. This is observable in the fact the vertical velocity increases dramatically in that region after the shock wave, leading to an upwards deflection of the flow. At the same time, this is related to the oblique character that the shock acquires during its upstream movement and that permits such deflection, starting from the shock foot and extending to the rest of the shock.

Fig. 5.12 shows the vertical profiles of the phase-average horizontal velocity component $(\bar{u} + \tilde{u})$ for 4 different phases (1, 3, 5 and 7) at $x/c = 90\%$. A clear difference is observed between the upstream shock motion (phases 3 and 5), where the wake is massively separated from the shock foot and back flow recirculation is observed near the trailing edge surface, and the downstream shock motion (phases 1 and 7), where reattachment occurs at the shock foot. An interesting feature that demonstrates the effect of the blockage produced by the separated region is that the outer flow under the presence of such region reaches velocities higher than the free stream.

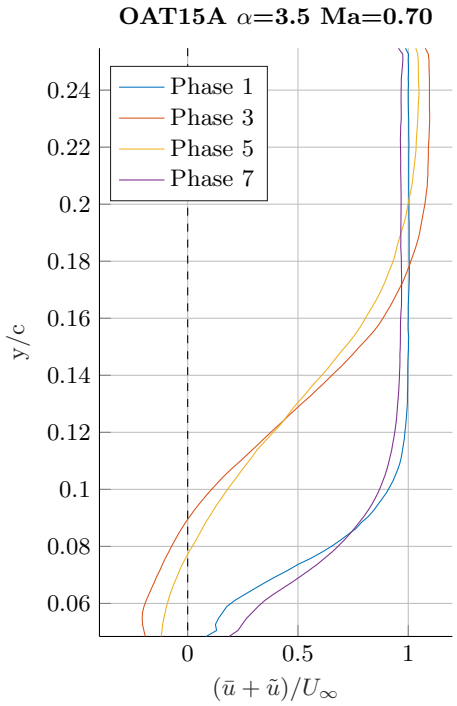

Figure 5.12: $(\bar{u} + \tilde{u})$ velocity profiles at $x/c = 90\%$ of phases 1,3, 5 and 7.

5.4 Comparison of unsteady flow behavior

The phase-average velocity fields $(\bar{u} + \tilde{u})$ give information about the unsteady development of the buffet phenomenon under specific aerodynamic conditions. In this section a comparison is intended of the aerodynamic case, labeled as *reference case*, presented in Section 5.3, i.e. OAT15A airfoil at $Ma = 0.70$ and $\alpha = 3.5°$, against the *buffet case* for the NACA0012 and cases of the OAT15A under different flow conditions of Mach number and angle of incidence. The aim is to analyze the differences that the buffet flow phenomenon creates over the flow field if compared to cases where it is not fully developed.

a) NACA0012 at $Ma = 0.70$, $\alpha = 4°$ and free transition

Fig. 5.13 depicts the *buffet case* of the NACA0012 airfoil, i.e. the case where buffet was found to be best developed. This case allows to compare the flow field under the same aerodynamic conditions but a different airfoil model. One important difference is observed if compared to the reference case from Section 5.3 where buffet was fully developed, it is that the separated wake is barely affected by the displacement of the shock, i.e. there is not a substantial growth during the upstream movement, nor reattachment during the downstream movement. Furthermore, the standard deviation of the shock motion is $(x/c)_{rms} = 2.64\%$, notably smaller compared to the $(x/c)_{rms} = 7.01\%$ from the reference case.

b) OAT15A at $Ma = 0.70$, $\alpha = 2°$ and fixed transition at $x/c = 7\%$

This case allows to analyze the effect of varying angle of attack over the flow field see Fig. 5.14. It is observed that separation at the shock foot never takes place, and the flow becomes separated only at the trailing edge region. Hence, the shock motion is not related to a development of the separated wake, which suggests the solely effect of the so called *upstream traveling waves*. The standard deviation of the shock motion is $(x/c)_{rms} = 5.3\%$, considerably high, and higher than in the case of NACA0012 at $Ma = 0.70$, $\alpha = 4°$. It is important to note that in this case the buffet phenomenon is highly developed even without massive separation taking place at the shock foot.

c) OAT15A at $Ma = 0.73$, $\alpha = 3.5°$ and fixed transition at $x/c = 7\%$

This case allows to analyze the effect of varying Mach number on the flow field, see Fig. 5.15. The increased flow speed creates a stronger shock wave and separation is present at the shock foot during the whole buffet cycle with no reattachment. The size of the wake is barely affected by the shock motion and the standard deviation of the shock motion is $(x/c)_{rms} = 3.85\%$. Note that, in contrast to the reference case, the oblique character of the shock wave near the shock foot is maintained throughout the whole buffet cycle, due to the permanent presence of separation at the shock foot.

Velocity profiles of a), b) and c)

Fig. 5.16 shows the vertical profiles of the phase-average horizontal velocity component $(\bar{u}+\tilde{u})$ for 4 different phases at $x/c = 90\%$ for the three cases just discussed (a, b and c). Despite the fact that in the NACA0012 airfoil, case a), separation occurs always from the shock foot, no recirculation takes place and the outer velocities are below the free stream value. In case b) separation occurs always in the trailing edge region with no recirculation. In case c), due to the massive constant separation at the shock foot, recirculation is always present at the trailing edge region, furthermore the outer velocities have greater values than the free stream. It has been shown, that for the OAT15A cases, recirculation is observed at the trailing edge whenever massive separation occurs at the shock foot, see also Fig. 5.12. Note that the conditions at the trailing edge just described are of paramount importance to understand the creation of the so called *upstream traveling waves* that actually occurs in this region.

Conclusions of transition analysis

These tests were used to determine if a tripping device would be needed for the experiments based on the boundary layer state, and in that case, what would be the best option. For the NACA0012 it was concluded that no tripping device was necessary since transition occurs freely near the leading edge due to the high curvature of the airfoil, furthermore this decision agrees with the literature where this airfoil was used under free transition conditions for buffet analysis.

On the other hand, for the OAT15A model, the transition trip is needed as it does

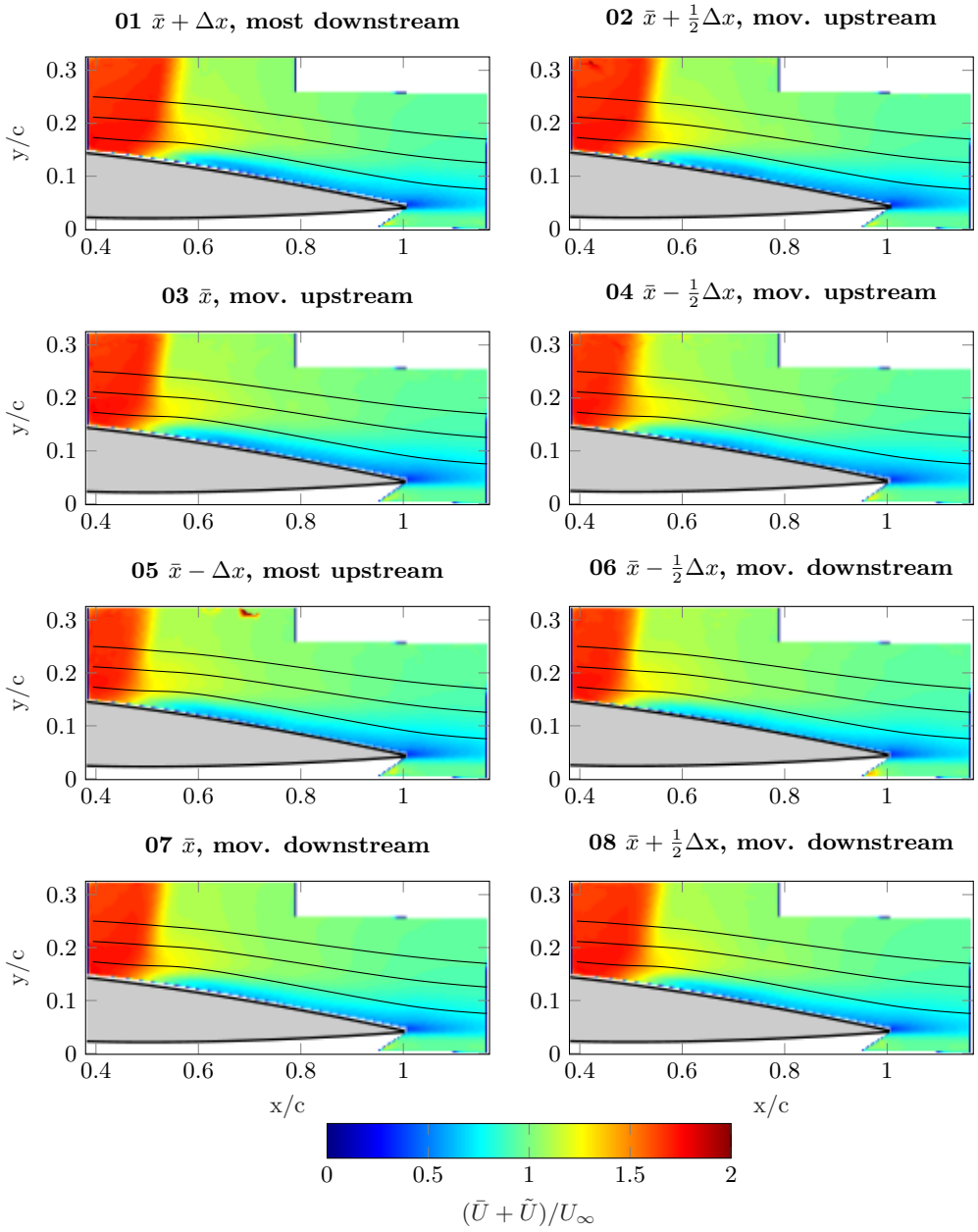

Figure 5.13: Phase average total velocity field $(\bar{U} + \tilde{U})$ over NACA0012 at $\alpha = 4°$ and $Ma = 0.70$. Phase 01) most downstream position; Phases 02, 03, 04) upstream travel; Phase 05) most upstream position; Phases 06, 07, 08) downstream travel of the shock wave.

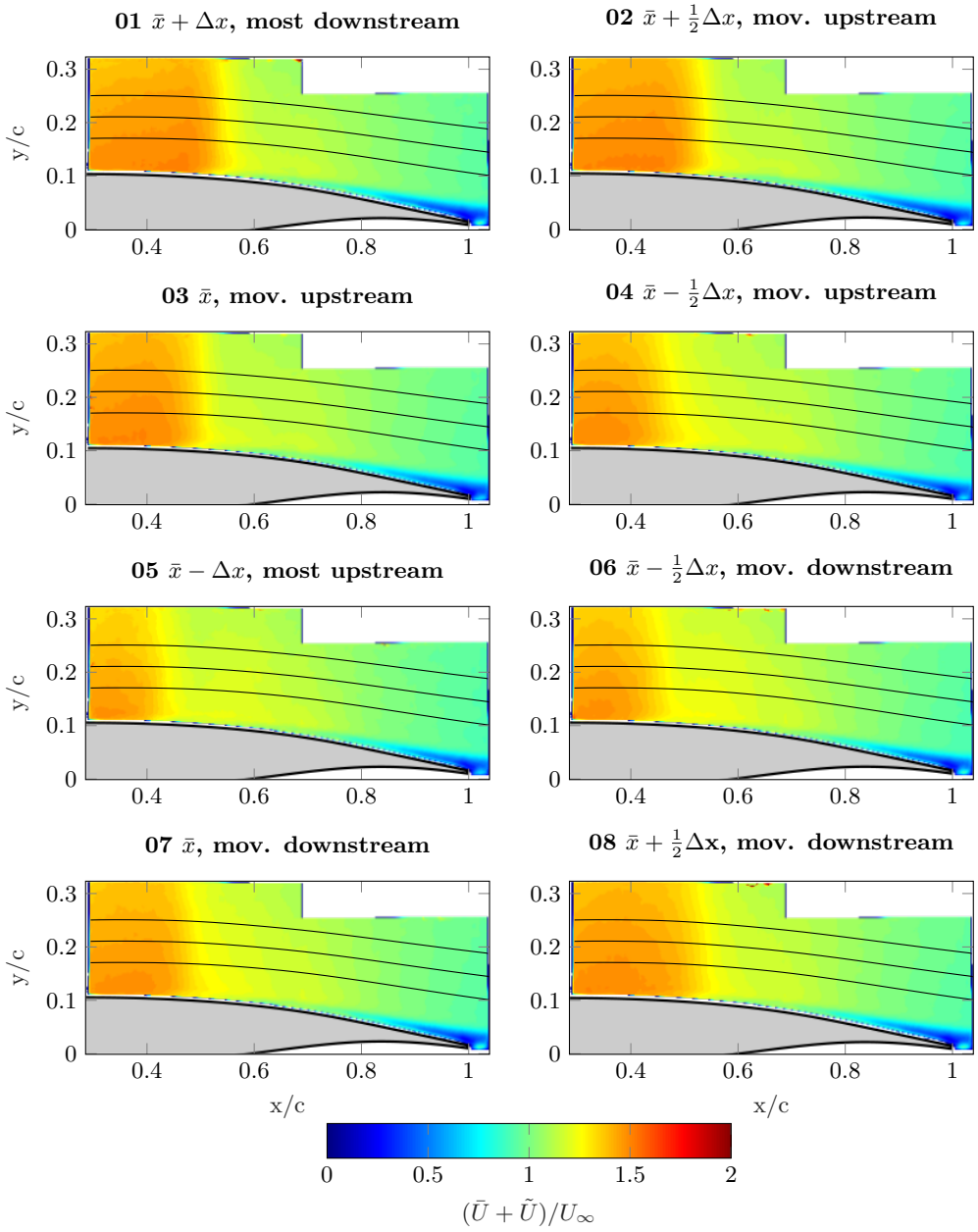

Figure 5.14: Phase average total velocity field $(\bar{U} + \tilde{U})$ over OAT15A at $\alpha = 2°$ and $Ma = 0.70$. Phase 01) most downstream position; Phases 02, 03, 04) upstream travel; Phase 05) most upstream position; Phases 06, 07, 08) downstream travel of the shock wave.

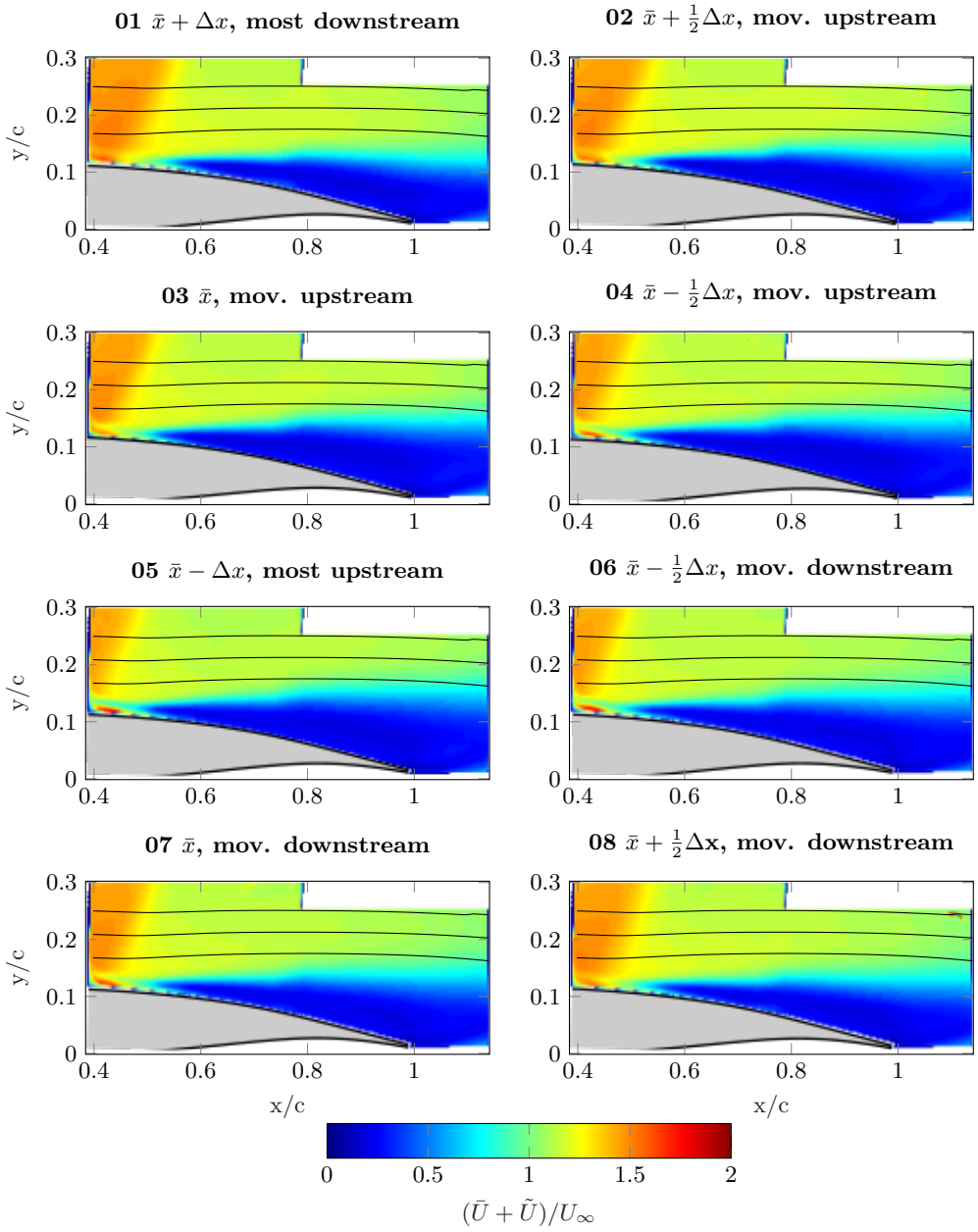

Figure 5.15: Phase average total velocity field ($\bar{U}+\tilde{U}$) over OAT15A at $\alpha = 3.5°$ and $Ma = 0.73$. Phase 01) most downstream position; Phases 02, 03, 04) upstream travel; Phase 05) most upstream position; Phases 06, 07, 08) downstream travel of the shock wave.

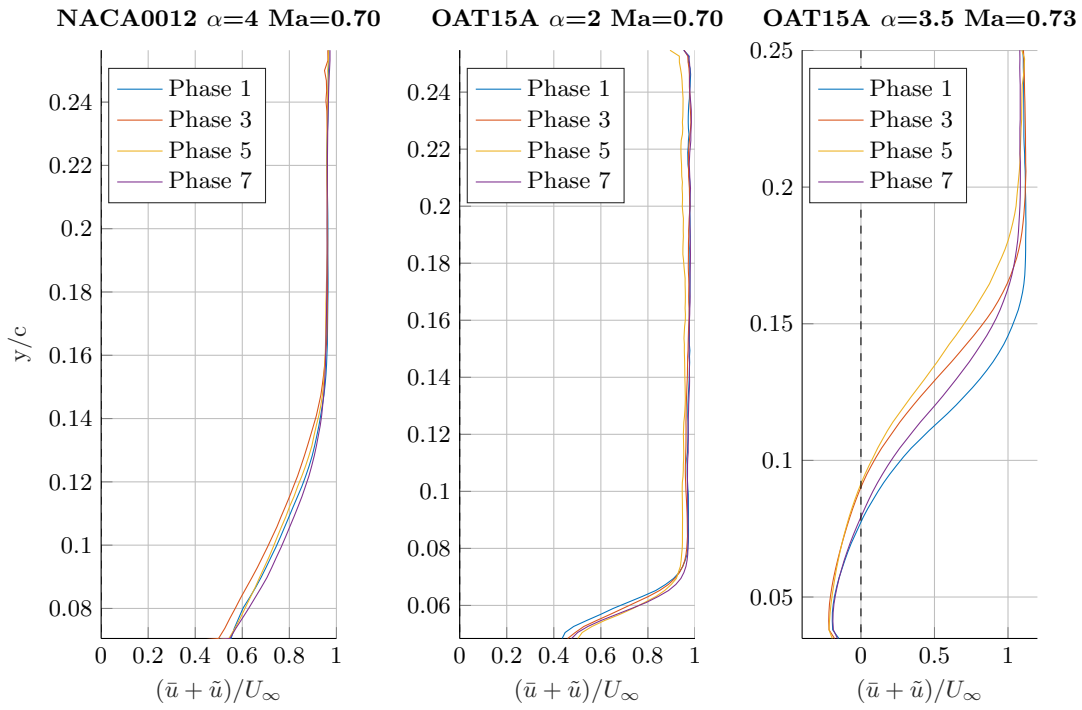

Figure 5.16: $(\bar{u} + \tilde{u})$ velocity profiles at $x/c = 90\%$ of phases 1,3, 5 and 7.

not occur freely. The limiting lengths given by the calculations of Re_k (0.07 mm) and boundary layer thickness δ (0.08 mm) suggested the Carborundum 150 (0.075 mm of particle size) as the appropriate option to fix transition. However, these tests demonstrated that all the trips trigger transition similarly, so the decision was made to use the smallest particle size for the experiments, namely Carborundum 500. The reasoning behind this decision is simply that it would perturb less the boundary layer while still triggering transition.

Chapter 6

Wind tunnel related noise analysis

Tests were conducted using the empty test section in order to analyze possible disturbances inside the wind tunnel previous to the analysis of the airfoil results. The aim of this analysis is to asses whether there is noise inside the tunnel in the form of coherent pressure waves that can affect the flow around an airfoil located in the test section, hence interacting with the buffet phenomenon. In order to do such analysis, the technique used was Schlieren as it allows for a clear visualization of possible pressure waves traveling through the test section, at different stages of the facility. The results obtained can be then studied in the frequency domain, showing the characteristic frequencies of such disturbances.

6.1 Empty test section without laser probe

Two different Mach numbers were tested, 0.75 and 0.80, in order to study its effect over the tunnel noise and to check whether its strength increases or remains bounded. In general the noise travels downstream and upstream through the test section in the form of pressure waves. Note the absence of the laser probe in the tunnel in these experiments, which would have an important effect over the test section. From the experimental results it can be noticed by plain view the existence of pressure waves that cross the test section in the upstream direction.

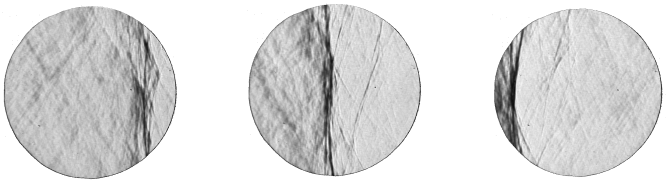

Figure 6.1: Pressure wave traveling upstream through the test section at t_0 (left), $t_0+\Delta t$ (center) and $t_0+2\Delta t$ (right). Flow goes from left to right and the waves displace in the opposite direction.

The frequency analysis, in this particular case, is done over the density gradients acquired time-wise at fixed locations in the flow. The actual variable given by the Schlieren system is the light intensity, which translates into the density gradient of the flow at such points. The variations observed in density are due to the pressure waves that go through the test section in either direction, hence the frequency peaks refer to the frequency of appearance of such waves.

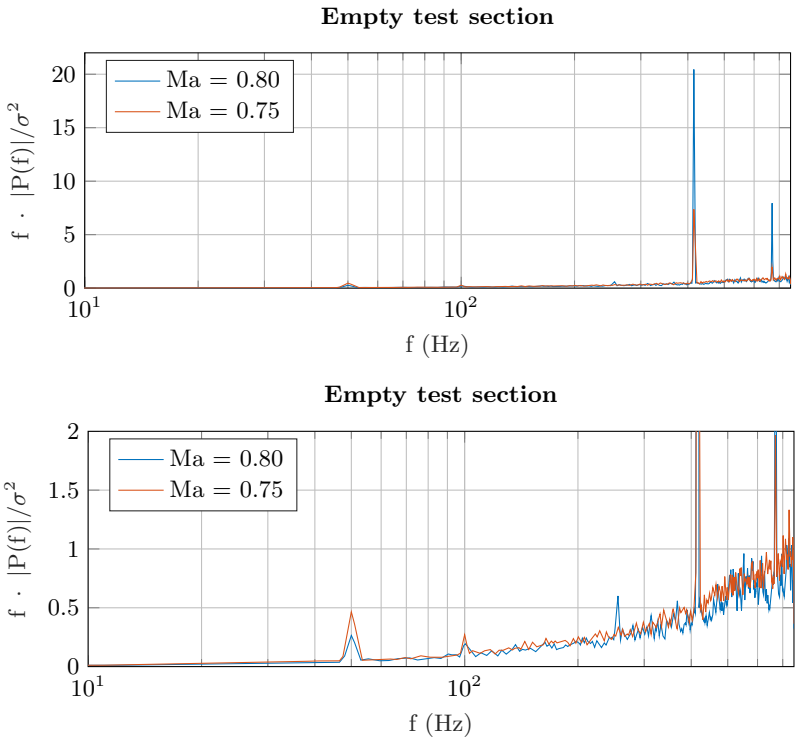

Figure 6.2: Frequency spectrum of the flow density gradients through the empty test section without laser probe. Standard scale (top), reduced scale (bottom)

Fig. 6.2 shows several predominant peaks in the frequency spectrum, where the amplitude $f \cdot |P|/\sigma^2$ is directly related to the energy of the phenomenon. The main peaks are located, in ascending frequency, at 50, 100, 255, 415 and 670 Hz. The peak at 415 Hz has the highest amplitude. The peak at 50 Hz and its harmonic at 100 Hz correspond to the electrical current oscillations of the illumination system, whereas the rest are due to the noise inside the wind tunnel. The most powerful noise sources are associated to frequencies of 415 and 670 Hz, furthermore, these peaks are highly affected by the Mach number as their amplitude increases by a factor 3 to 4. The energy of the rest of the peaks is much smaller, however it is worth to take note of their existence as they may appear magnified in the model experiments. An important feature of these peaks that may be highlighted is that their frequency appears to be unaffected by the Mach number increment. In principle this should not happen as the Strouhal number is conserved, i.e. a variation of the flow speed from state A to a state B

should be translated into a frequency variation as follows,

$$Str = \frac{f \cdot L}{U_\infty} \quad \Rightarrow \quad \frac{U_\infty^A}{f^A} = \frac{U_\infty^B}{f^B}. \tag{6.1}$$

The reason why the peaks do not change in frequency may be because they are originated in a region of the tunnel where the speed is constant, for instance, the choke. An estimate of the characteristic lengths associated to these frequencies can be computed by an approximation of the local flow conditions. This can give an idea of the part of the tunnel were the source of the waves is located for future possible research focused on finding the wind tunnel noise sources. For a measured total temperature of 280 K and a Mach number of 0.75 the flow speed is computed as

$$U_\infty = M \cdot \sqrt{\gamma \cdot R \cdot T_s} = 0.75 \cdot \sqrt{1.4 \cdot 287.058 \cdot 252} \approx 240 \quad [m/s]. \tag{6.2}$$

And after applying the appropriate velocity corrections, see 3.4.1, it is $U_\infty \approx 248$ m/s. Based on this velocity, the characteristic lengths are computed for $St = 1$ from Eq. 6.1 as

$$L = St \cdot \frac{U_\infty}{f} \quad \Rightarrow \quad \begin{cases} f = 670 \quad Hz \quad \Rightarrow \quad L \approx 0.4 \quad m \\ f = 415 \quad Hz \quad \Rightarrow \quad L \approx 0.6 \quad m \\ f = 255 \quad Hz \quad \Rightarrow \quad L \approx 1.0 \quad m \end{cases} \tag{6.3}$$

Although the actual physical source of these peaks is not clear, it is important to note that their nature is unrelated to the buffet phenomenon. Otherwise, they could be misleading in the interpretation of posterior results related to the transonic phenomenon.

6.2 Empty test section with laser probe

The effect of the laser probe is first studied over the empty test section in order to analyze whether it acts as a source of possible upstream traveling disturbances or whether it has an effect over the wind tunnel noise shown in Fig. 6.2. One of the effects that the probe may cause is a peak near 3000 Hz caused as a result of the upstream traveling waves, see Appendix B.3.However, there can also be an indirect influence, more related to a possible variation of the wind tunnel noise levels due to the presence of the laser probe. Fig. 6.3 shows the Fourier Transform of the light intensity signal variation in time, captured by the Schlieren system for three different Mach numbers. It aims at making a comparison with the case without probe from Fig. 6.2.

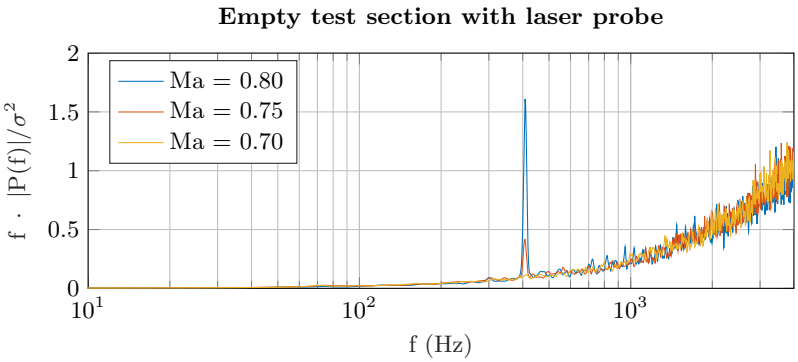

Figure 6.3: Frequency spectrum of the flow density gradients through the empty test section with the presence of the probe inserted 50%

Similarly to the case with no laser probe, Fig. 6.2, a peak is observed in the vicinity of 400 Hz, exactly at 408 Hz. However, no peak appears in the region of 3000 Hz as expected. The reason for this cannot be exactly stated only from these results, a possible explanation is that the strength of such pressure waves is below the sensitivity threshold of the Schlieren system. Another option is that during their upstream travel the waves get damped and lose strength due to dissipation along the distance between the probe and the test section, a total of 8 times the airfoil chord distance (0.8 m). Note the absence of the peaks at 50, 100, 255 and 670 Hz that were present in the case without laser probe.

An important difference between the cases with and without probe is the magnitude of the 400 Hz peak signal, i.e. $f \cdot |P(f)|$, which is of the order of 10 times smaller in the case with the laser probe. This fact would suggest that the main effect of the laser probe is that it reduces the noise level and the disturbances caused by the tunnel itself. However, it is important to note that both cases were studied in different experimental campaigns and, hence, with different Schlieren system setups. For the empty test section analysis the Fourier transform is performed over the acquired light intensity versus time at specific locations of the flow field. Since the experimental setups were different, two important parameters that allow for the comparison between the two cases of this analysis are different too, the first one is the average light intensity and the second one, the average fluctuation magnitude of the signal. In order to account for these differences Parseval's theorem is used to scale the results. This theorem, also known as Rayleigh's energy theorem, is actually derived from the more general mathematical Plancherel theorem. It states that the integral of the square of a function modulus is equal to the integral of the squared modulus of its frequency spectrum. For the current analysis, a discrete Fourier transform, the theorem becomes

$$\sum_{n=0}^{N-1} |x[n]|^2 = \frac{1}{N} \sum_{k=0}^{N-1} |X[k]|^2, \tag{6.4}$$

where $x[n]$ is a discrete time signal, $X[k]$ is the discrete Fourier transform of $x[n]$ and N is the size of both functions. Taking $x[n]$ as the original function minus the average $x[n] =$

$x_0[n] - x_{aver}$, the left hand side can be substituted by the variance of x as

$$\sum_{n=0}^{N-1} |x_0[n] - x_{aver}|^2 = \frac{1}{N} \sum_{k=0}^{N-1} |X[k]|^2 \quad \Rightarrow \quad \sigma^2 = \sum_{k=0}^{N-1} |X[k]|^2, \tag{6.5}$$

This leads to the possibility of scaling the discrete Fourier transform with its variance, allowing for the comparison between different cases. This is exactly what was done in Figs. 6.2 and 6.3, a scaling of the y-axis by means of its variance ($f \cdot |P(f)|/\sigma^2$) so that the differences in light average and standard deviation from average were taken into account and a comparison between their magnitudes was possible.

Despite the aforementioned, a proper comparison of the signal magnitude from the Fourier analysis of both cases with and without probe cannot be realistically done. The reason is that the acquisition frequencies and the spatial resolutions used in the experiments are different, leading to a difference in the total amount of energy enclosed under the curve in the graphs. However, although an exact direct comparison is not possible, one can get an overall idea of the probe effect by performing a "pseudo" signal-to-noise ratio approach. Considering the relative magnitude of the peak at 400 Hz with respect to the overall level of noise of the rest of the signal taken at a given frequency. The case with no probe (Fig. 6.2) shows a signal-to-noise ratio of about 20 for Ma=0.8 and taking the overall signal at about 700 Hz, meaning that the peak magnitude is around 20 times higher than the rest of the signal. On the other hand, the case with probe (Fig. 6.3) shows a ratio of around 8 for the same conditions. Based on this, a guess can be made that the effect of the probe is actually to decrease the magnitude of the noise coming from the tunnel. However, it must be noted that the overall background noise may have increased due to the presence of the probe. The physical mechanism of this guess cannot be exactly identified with these results, but it could be conjectured that it has to do with the interference of the noise waves with the laser probe and the vortices it sheds into the flow. Further analysis would be required if the real mechanism and exact effect of the probe is desired, possibly by means of pressure measurements.

Chapter 7

Buffet spectral analysis

The present chapter deals with the frequency analysis of the shock motion, results obtained from Schlieren Visualization and PIV measurements. It focuses on finding the range of aerodynamic conditions under which buffet develops, and on the spectral characteristics of the shock wave motion. The same analysis is performed over the results from both experimental techniques in order to verify their similarity and reproducibility and to capture any possible incongruity. The processing applied to obtain these results can be found in Section 4.1.

The frequency analysis covers the effect of the main aerodynamic parameters over the development and strength of the buffet phenomenon, i.e. the effect of the Mach number and the angle of incidence. Also the differences between the flow behavior over a standard (NACA0012) and a supercritical (OAT15A) airfoils are studied. Furthermore, attention is paid to the effect of the presence of a laser probe downstream from the test section, which may be a source of noise that can affect the behavior of the shock motion.

7.1 Mach number influence

The Mach number, together with the angle of incidence and the Reynolds number, are the aerodynamic parameters that influences most the onset and development of buffet. This influence has been studied in both aerodynamic models by setting a constant value of the angle of attack and varying the Mach number from 0.65 to 0.80. Two particular cases are presented here, the first one for the NACA0012 model at $\alpha = 4°$ with free transition and the presence of the laser probe inserted 17 cm inside the wind tunnel, see Fig. 7.1. The acquisition frequency used was 1500 Hz for a total duration of 1 second. The second case for the OAT15A model at $\alpha = 3.5°$ with fixed transition at $x/c = 7\%$ using Carborundum 500 and without the presence of the laser probe, see Fig. 7.2. A frame rate of 4000 Hz was used during 1 second in this case. The reason to choose these two cases is that they were

tested for both experimental techniques, Schlieren and PIV. However, in this section only the results computed from the Schlieren measurements are shown.

A priori, it is expected that an increase in the Mach number from a steady regime will trigger buffet. Further increase will lead the airfoil to its most unsteady regime, where buffet is fully developed and, eventually, the phenomenon will be damped and disappear as the Mach number overcomes the upper bound of the buffet regime. It can also be expected to observe a variation of the buffet frequency for varying Mach number, as stated by Jacquin et al. (2009). The aim of this analysis is to know where the buffet regime appears and how it develops in terms of increasing Mach number.

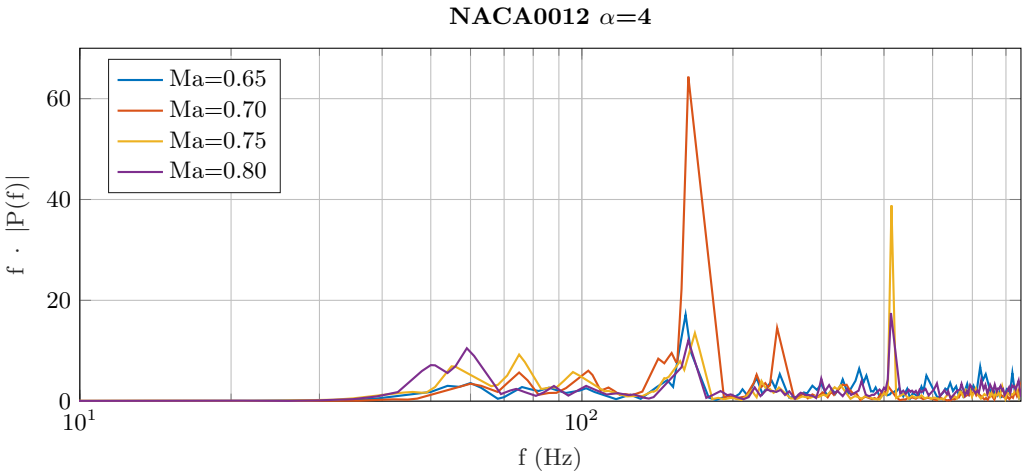

Figure 7.1: Influence of Mach number on the shock motion spectrum for the NACA0012 at $\alpha = 4°$. Schlieren results.

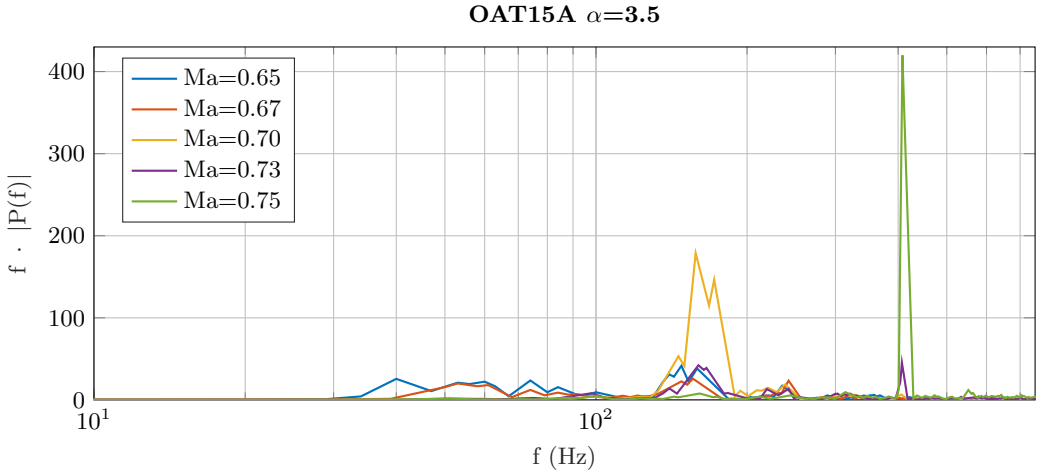

Figure 7.2: Influence of Mach number on the shock motion spectrum for the OAT15A at $\alpha = 3.5°$. Schlieren results.

Two main peaks are observed in the frequency spectrum from Figs. 7.1 and 7.2. The first

one at $f \sim 160$ Hz and the second one at $f \sim 405$ Hz. The former corresponds to the buffet peak, whereas the later is actually associated to the wind tunnel noise, as it was shown in Chapter 6. Focusing on this last peak, note the dramatic increase of energy it suffers for increasing Mach number, reaching values of $f \cdot |P(f)|$ more than twice the buffet peak for the OAT15A airfoil at $Ma = 0.75$. The tunnel noise gains strength for increasing free stream Mach number. It was shown in Chapter 6 that the magnitude of this peak is highest at free stream Mach values near 0.80. The Mach numbers measured now are relatively lower, but it has to be taken into account that they are not corrected. If the corrections are applied, the actual values are slightly higher. The solely presence of this peak in the frequency spectrum of the shock motion means that the wind tunnel noise interacts with the shock wave and affects its development.

From the literature it is known that buffet develops in a specific range of aerodynamic conditions and that out of this interval, the phenomenon gets damped or just disappears. This is corroborated by Figs. 7.1 and 7.2, where it is observed that at frequencies near 160 Hz a large peak appears only for Mach numbers in the vicinity of $Ma \approx 0.7$. This means that there are an upper and a lower bounds for the phenomenon, however the sampling of Mach numbers used in this study is not fine enough to capture the exact onset of buffet. Note that in both airfoils buffet develops in a similar range of Ma, near 0.7.

	NACA0012 $\alpha = 0°$				OAT15A $\alpha = 0°$			
Ma	f	$f \cdot \|P(f)\|$	$(\bar{x}/c)_s$	$(x/c)_{rms}$	f	$f \cdot \|P(f)\|$	$(\bar{x}/c)_s$	$(x/c)_{rms}$
0.75	166	18.82	0.40	5.98%	162	45.77	0.66	7.78%
0.77	165	27.89	0.46	4.63%	-	-	-	-
0.80	166	8.83	0.71	2.47%	165	17.15	0.75	3.98%
	NACA0012 $\alpha = 2°$				OAT15A $\alpha = 2°$			
Ma	f	$f \cdot \|P(f)\|$	$(\bar{x}/c)_s$	$(x/c)_{rms}$	f	$f \cdot \|P(f)\|$	$(\bar{x}/c)_s$	$(x/c)_{rms}$
0.70	164	19.76	0.37	3.39%	162	35.55	0.49	4.97%
0.73	168	14.02	0.49	3%	158	53.00	0.61	4.32%
0.75	161	21.9	0.61	2.95%	163	25.68	0.66	3.69%
0.77	166	8.87	0.68	2.60%	164	14.22	0.73	2.97%
0.80	162	5.27	0.79	2.64%	-	-	-	-
	NACA0012 $\alpha = 4°$				OAT15A $\alpha = 3.5°$			
Ma	f	$f \cdot \|P(f)\|$	$(\bar{x}/c)_s$	$(x/c)_{rms}$	f	$f \cdot \|P(f)\|$	$(\bar{x}/c)_s$	$(x/c)_{rms}$
0.65	161	17.16	0.30	2.9%	148	41.61	0.33	5.3%
0.67	-	-	-	-	156	25.88	0.46	4.5%
0.70	163	64.37	0.51	3.2%	158	178.66	0.52	6.1%
0.73	-	-	-	-	160	42.18	0.58	3.9%
0.75	168	13.51	0.69	2.8%	161	7.82	0.62	4.3%
0.80	163	12.06	0.94	2.5%	-	-	-	-

Table 7.1: Buffet peak properties, mean shock position and shock displacement from Schlieren results. Cases not tested signaled by a hyphen (-)

Table 7.1 shows the values of frequency (f) and energy ($f \cdot |P(f)|$) for the buffet peaks in every Mach number case, the mean chord wise shock position $(\bar{x}/c)_s$ and the standard

deviation of the shock position $(x/c)_{rms}$ in its cyclic movement. Regarding the frequency value of the peak, a variation is observed for increasing Mach number, however the accuracy of the Schlieren technique for the computation of this parameter is not enough to draw a conclusion from these results. On the other hand, a clearer behavior is observed for the amplitude of the buffet peaks. Focusing on NACA0012 at $\alpha = 4°$ and OAT15A at $\alpha = 3.5°$, the highest values appear at $Ma = 0.7$ with a difference of about $\sim 80\%$ in amplitude with respect to the rest of Mach numbers by means of a rough comparison. It is worth to highlight the large difference in energy of the phenomenon observed between the two airfoils, where the value for the OAT15A is almost 3 times larger than the one for the NACA0012 when comparing the maximum buffet peak, i.e. $Ma = 0.70$ and highest α.

Increasing Mach numbers push the mean shock position to more downstream locations independently of the buffet phenomenon, however, a clear effect is observed over the length of the shock motion, $\Delta(x/c)_s$. Increasing amplitude of buffet peaks is physically translated into an increase of the shock movement length, as shown in Table 7.1 where the highest displacement occurs for $Ma = 0.7$. Note that even for the cases where buffet is not fully developed there is still a shock position fluctuation, meaning that the flow field is not steady.

7.2 Angle of attack influence

The influence of varying angles of attack on buffet is analyzed over the same experimental cases used in the previous section, 7.1. The first one for the NACA0012 model at $\alpha = 0°, 2°, 4°$ with free transition and the presence of the laser probe inserted 17 cm inside the wind tunnel. The second case for the OAT15A model at $\alpha = 0°, 2°, 3.5°$ with fixed transition at $x/c = 7\%$ using Carborundum 500 and without the presence of the laser probe. In this section only the results computed from the Schlieren measurements are shown.

When compared to the Mach number, a similar influence is expected from the angle of attack variation. Buffet is foreseen to occur in a certain range of angles, furthermore, smaller values than the onset limit would avoid the phenomenon to occur. This translates into the existence of a critical value of the angle of attack under which, for a certain experimental setup, buffet will not be triggered. It was demonstrated by McDevitt and Okuno (1985) and Crouch et al. (2009) that both the critical Mach number and angle of incidence depend on each other in the onset of buffet, i.e. they vary as shown in Figs. 2.6 and 2.7. These predictions are corroborated by the results obtained from these experiments, where the expected behavior is found to agree with the results.

Fig. 7.3 shows the energy variation of the buffet peak from the frequency spectrum as function of the Mach number and the angle of attack. It is observed that for every α line there is a Mach number that defines a maximum of buffet energy, corresponding to the values where buffet is more highly developed. These values of Mach numbers decrease for increasing angle of attack, i.e. fully developed buffet is reached at smaller free stream velocities for higher angles of attack. Note that the most fully developed buffet case for

the NACA0012 is actually of the order of the least developed buffet cases for the OAT15A in terms of energy. This actually may suggest that the buffet phenomenon is only fully developed for the OAT15A at $Ma = 0.70$ and $\alpha = 3.5°$, and not for the NACA0012.

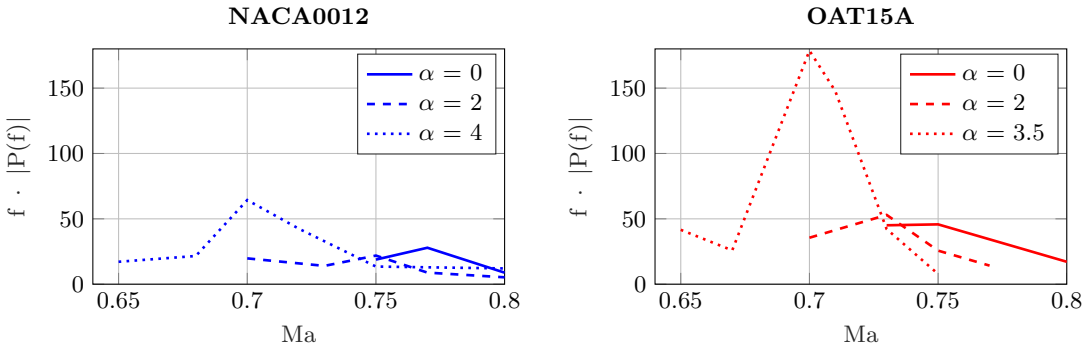

Figure 7.3: Effect of α and Ma over the buffet peak energy, obtained from Schlieren results

7.3 Laser probe effect over buffet

Once the effect of the laser probe over the test section region is studied, one can focus on the effect that it produces over the flow about the aerodynamic models. This analysis aims to study the variations of the buffet phenomenon behavior due to the presence of the probe with different insertion lengths. For that, measurements were performed over both airfoils by means of Schlieren visualization. In both cases the Mach number was set to 0.7 and transition was triggered by means of a Carborundum 500 strip at $x/c = 7\%$. The acquisition frequency was 4000 Hz, the spatial resolution and the recording settings in general were the same for both airfoils so that a direct comparison could be carried out. The only difference between the two cases is the angle of attack, $\alpha = 4°$ for the NACA0012 and $\alpha = 3.5°$ for the OAT15A. The measurements were done for three different configurations, the first one (labeled 0%) without the probe, the second (labeled 10%) with a probe insertion length of 4 cm, and the last one (labeled 50%) with a total insertion of 17 cm.

Based on the results from the empty test section analysis, one can assume that the presence of the probe will have an influence over the buffet development, however, it is difficult to predict *a priori* the real impact. Figs. 7.4 and 7.5 show the results from the Fourier transform analysis of the shock motion in the frequency spectrum for both airfoils.

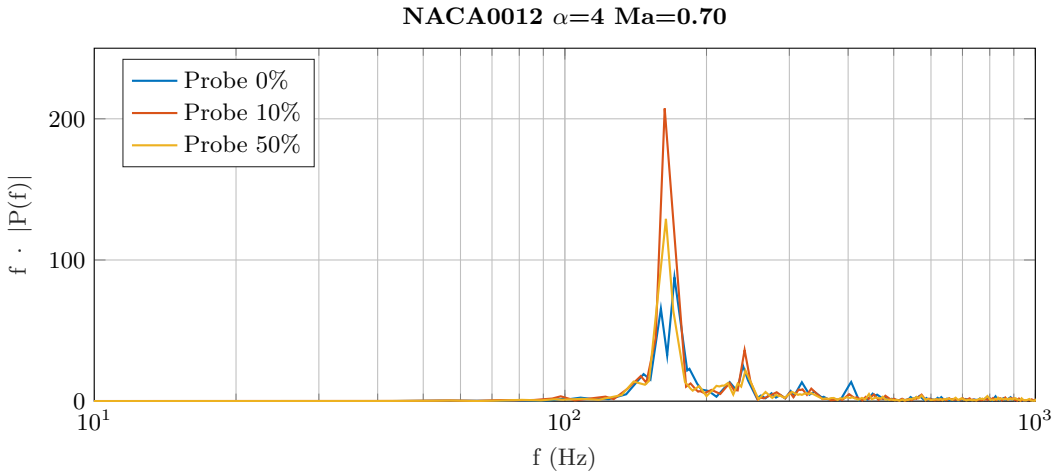

Figure 7.4: Effect of the laser probe on the shock motion spectrum of the NACA0012

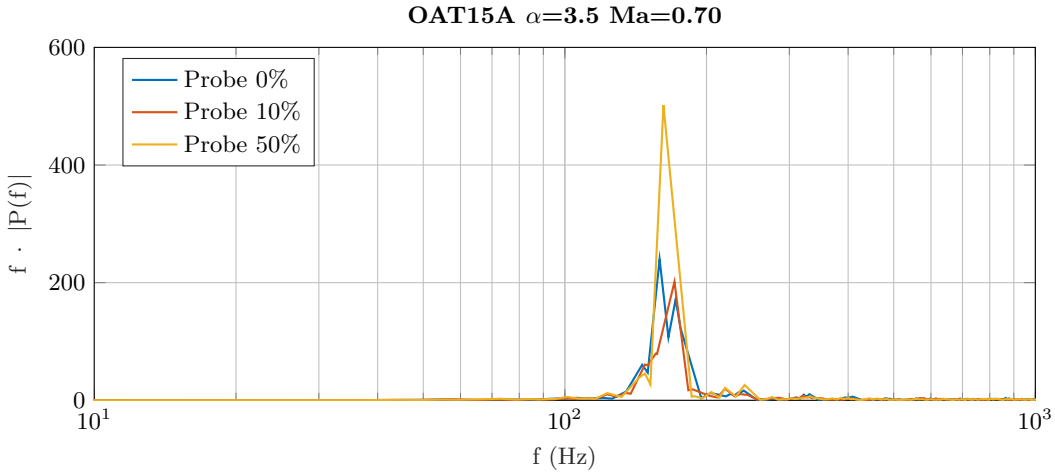

Figure 7.5: Effect of the laser probe on the shock motion spectrum of the OAT15A

Two important conclusions can be highlighted from the results of this analysis. The first one is that the probe has no apparent effect over the buffet frequency. It is observed from the figures that under the three different probe configurations, the buffet peak always falls into the same range of frequencies. It is true that the points of highest magnitude for the three cases have a variation of its local frequency, however this is due to the shape variation of the peak and such point always remains enclosed in the same range of frequencies. The second conclusion is that the presence of the probe actually has an effect over the buffet peak magnitude, i.e. the energy associated to the physical phenomenon. However, there is a remarkable feature of the trend of this influence: the effect of the probe seems to affect differently each airfoil even though they were tested under the same conditions (except for the different angle of attack).

In the NACA0012 case the three configurations in order of decreasing magnitude of

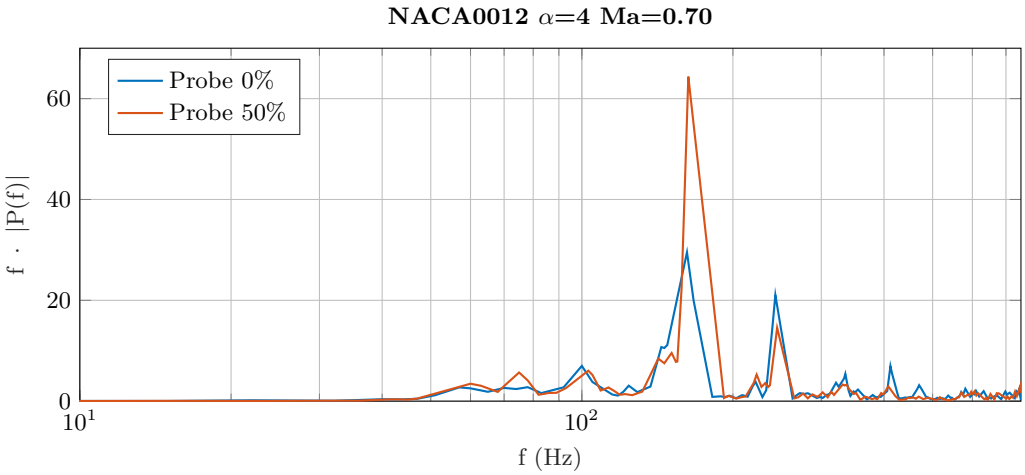

Figure 7.6: Effect of the laser probe on the shock motion spectrum of the NACA0012

buffet peak are 10%, 50% and 0%, whereas in the OAT15A case they are 50%, 0% and 10%. In other words, the buffet phenomenon appears to be more powerful under the influence of the laser probe than when the probe is not in the tunnel, nevertheless there is a difference between the airfoils concerning the insertion length of the probe. In the NACA0012 case the magnitude is higher for the 10% configuration, while for the OAT15A it is higher for the 50% configuration instead. From these results, it is not possible to state the physical reason behind this difference between the airfoils. Note that this analysis was only done under this particular aerodynamic conditions, and that if they changed, the described trend could be different. Also it is worth to highlight that the reproducibility of the later conclusion is not ensured as the experiment was done only once.

On the other hand, the reproducibility of the analysis comparing only the 0% and 50% configurations was proven with two more experiments for the NACA0012 model. Both with free transition, and acquisition frequencies of 1500 Hz. The first one (Fig. 7.6) at $\alpha = 4°$ and Ma=0.70; and the second one (Fig. 7.7) at $\alpha = 0°$ and Ma=0.78.

The results from both cases are very representative and they evidence the conclusions drawn previously. On one hand, Fig. 7.7 shows a case were buffet is not triggered but the noise from the wind tunnel is affecting the shock motion as can be observed from the relatively large peak at 400 Hz. The insertion of the probe in this case has a clear effect: it reduces the magnitude of such peak, as proven by the shock motion. On the other hand, Fig. 7.6 shows a case where the peak at 400 Hz from the wind tunnel is very weak due to the low Mach number but where buffet is fully developed. In this case the insertion of the laser probe entails an increase of the buffet energy while it slightly reduces the rest of the peaks. It can be stated then, that in general the effect the probe has over the flow is to dampen the coherent waves of the wind tunnel noise near 400 Hz and to increase the energy of buffet. It could be that actually these effects are linked to each other, i.e. that the dampen of the peak at 400 Hz is actually the cause for the increase of the buffet phenomenon energy. A possible explanation could be that part of the energy of the shock motion is being absorbed by the motion induced by the 400 Hz waves. However, this conclusion cannot be corroborated with

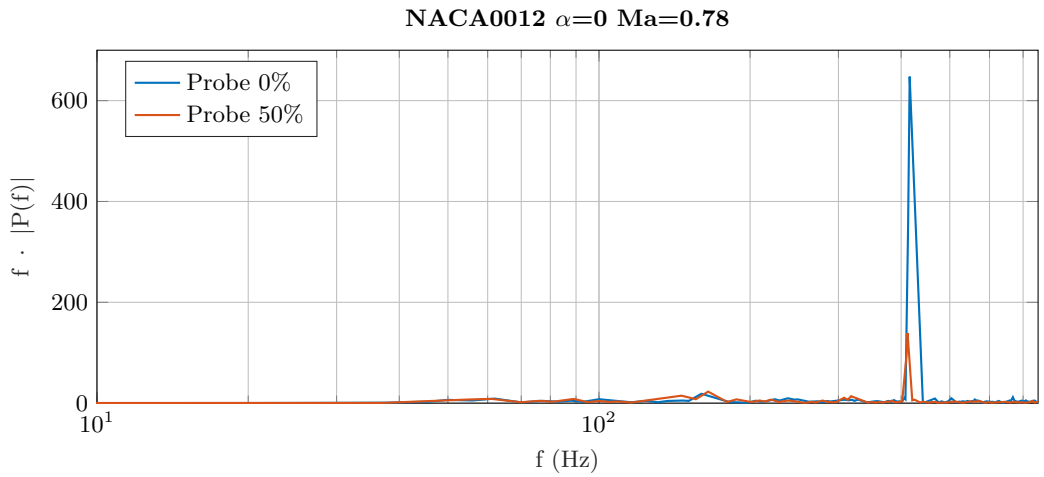

Figure 7.7: Effect of the laser probe on the shock motion spectrum of the NACA0012

the available results.

7.4 Schlieren-PIV frequency analyses comparison

So far, all the results presented for the spectral analysis of buffet in this chapter were obtained from Schlieren results, where the shock position is obtained at every instant and analyzed over time. However, there is an important physical feature that is inherent to the Schlieren system and that can have an effect over the shock position acquisition method, it is the 3D effect, i.e. the overlap of the spanwise flow information in the same plane (e.g. the same Schlieren image). The shock position acquisition method used for the Schlieren results basically consists of looking for the highest light intensity gradient position over a line parallel to the chord. For every time instant a shock position is found, however, it is not guaranteed that such position keeps a fixed spanwise position over time, since all the spanwise information is overlapped in the same plane. This effect entails an uncertainty on the results of the frequency analysis that cannot be accounted for only with the Schlieren results.

This is the reason why the same analysis is performed over a few representative cases where the measurements were obtained by means of PIV, technique that lacks of the detrimental 3D effect mentioned. The aim is to compare the frequency analysis of the results from both experimental techniques and to analyze their possible differences and whether the 3D effect of the Schlieren visualization has significant consequences or it can be neglected.

Four representative experimental cases have been chosen for the comparison, two for each of the airfoils. On one side, for the NACA0012 model the tests for both the Schlieren and PIV techniques were done under the exact same flow conditions and wind tunnel setup, with the laser probe introduced in the 50% configuration. The flow conditions used are $\alpha = 2°$, $Ma = 0.75$ for the first case and $\alpha = 4°$, $Ma = 0.70$ for the second one. The acquisition frequency used for Schlieren was 1500 Hz with a spatial resolution of $\sim$10 pix/mm, whereas for PIV 8000 Hz acquisition frequency was used with a total spatial resolution of $\sim$19 pix/mm. On the other hand, for the OAT15A model there is a difference between the tests, for the Schlieren cases the laser probe was not inserted, whereas in the PIV cases it was inserted in the 10% configuration. The test cases were $\alpha = 2°$, $Ma = 0.73$ and $\alpha = 3.5°$, $Ma = 0.70$. The acquisition frequencies and spatial resolutions were 4000 Hz, $\sim$5 pix/mm respectively for the Schlieren measurements and 8000 Hz, $\sim$19 pix/mm for the PIV measurements.

Figs. 7.8 and 7.9 show the comparison between the analysis from Schlieren and PIV results. Note that this analysis is done over the development of the shock position in time, which means that the temporal and spatial discretization will have an effect over the computed energy of the phenomenon, i.e. over the area enclosed under the curves of the frequency analysis. This means that, due to the differences in acquisition frequencies and spatial resolutions between the test cases, this area may be different. Hence, a direct comparison of the amplitude of the curves between the Schlieren and PIV tests may have an uncertainty due to this effect. Despite it, it is observed in the figures that the frequency analyses from both techniques agree quite well, especially for the OAT15A airfoil. The peaks are located in the same frequency ranges or with small deviations of maximum 5-10 Hz. The magnitudes of the curves are consistent and of the same order. A difference can be

noted in the NACA0012 at $\alpha = 4°$, $Ma = 0.70$, where the Schlieren system detects a much stronger buffet peak than the PIV system, but at the same frequency. A strong peak would be expected there as at those conditions buffet is triggered, however, taking into account that the rest of the cases are in good agreement, this difference may just be due to the reproducibility of the experiment, i.e. that the particular conditions of this test run led to this difference.

It can then be concluded from these results that the buffet phenomenon is mostly two-dimensional and that the 3D effect captured by the Schlieren system does not influence strongly the shock movement frequency analysis. Schlieren visualization can be used for a preliminary study of the buffet presence and behavior.

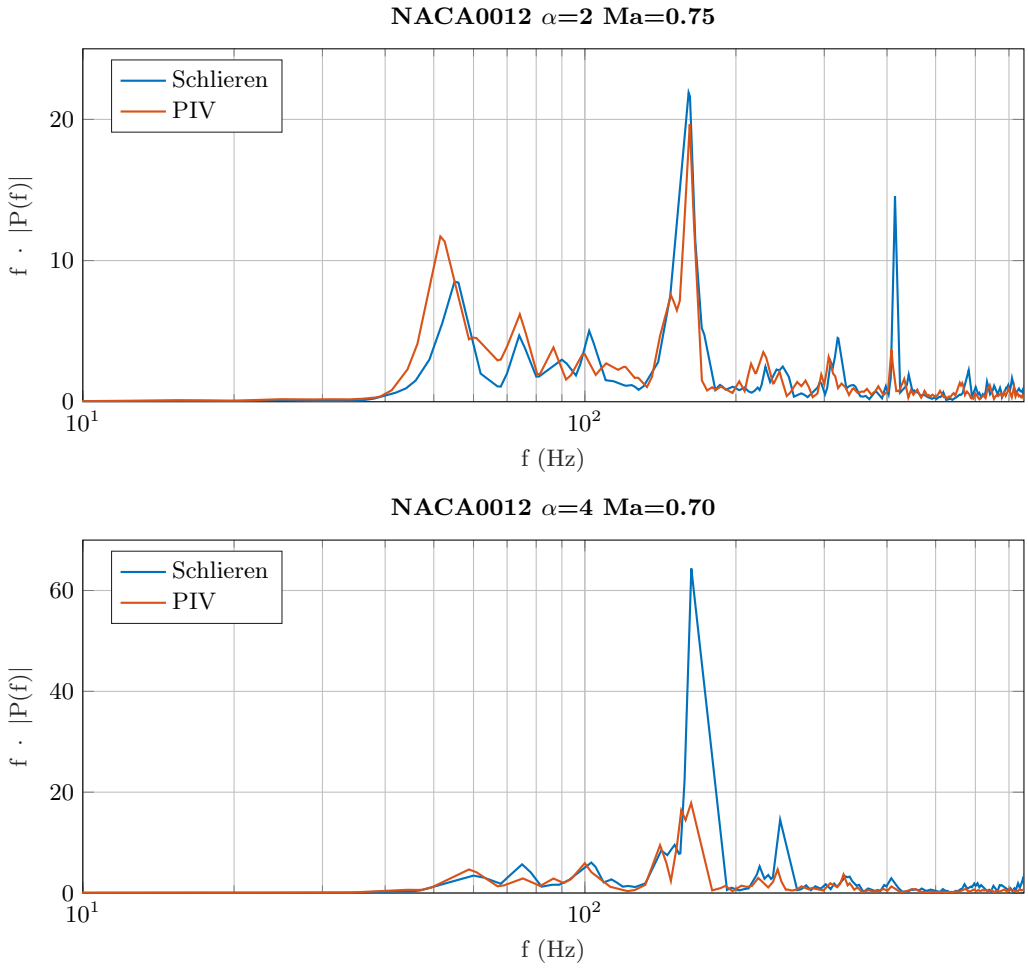

Figure 7.8: Schlieren-PIV frequency analysis comparison over NACA0012

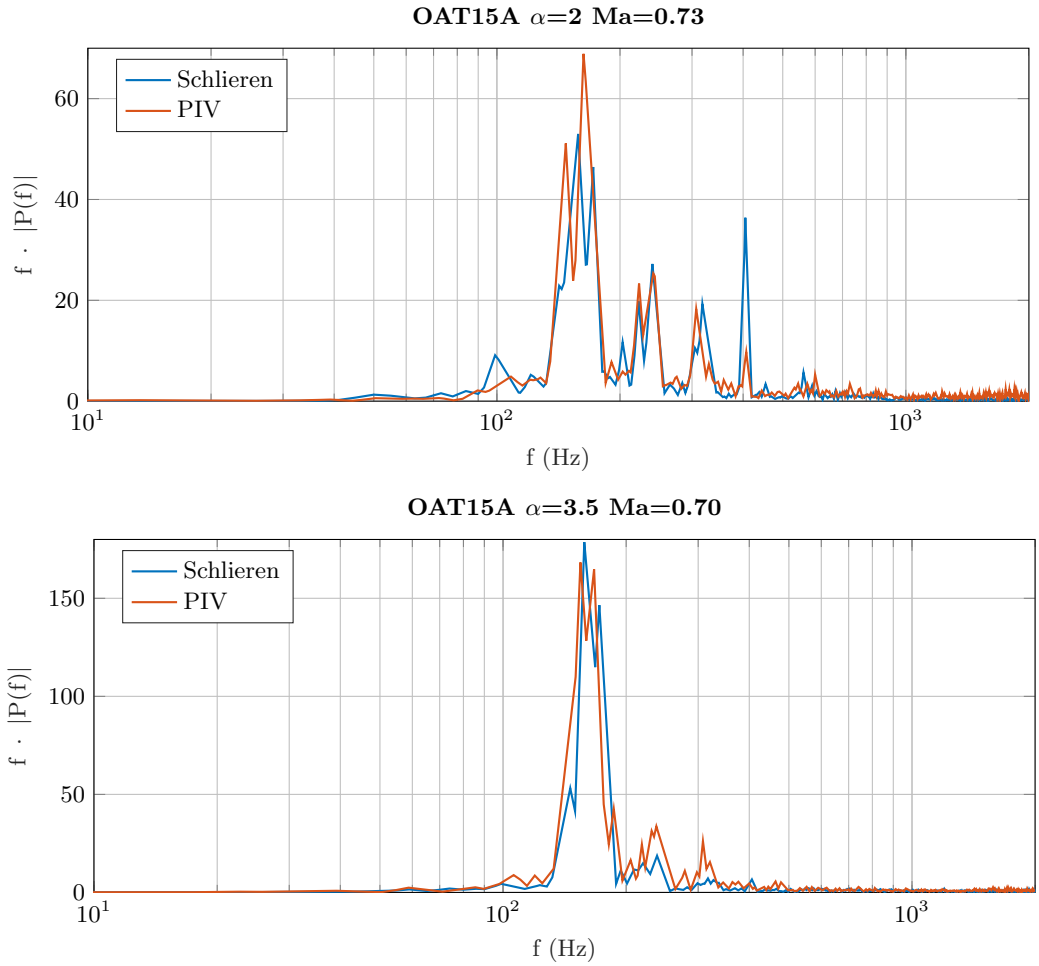

Figure 7.9: Schlieren-PIV frequency analysis comparison over OAT15A

	NACA0012 $\alpha = 0°$				OAT15A $\alpha = 0°$			
Ma	f	$f \cdot \lvert P(f)\rvert$	$(\bar{x}/c)_s$	$(x/c)_{rms}$	f	$f \cdot \lvert P(f)\rvert$	$(\bar{x}/c)_s$	$(x/c)_{rms}$
0.78	144	23.65	0.55	3.58%	163	11.68	0.68	3.01%
	NACA0012 $\alpha = 2°$				OAT15A $\alpha = 2°$			
Ma	f	$f \cdot \lvert P(f)\rvert$	$(\bar{x}/c)_s$	$(x/c)_{rms}$	f	$f \cdot \lvert P(f)\rvert$	$(\bar{x}/c)_s$	$(x/c)_{rms}$
0.70	-	-	-	-	160	49.07	0.48	5.30%
0.73	-	-	-	-	163	68.89	0.55	4.60%
0.75	162	19.66	0.63	3.00%	-	-	-	-
	NACA0012 $\alpha = 4°$				OAT15A $\alpha = 3.5°$			
Ma	f	$f \cdot \lvert P(f)\rvert$	$(\bar{x}/c)_s$	$(x/c)_{rms}$	f	$f \cdot \lvert P(f)\rvert$	$(\bar{x}/c)_s$	$(x/c)_{rms}$
0.70	163	17.84	0.52	2.64%	155	161.64	0.48	7.01%
0.73	-	-	-	-	162	29.55	0.48	3.85%
0.75	163	8.66	0.71	4.07%	-	-	-	-

Table 7.2: Buffet peak properties, mean shock position and shock displacement from PIV results. Cases not tested signaled by a hyphen (-)

7.5 Conclusions

The analysis of the influence of Mach number and angle of attack variations over the evolution of buffet has shown that actually there is only one case per airfoil in which buffet is more highly developed, labeled as *buffet cases*. In the case of the OAT15A with fixed transition at $x/c = 7\%$, the buffet case is at $Ma = 0.70$ and $\alpha = 3.5°$. For this case, buffet is fully developed. In the case of the NACA0012 with free transition, the Buffet case is at $Ma = 0.70$ and $\alpha = 4°$, but it has been found that Buffet may not be fully developed when comparing the energy of the phenomenon to the first case. These cases are used for the rest of the analyses as they are the ones were buffet is best represented. Table 7.3 gathers the characteristics of these two cases.

	NACA0012 $\alpha = 4°$					OAT15A $\alpha = 3.5°$				
Ma	f	ω^*	$f \cdot \lvert P(f) \rvert$	$(\bar{x}/c)_s$	$(x/c)_{rms}$	f	ω^*	$f \cdot \lvert P(f) \rvert$	$(\bar{x}/c)_s$	$(x/c)_{rms}$
0.70	163	0.44	64.37	0.51	3.2%	158	0.43	178.66	0.52	6.1%

Table 7.3: Buffet peak properties, mean shock position and shock displacement of the *Buffet cases* from Schlieren visualization

It can also be concluded that the laser probe effect over the shock motion reduces the noise from the wind tunnel, specially the peak found at ~ 400 Hz, hence increasing the energy of the buffet phenomenon. Moreover, the results of the spectral analysis from both the Schlieren and the PIV measurements were found to be in good agreement.

Chapter 8

Wave propagation analysis

It is known by now that the vortices traveling downstream inside the separated region and the pressure fluctuations that emanate from the trailing edge and that travel upstream as the so called *upstream traveling waves* are linked with each other and with the whole buffet cyclic mechanism. However, the exact dynamic relation between them, their cause and effect and the role they play on the feedback loop is not yet fully clear. In Chapter 5 a general overview and introduction to the flow field was given. This chapter focuses on the study of the upstream traveling disturbances and the downstream traveling vortices generated in the separated region. The main goals are to actually capture the existence and properties of these waves from the PIV measurements using a correlation analysis over the velocity fields in time in order to compute their velocity and characteristic frequency. Furthermore, it is also desired to analyze the relation and synchronization mechanism of the vortices with these pressure fluctuations. This is done for two cases, the OAT15A airfoil at $Ma = 0.70$ and $\alpha = 3.5°$ with fixed transition at $x/c = 7\%$, and the NACA0012 at $Ma = 0.70$ and $\alpha = 4°$ with free transition. These two cases were found to be the ones were buffet was most highly developed.

As it was presented in Chapter 5, there is a huge difference in the size of the separated region during the different phases of one buffet cycle. It was stated by Hartmann et al. (2013) that the larger the separation region size is, the less noise is generated at the trailing edge. The reason is that the vorticity (the driving mechanism of noise) is lower as it is determined by the local velocity gradient, and large separated regions undergo a smaller vertical velocity gradient than smaller separated regions, see Hartmann et al. (2013). Furthermore, the presence of such large separated region force the upstream traveling waves to undergo stronger refraction and interaction with a shear layer, which decreases its sound pressure level during the upstream movement. On the other hand, a different factor that influences the strength of the pressure waves is the strength of the vortex that creates them. Stronger vortices lead to higher sound pressure levels, hence stronger upstream traveling waves. Following Hartmann et al. (2013) idea then, there are 2 factors that would make the UTW to be stronger, i.e the presence of strong vortices at

the trailing edge and a small separated region. Firstly, these strong vortices are created during the upstream movement of the shock, but they arrive to the trailing edge with a certain delay. Secondly, the small separated region is present during the downstream shock movement. In Hartmann et al. (2013), both these factors occur at the same time due to the delays they measured in these two phenomena (vortices and UTW). Nevertheless, this is just hypothesized by Hartmann et al. (2013), and not real proof is given corroborating that this strength modulation of the UTW is actually happening in the flow. This reasoning suggests at least that it is important to study how these 2 phenomena, e.g. vortices and UTW, actually interact with each other during the buffet cycle in order to analyze whether there is a delay associated to them and to check if the pressure waves are actually significantly stronger during a specific part of the cycle. In order to do that, it is also necessary to analyze how the vortices are being shed and to study their velocity and frequency.

This analysis is necessary in order to be able to demonstrate the feedback loop mechanism of the buffet phenomenon and the role and effect that such disturbances play in the oscillatory motion, even when the characteristic frequencies of these phenomena differ by one order of magnitude. This synchronization mechanism is currently the state of the art topic in the study and understanding of buffet. The first section of this chapter presents the results obtained from the velocity fields correlation analysis and a thorough description of the phenomena observed, then an analysis is done of the dynamics of the vortices shed at the separated wake region and finally some important conclusions about this chapter are gathered and put together for clarification purposes.

8.1 Upstream traveling waves

In order to understand the link between upstream traveling waves with the rest of the cycle and, hence, to be able to make a close argumentation of the buffet self sustained oscillation, it is needed to have an explanation of the physical mechanisms that create such waves and their characteristic frequencies and development over the flow field. An analysis of the UTW is discussed here, to show how they develop in time and to try to analyze its behavior and importance with respect to the cyclic phenomenon.

The model presented by Lee (2001) was the first introducing the idea of the UTW, he stated that disturbances were generated at the shock foot that traveled to the trailing edge, generating there the UTW that would travel upstream and influence the shock wave. It is known that these waves are created when vortices reach the trailing edge of the airfoil, as the wall bounded shear layer changes instantaneously into a free shear layer. This is the reason why the UTW strength and frequency actually depend on the vortices and on the separation region size, or what is equivalent, on the shock wave position as it defines the actual separation size. This leads to the fact that during the whole buffet cycle, the pressure waves change strength is being modulated, changing also their effect over the shock wave motion. This change produced by the shock wave on the UTW occurs at the same frequency as the shock moves. This means that even if the UTW are generated at a different frequency, their effect over the shock wave changes with a frequency equal to the buffet frequency.

Fig. 8.1 shows the instantaneous velocity field during the downstream motion of the shock wave at 6 consecutive time instants where the development of an upstream traveling wave can be observed. This wave appears as a perturbation in the velocity field that travels upstream until it reaches the shock wave. This actually proves that these pressure waves can be captured by means of PIV, and that a proper correlation analysis over the velocity fields can be performed to study their development and characteristics. Note that the pressure wave is marked in the images with a black straight line for better visualization.

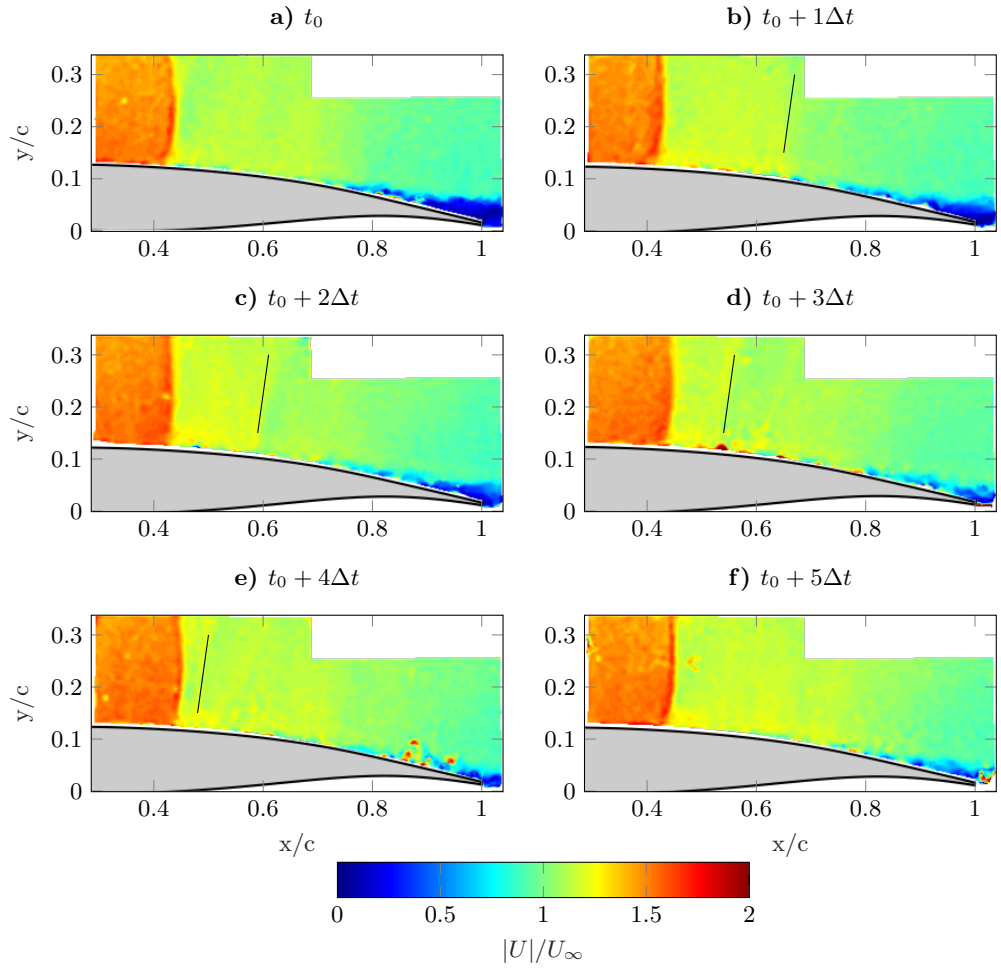

Figure 8.1: Upstream traveling wave in instantaneous velocity field $|U|$ at buffet flow over OAT15A at $\alpha = 3.5$ and $Ma = 0.70$, $\Delta t = 0.125$ ms.

8.1.1 Determination of UTW velocity

The correlation analysis is firstly performed for the case of the OAT15A airfoil at $\alpha = 3.5°$ and $Ma = 0.70$ with fixed transition at $x/c = 7\%$. This is the case where buffet was found to be most fully developed, with shock motion of standard deviation equal to $(x/c)_{rms} = 7.03\%$,

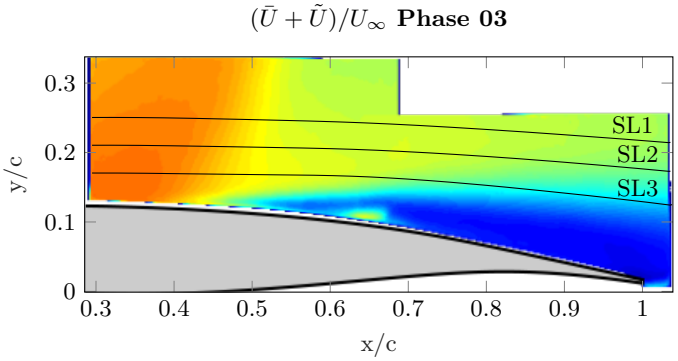

Figure 8.2: Streamlines used for the correlation analysis over the phase averaged flow field.

so the results for the upstream traveling waves are expected to be better visualized. Fig. 8.2 is a re-plot of Fig. 4.14 that shows the streamlines used for the correlation analysis. The correlation function used and described also in Chapter 4 is

$$R(x_{ref}, x_1, \tau) = \int_{-\infty}^{\infty} \frac{U'(x_{ref}, t) \cdot U'(x_1, t+\tau)}{\sqrt{U'(x_{ref}, t)^2 \cdot U'(x_1, t+\tau)^2}} dt, \tag{8.1}$$

where the velocity function at x_1 is correlated against x_{ref}. See Chapter 4 for further information about the correlation procedures.

Firstly the correlation is applied over the entire chord length available from the PIV results including the shock wave region. The aim is to analyze what kind of information can be captured from the correlation without the settings that specifically increase the sensitivity for the upstream traveling waves. Fig. 8.3 shows the correlation maps of the described horizontal and vertical velocity fields, respectively. The streamline analyzed is SL1, with x_1 varying from $0.3 \leq (x_1/c) \leq 1$, the reference position placed at $x_{ref}/c = 0.65$, i.e. downstream from the shock position and with a varying time delay of $-0.02 \leq \tau \leq 0.02$ s between the signals. A low-pass filter is used at a cut-off frequency of $f_{cut} = 500$ Hz in order to perfectly capture the phenomena related to the buffet frequency by removing the effect of the high-frequency phenomena.

The shock wave movement is nicely captured by the correlation analysis of the horizontal velocity component u', the region in which it moves, $0.4 \leq x/c \leq 0.6$, can be observed in image a) as a disturbance that highlights against the background. The frequency at which this phenomenon occurs can be estimated by measuring the time delay τ between maximums, which actually is the period of the signal. Such delay is of the order of $\tau \sim 6.3$ ms, which leads to frequencies of $f = 1/\tau \approx 160$ Hz, exactly of the order of the buffet frequency captured in the spectral analysis in Chapter 7. Furthermore, note the presence of a downstream traveling phenomenon, represented as slightly tilted straight disturbances that arise from the shock region ($0.4 \leq x/c \leq 0.6$) and extend towards the trailing edge at exactly the same frequency of buffet. This phenomenon is being captured more clearly in the correlation of the vertical velocity component v', image b), which means that its effect is stronger over this component, i.e. it is a disturbance that mainly creates a variation in the vertical component. The velocity at which it travels downstream cannot be accurately

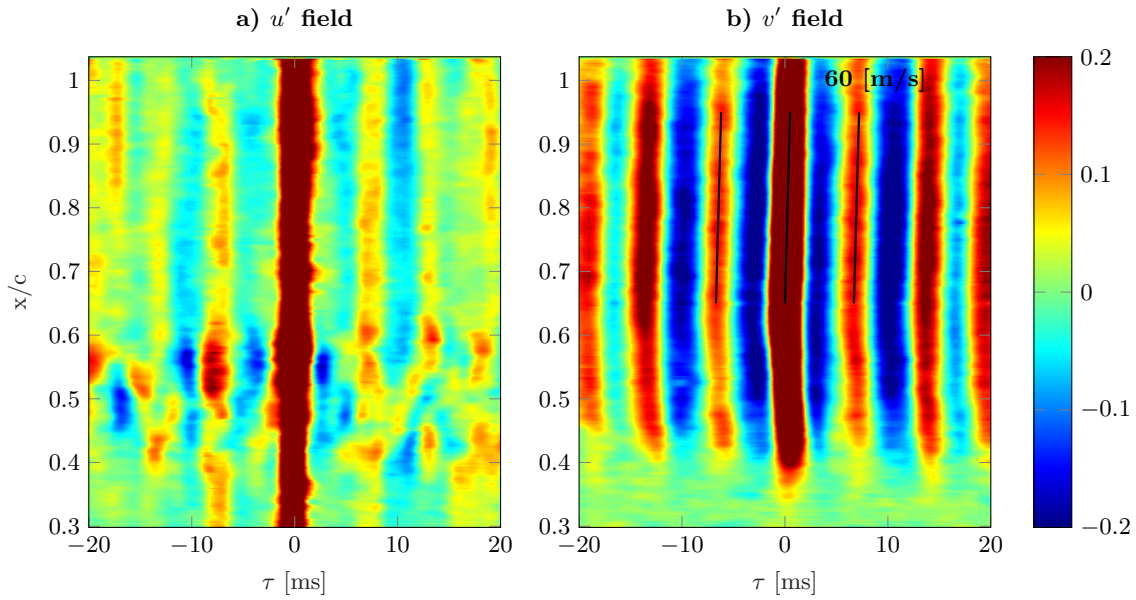

Figure 8.3: Contours of the correlation of a) u' and b) v' velocity components along streamline SL1, with $x_{ref}/c = 0.65$ and low-pass filtered for the OAT15A at $\alpha = 3.5°$ and $Ma = 0.70$.

computed and its uncertainty is graphically estimated, such velocity is found to be of the order of 60 ± 10 m/s, which actually is too low to be associated to the vortices being convected downstream inside the separated region if one takes into account that the outer flow speed is of the order of ~ 230 m/s. Note that this downstream traveling phenomenon starts exactly at the shock foot in image b) and not before, which indeed demonstrates that it is related to the development of the separated region itself.

Now for Fig. 8.4, in order to focus exclusively on the high frequency phenomena taking place on the flow field, a high-pass filter is applied at a cut-off frequency of $f_{cut} = 1200$ Hz. From the literature it is known that the upstream traveling waves are produced at a frequency of $f_{utw} = 1000$ Hz on an airfoil of 200 mm chord, using the Strouhal number it is estimated that for the present study (chord length 100 mm) the UTW are expected to occur at frequencies of the order of $f_{utw} = 2000$ Hz. By applying a high-pass filter at 1200 Hz it is possible to get rid of the strong effects caused by the low frequency phenomena, such as the shock motion and the pulsating character of the separated region. Furthermore, the buffet cycles are divided in two different phases as was explained before, Phase 1 referencing the upstream motion of the shock wave and Phase 2 for the downstream motion. In this case, the x_1 value for the correlation is restricted to $0.6 \leq x_1/c \leq 1$ so that the shock wave region is avoided. The rest of the correlation parameters are kept constant with respect to the previous case, i.e. streamline SL1 and $x_{ref}/c = 0.65$. The absolute fluctuating velocity field ($U' = \sqrt{u'^2 + v'^2}$) is analyzed in Fig. 8.4, as it contains both the horizontal and vertical components of the velocity,

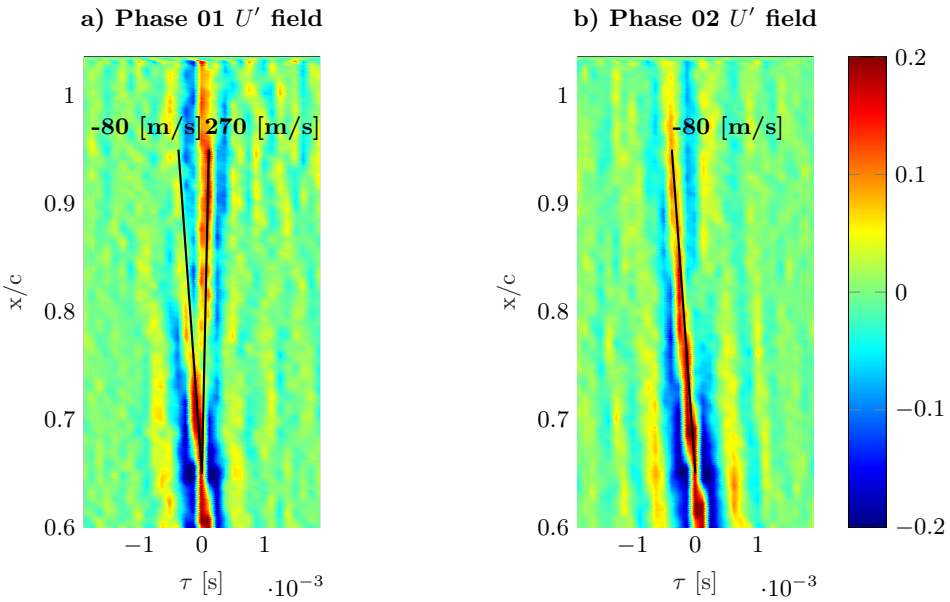

Figure 8.4: Contours of the correlation of U' velocity component in phases along streamline SL1, with $x_{ref}/c = 0.65$ and high-pass filtered for the OAT15A at $\alpha = 3.5°$ and $Ma = 0.70$.

In Fig. 8.4 a clear difference is observed between phases 1 and 2: for the upstream motion of the shock wave (Phase 1) the correlation map is dominated by a downstream traveling signal at a velocity of the order of 270 ± 50 m/s, whereas for the downstream shock wave motion (Phase 2) the correlation map is clearly showing an upstream traveling signal at a velocity of the order of -80 ± 10 m/s. Note that in Phase 1 this upstream traveling signal is also present, however it is weaker, which suggests that either it is masked by the downstream traveling signal or that the presence of the massively separated region is weakening or even canceling the creation of such disturbance. From the phase-average velocity fields, it is known that the flow velocity after the shock and during the shock upstream motion is of the order of $1.2 \cdot U_\infty \approx 270$ m/s, so the result showed for Phase 01 actually suggests that the correlation analysis done over the fluctuating component of the velocity is capturing the presence of disturbances that are convected with the flow speed. Probably these disturbances are related to the seeding and the outliers formed in the velocity fields during the PIV post-processing that are indeed convected downstream at speeds of the order of the flow speed itself. If that is the case, the reason why they appear stronger in Phase 1 is due to the presence of the massively separated region that deflects the flow forcing all these disturbances to pass through the streamline of study SL1. This assumption would mean that this phenomenon is not actually related to the flow itself, but to the measurement technique. The frequency at which the upstream traveling disturbances phenomenon is occurring can be computed from Fig. 8.4. The delay between two maxima has been measured to vary between $\tau \sim 0.25 - 0.5$ ms, see Fig. 8.5 that shows the correlation signal at a fixed position $x/c = 0.70$. This means that the frequency of these upstream traveling waves is in the range of $f_{utw} \approx 2000 - 4000$ Hz, and it is coincident in both phases. This uncertainty related to the delay between maxima of the correlation profile is caused by the *rough* discretization of the time signal due to the acquisition frequency used for the experiments. Higher values of acquisition frequency would

enhance the computation of the actual UTW frequency.

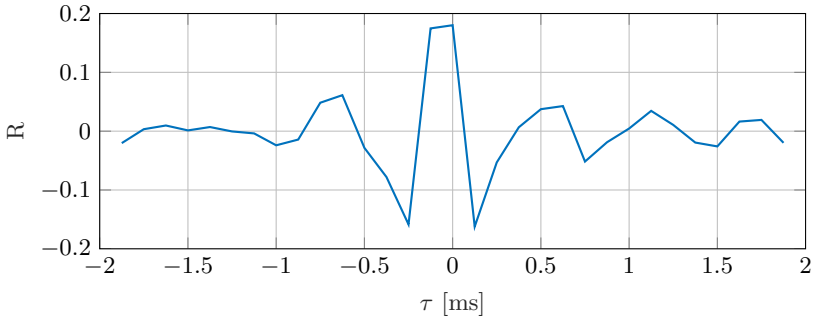

Figure 8.5: Correlation contour of OAT15A at $\alpha = 3.5°$ and $Ma = 0.70$ at $x/c = 0.70$.

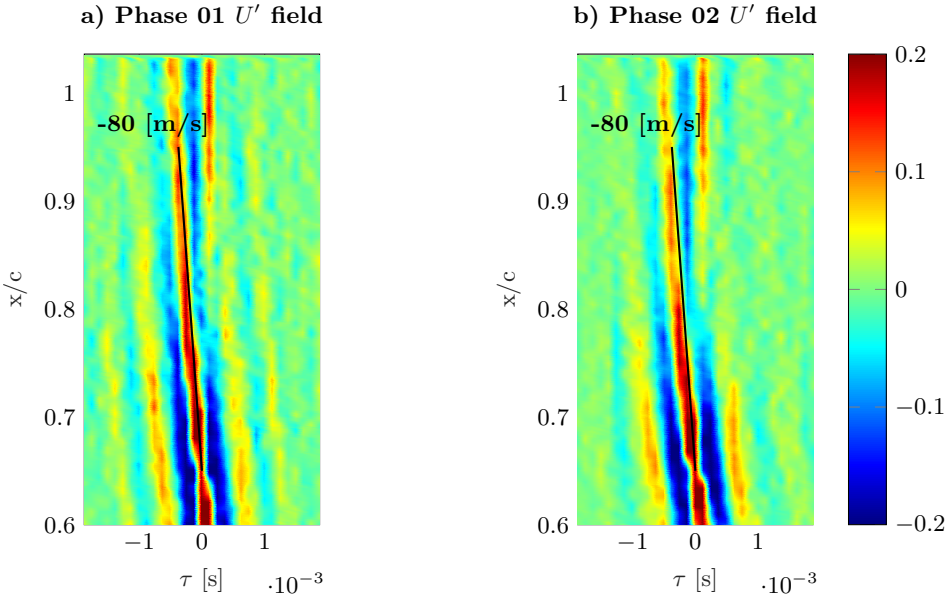

Figure 8.6: Contours of the correlation of U' velocity component in phases along streamline SL1, with $x_{ref}/c = 0.65$ and high-pass filtered for the OAT15A at $\alpha = 2°$ and $Ma = 0.70$.

Fig. 8.6 shows the same analysis done over the case OAT15A at at $\alpha = 2°$ and $Ma = 0.70$, that was seen in Fig. 5.14 to present a highly unsteady periodic flow development marked by a strong shock wave displacement ($(x/c)_{rms} = 5.3\%$) but with the absence of a massively separated region from the shock foot. Instead separation was occurring mostly in the trailing edge region of the suction surface. As can be observed, the upstream traveling signal appears clear in both phases at a velocity of -80 ± 10 m/s, i.e. appears equally during the whole cycle of the shock wave motion. The main difference with respect to Fig. 8.4 is that now the upstream traveling signal is much clearer and the downstream traveling signal at 270 ± 50 m/s is much weaker. Physically, the main difference between both flow fields is the absence of the massively separated region from shock foot during the upstream motion of the shock wave, which indeed indicates that such separated region may be just masking

or even weakening the creation of the disturbances that travel upstream at -80 ± 10 m/s. Again, a frequency of the order of $\sim 2000 - 4000$ Hz is measured from this correlation maps for the upstream traveling disturbances. Note that the velocities of the disturbances are just slightly affected by the variation in the free stream conditions between the different cases being analyzed, and that change cannot be measured in the present correlation maps due to the time discretization.

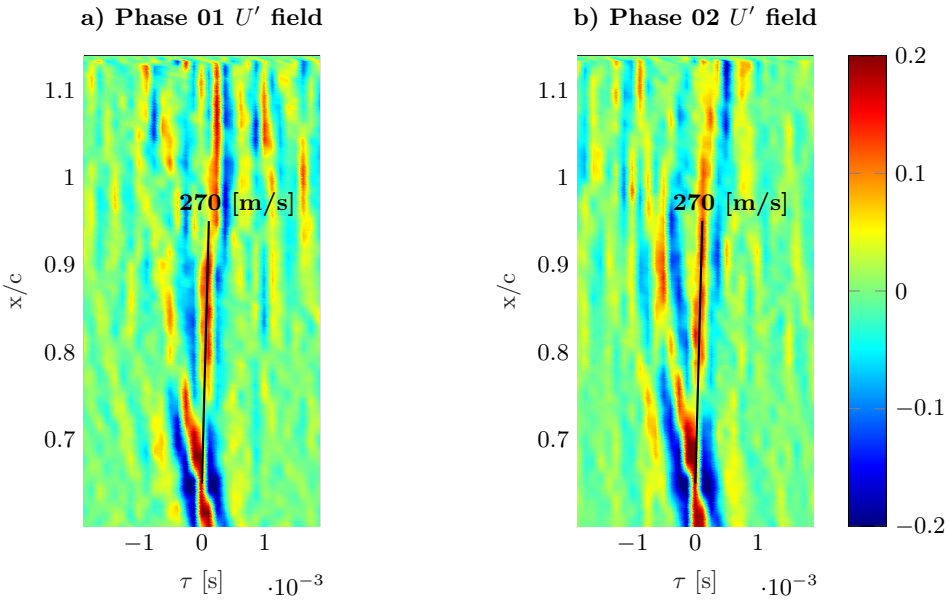

Figure 8.7: Contours of the correlation of U' velocity component in phases along streamline SL1, with $x_{ref}/c = 0.65$ and high-pass filtered for the OAT15A at $\alpha = 3.5°$ and $Ma = 0.73$.

Fig. 8.7 depicts the correlation map for the case of the OAT15A at $\alpha = 3.5°$ and $Ma = 0.73$, a case in which the buffet phenomenon is not fully developed and massive separation is always taking place from the shock foot without reattachment, see Fig. 5.15. The shock motion amplitude has a standard deviation of $(x/c)_{rms} = 3.84\%$. In this case it can be seen that the upstream traveling disturbances at -80 ± 10 m/s are barely present and that the downstream traveling signal at 270 ± 50 is not as defined as in Fig. 8.4. After the analysis of images 8.4, 8.6 and 8.7 it can be stated that the effect of the massive separated region from the shock foot is actually to mask and weaken the upstream traveling waves at -80 ± 10 m/s.

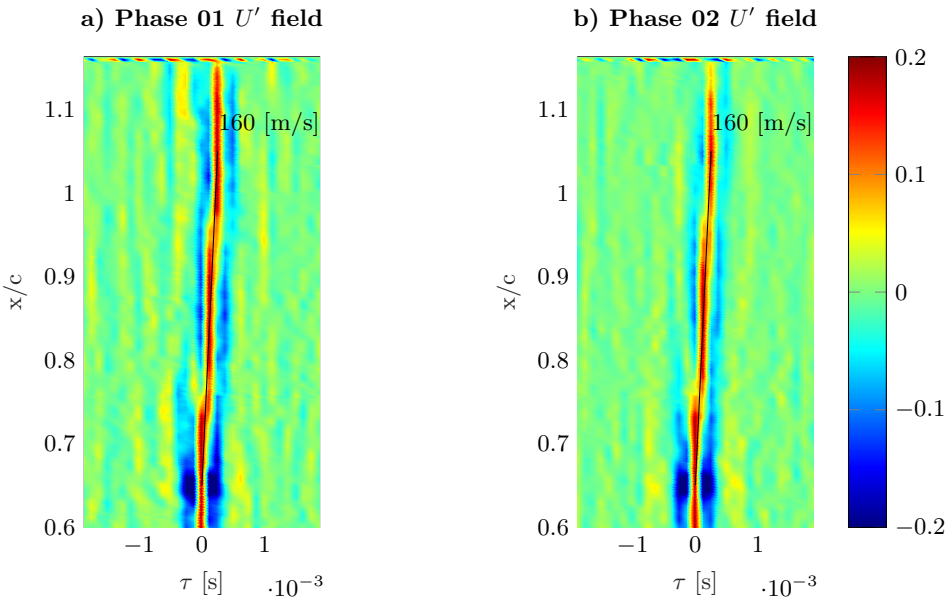

Figure 8.8: Contours of the correlation of U' velocity component in phases along streamline SL1, with $x_{ref}/c = 0.65$ and high-pass filtered for the NACA0012 at $\alpha = 4°$ and $Ma = 0.70$.

The exact same analysis is performed over a different aerodynamic case, the NACA0012 model at $\alpha = 4°$, $Ma = 0.70$ and free transition, conditions under which buffet was found to be most fully developed for this particular airfoil. All the parameters of the analysis described for the previous case (OAT15A model) have been maintained for the correlation of the NACA0012 with the aim of allowing for a direct comparison between the development of the flow field over both airfoils. Fig. 8.8 shows the contours of the correlation maps performed for this aerodynamic case over the absolute fluctuating velocity component ($U' = \sqrt{u'^2 + v'^2}$). It is observed that in both phases the exact same phenomenon is being captured, a downstream traveling disturbance with a velocity of the order of 160 ± 10 m/s. The most reasonable physical explanation for this phenomenon are the shedding vortices, a cross-correlation analysis of the wake is developed in the next section in order to corroborate this hypothesis. Note the absence in the correlation maps of the upstream traveling waves that were found in the OAT15A case. The buffet phenomenon over the NACA0012 model was demonstrated to be much less powerful and developed, and notably less periodic than over the OAT15A model, see Chapter 7. Moreover, the separated region does not develop with a marked pulsating nature as it does over the supercritical airfoil, reattachment does not completely occur and the growth is not as pronounced. This leads to much weaker sound pressure waves that are not being captured by this analysis, or directly to the lack of such waves.

8.1.2 Theoretical estimation of the UTW velocity

Focusing on the signal captured at -80 m/s, it would be interesting to know whether these upstream traveling disturbances are traveling at the local speed of sound with respect to the flow, i.e. at a total speed equal to $(U_{loc} - a_{loc})$ in the upstream direction. The reason is

that if the disturbances are actually pressure waves, they would be expected to travel at such velocity. In order to do that it is necessary to compute the speed of the sound at the flow field region after the shock. Note that there is a somewhat marked flow velocity variation (U_{loc}) in the x direction downstream from the shock wave, so the pressure wave speed is not constant. This differs with the literature, studies like Hartmann et al. (2013) and Jacquin et al. (2009) state that these waves have a constant velocity equal to -80 m/s in both cases. The present results give the possibility to directly estimate the total velocity of such waves using the first law of the thermodynamics, assuming ideal gas ($h = c_p \cdot T$), adiabatic flow and constant total temperature along the wind tunnel, as follows,

$$\begin{cases} h_0 = h + \frac{V^2}{2} \\ h = c_p \cdot T \end{cases} \quad \Rightarrow \quad T = T_0 - \frac{V^2}{2 \cdot c_p}$$

Where h is the enthalpy, V the velocity, c_p the specific heat capacity at constant pressure and T the temperature. Now, the speed of the sound can be derived as,

$$a = \sqrt{\gamma \cdot R \cdot T} = \sqrt{\gamma \cdot R \cdot \left(T_0 - \frac{V^2}{2 \cdot c_p} \right)}$$

Where γ is the air specific heat ratio and R is the air gas constant. All these parameters and variables are known so the speed of sound is defined at every position in the flow field. Taking the flow velocity values along a streamline in the region after the shock, the absolute velocity at which the upstream traveling waves travel can be computed as the difference between the local flow speed and the speed of sound,

$$U_{utw} = U_{loc} - a_{loc},$$

along the x direction. This result is plotted in Fig. 8.9, where the speed of the UTW has been computed along SL3 line, see Fig. 8.2, using the phase average velocity fields during two different phases of the flow. The reason is that the flow field behind the shock is markedly different between these two cases. During the upstream movement of the shock, an extended separated region with smaller flow velocities is encountered by the UTW during their upstream movement, reason for their higher upstream velocity compared to the shock-moving-downstream case in which reattachment is occurring at the shock foot. Note that under reattachment conditions (shock wave traveling downstream), the estimated velocity varies between -50 m/s and -100 m/s. Furthermore, the studies from Jacquin et al. (2009) and Hartmann et al. (2013) found that the speed of the upstream traveling waves was of the order of $-U_\infty \cdot (1 - M_\infty)/M_\infty = 0.37 \cdot U_\infty \approx -80$ m/s for a corrected $M_\infty = 0.73$ over two different supercritical airfoils, OAT15A and DRA2303, with chord lengths of 230 mm and 200 mm.

It has been demonstrated that the pressure waves coming from the trailing edge travel at the speed of sound relative to the flow, which means that their total velocity is not constant, but it depends on the flow speed at every location. It can be observed in Figs. 8.4 and 8.6 that the UTW line is not completely straight, it is steeper at the trailing edge region, suggesting higher velocities, and then it gets curved when moving towards the shock region, i.e. it decreases its velocity. This is in agreement with the fact that the free stream velocity increases when moving upstream towards the shock region, hence the absolute value of

the upstream traveling waves velocity decreases when moving upstream as it is defined as $U_{utw} = (U_{loc} - a_{loc})$.

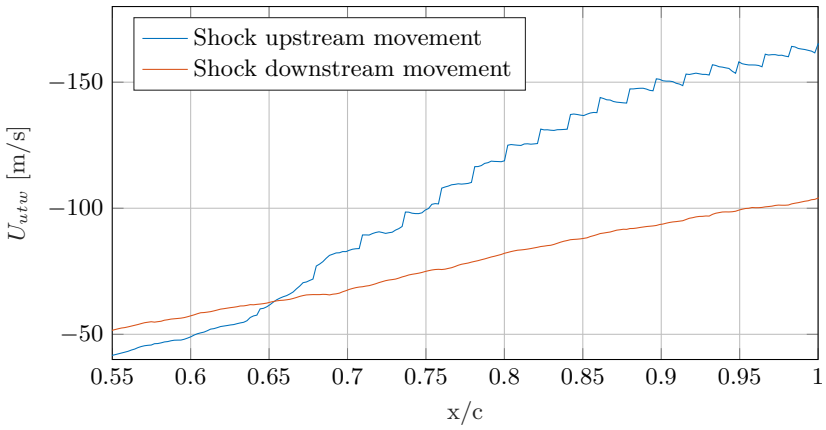

Figure 8.9: Theoretical estimated UTW velocity along the chord direction at buffet conditions over OAT15A at $\alpha = 3.5$ and $Ma = 0.70$.

8.2 Vortex shedding analysis

Lee (1990), Hartmann et al. (2013) and others based the buffet feedback loop explanation mainly on both the upstream traveling waves and the downstream traveling disturbances. In their research, Hartmann et al. (2013) stated that the vortices shed from the shock foot are the main cause of the creation of the upstream traveling waves and that a synchronization of frequencies exists between both phenomena. This section aims at obtaining the real velocity at which the vortices present in the flow are being convected downstream inside the separated region, and at estimating the order of magnitude of the shedding frequency in order to corroborate whether it coincides with the frequency of the upstream traveling waves, computed in section 8.1.

8.2.1 Vortex convection velocity

In order to obtain both the vortex displacement in time and their convection velocity, a cross-correlation analysis is carried out over pairs of consecutive images for two experimental cases, the first one over the OAT15A at $\alpha = 3.5°$ and $Ma = 0.70$ with fixed transition at $x/c = 7\%$, and the second one over the NACA0012 at $\alpha = 4°$ and $Ma = 0.70$ with free transition. The correlation is done over a reference area of the flow field centered in the separated region, in order to perfectly capture the vortices and to avoid the effect of other phenomena. The velocity term analyzed is the fluctuating term of the vertical velocity component, v', because it is precisely this component that better shows the location of the vortices. Note that two correlation analysis are done, one over the fully separated region from the shock foot, and one over the separated area in the trailing edge region when there is reattachment at the shock

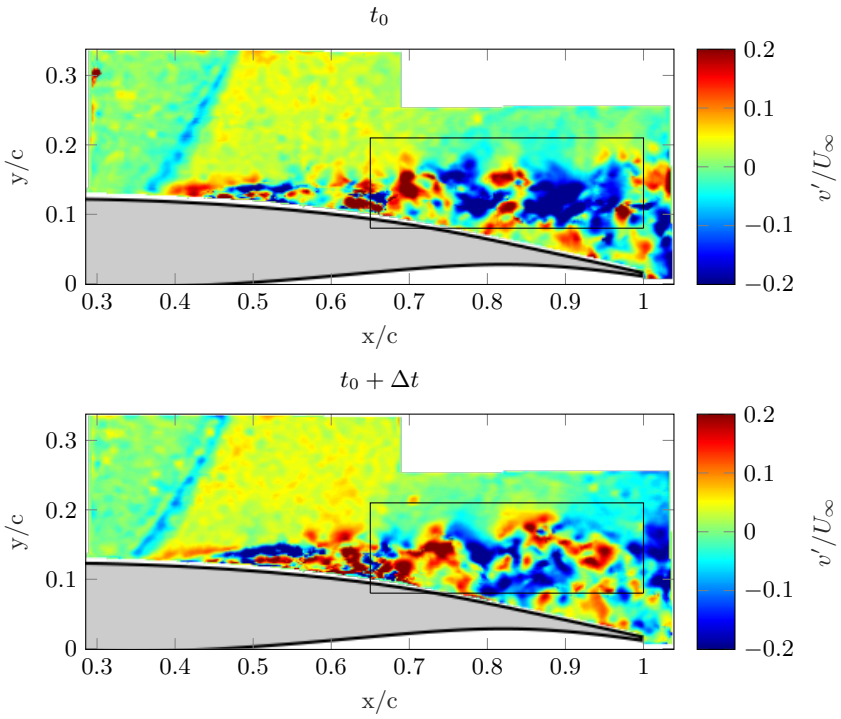

Figure 8.10: Cross-correlation area of the fully separated wake of OAT15A at $\alpha = 3.5°$ and $Ma = 0.70$.

foot.

Full separation from shock-foot

Firstly, all the images contained in Phases 03, 04 and 05 (as presented in the Phase-average description at 5.3.3) are analyzed, i.e. the phases that contain the upstream travel of the shock motion (03 and 04) and the most upstream shock position (05), where the separated region is most fully developed.

Figs. 8.10 and 8.11 show a pair of consecutive frames of the flow field containing the area of correlation for both the OAT15A and the NACA0012 models. In both cases the area used for the correlation has exactly the same size and position. Fig. 8.12 shows the results obtained from the correlation analysis of the OAT15A and the NACA0012 respectively, where the maximum correlation values are marked with a white square. The distance measured in these images is the displacement d of the vortices during one $\Delta t = 0.125$ ms. For the OAT15A a displacement of $d = 12.21$ mm is measured, whereas for the NACA0012 the displacement is $d = \sqrt{20.51^2 + 2.24^2} = 20.63$ mm. This allows for the computation of the velocity at which the shock-foot vortices are being convected downstream as follows,

$$U^{sf}_{vortex} = \frac{d}{\Delta t} \quad \Rightarrow \quad \begin{cases} U^{sf}_{vortex} \approx 100 & m/s \quad \text{for the OAT15A} \\ U^{sf}_{vortex} \approx 165 & m/s \quad \text{for the NACA0012} \end{cases} \tag{8.2}$$

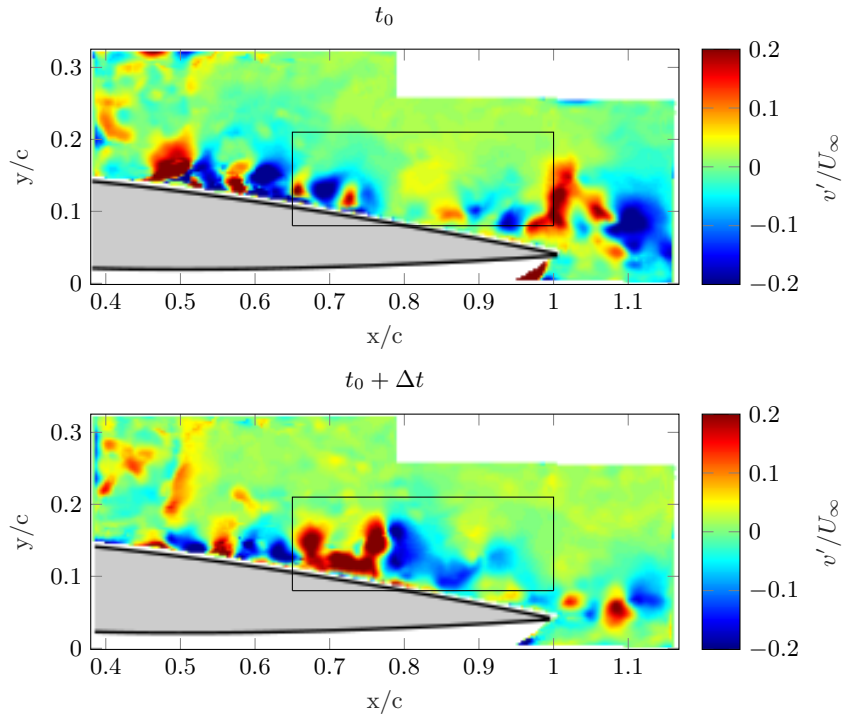

Figure 8.11: Cross-correlation area of the fully separated wake of NACA0012 at $\alpha = 4°$ and $Ma = 0.70$.

Where the superscript *sf* stands for *shock foot* as a reference of the origin of the vortices. Note that the speed of these vortices is in good agreement with the average speed at the separated shear layer presented in Figs. 5.9 and 5.13, measured as $0.5 \cdot U_\infty \approx 110$ for the OAT15A case, and $0.75 \cdot U_\infty \approx 170$ for the NACA0012 case. A question arises at this point as to whether any of the phenomena captured in the correlation analysis performed over the chord length in section 8.1 corresponds to the downstream convection of these vortices. It is clear in the case of the NACA0012 that the downstream traveling phenomena captured in Fig. 8.8 has a velocity of exactly the same order as the shed vortices, it is then safe to assume that both analysis refer to the same physical feature. However, this does not occur for the OAT15A, where the only phenomena captured in Fig. 8.4 are the upstream traveling waves that move upstream with a velocity of the order of the speed of sound with respect to the incoming flow.

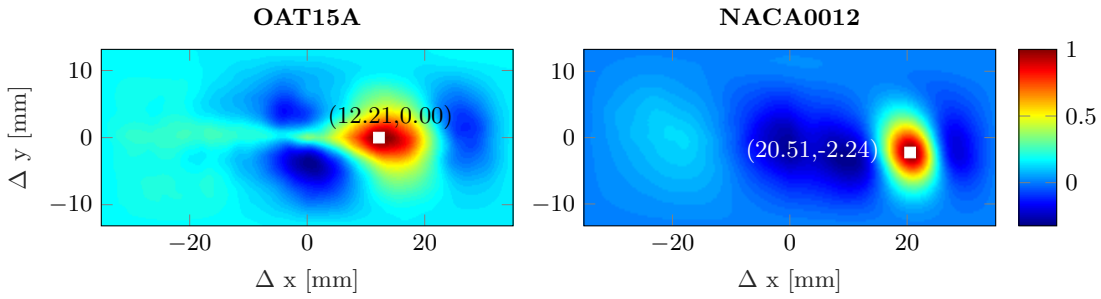

Figure 8.12: Average cross-correlation contour of the fully separated wake of OAT15A at $\alpha = 3.5°$, $Ma = 0.70$ and NACA0012 at $\alpha = 4°$, $Ma = 0.70$.

Trailing edge separation

During the buffet oscillatory cycle about the OAT15A airfoil, reattachment at the shock foot takes place during the downstream motion of the shock wave. This reattachment leads to the stop of the vortex shedding from the shock foot, however, it is important to note that still separation occurs at the trailing edge region. In this region different disturbances may be created that may affect the trailing edge. In principle, they may also have a different Strouhal number than the shock-foot vortex shedding. In order to corroborate this, the same analysis that was done over the fully separated region is done now over the trailing edge separated region. This analysis is not done over the NACA0012 as it was demonstrated that reattachment does not occur in any of the cycle Phases in this airfoil.

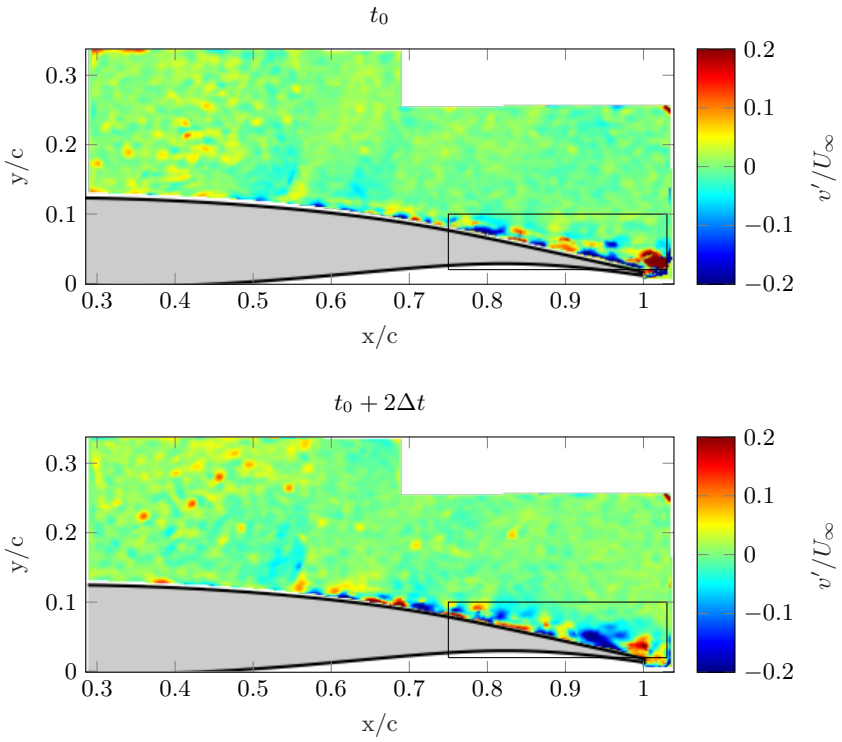

Figure 8.13: Cross-correlation area of the trailing edge separated wake of OAT15A at $\alpha = 3.5°$ and $Ma = 0.70$.

In this case, Fig. 8.13, a smaller wake region is taken as the reference area for the cross correlation, with a time separation equal to $2\Delta t$ since small displacements are expected, and only the time instants belonging to Phases 7 and 8 are analyzed, where reattachment occurs. Fig. 8.14 shows the averaged correlation map of the images. Note that the correlation procedure in this case is much less accurate than in the full separated wake. The reason is that the region being analyzed is too close to the airfoil surface so the phenomena being captured may be related to laser reflections on the surface. Also outliers due to lack of seeding near the surface and the small size of the features make this analysis much less accurate.

The result of the correlation is a crest of values that present a range of displacements, and that it is not centered exactly at the origin but slightly shifted. Note that this crest actually follows the path traveled by the disturbances, i.e. the curvature of the airfoil region edge. A small displacement value is being captured, ranging between 1 to 2 mm per Δt. The correlation map captures two local maximum values, one placed at the origin and another one indicated by a white square in Fig. 8.14. This local peak is taken as the average displacement, however, the fact that a clear single peak is not being captured leads to a cross-correlation analysis that may not be accurate enough as to predict an exact displacement, but that can give an estimated value. In order to compute a velocity based on this results, the displacement is taken as $d = \sqrt{2.95^2 + 0.63^2} = 3.02$ mm. Now, the velocity of the vortices can be estimated using a time interval of $2\Delta t = 0.25$ ms,

$$\boxed{U^{te}_{vortex} = \frac{d}{2\Delta t} \quad \Rightarrow \quad U^{te}_{vortex} \approx 12 \quad m/s \quad \text{for the OAT15A}} \tag{8.3}$$

Where the superscript *te* stands for *trailing edge* as a reference of the separated region location. The value obtained of 12 m/s seems rather low for vortex convective velocity taking into account the velocity at the shear layer in the phase-average flow fields, e.g. about 100 m/s. On the other hand, the order of magnitude of this velocity agrees with the experiments by Hartmann et al. (2013), where they found velocities of 19 m/s in the same region for a DRA2303 supercritical airfoil. This suggests that such downstream traveling disturbances may not be vortices but a different type of disturbances, however this cannot be corroborated with the present results. Moreover, in Chapter 9 it is demonstrated that using Lee's formula for the determination of the frequency of buffet, a downstream traveling disturbance with velocity of order of magnitude $\sim o(10)$ would agree with the actual buffet frequency measured in these experiments ($\sim$ 160 Hz). Hence, this value can be used as a reference of the order of magnitude. This phenomenon was not first captured in the correlation analysis of the velocity field of the OAT15A airfoil in Fig. 8.4. Furthermore, using that analysis it was not even possible to capture a phenomenon with such a low speed due to time discretization issues.

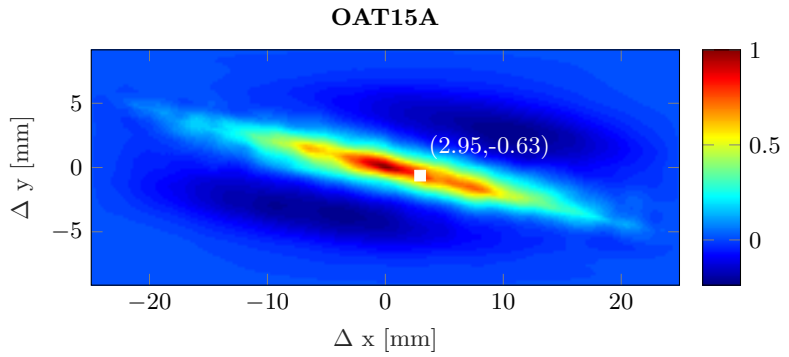

Figure 8.14: Cross-correlation area of the trailing edge separated wake of OAT15A at $\alpha = 3.5°$ and $Ma = 0.70$.

8.2.2 Vortex shedding frequency

Once the velocity at which the disturbances are convected downstream is known, it is possible to compute their characteristic frequency if their wavelength is previously estimated. In order to do so an auto-correlation of the wake region described in Figs. 8.10, 8.11 and 8.13 is done. This analysis is similar to the one performed before, only now the correlation is not between two consecutive frames but over the same frame, so that the distance between likewise flow features (as the vortices) present in the same region at the same instant is computed.

Full separation from shock-foot

It was found that the results for the instantaneous auto-correlation maps differ very much between the different instantaneous frames, which leads to an averaged result that does not provide very truthful information. Some of the instantaneous maps provide strong information while others are not so clear. The reason for this is that the vortices actually develop along the chord line changing greatly its size and shape, so the autocorrelation does not detect them equally. In order to demonstrate and comment this effect, two instantaneous auto-correlation maps are shown in Fig 8.15 for each of the aerodynamic models. In these images 2 white squares indicate the 2 main maximum peaks that appear in the correlation map and their associated displacement. In the instantaneous frame presented in image a) the vortices are clearly detected and the result of the correlation is a well defined vortex distance, however this is not the common case, the amount of images that show this clear information is small. On the other hand the image b) presents a random instantaneous frame in which it is clear that the vortices are not properly being detected by the correlation and, hence, the distances presented are not correct. From the images a) a clear vortex distance can be computed, e.g. 16.5 mm for the OAT15A and 22.8 mm for the NACA0012. These values cannot be taken as a definitive distance as they belong to an specific time instant, however they can be used as a reference to compare the averaged correlation results.

Fig. 8.16 represents the average auto-correlation maps for the OAT15A and the NACA0012 along all the frames belonging to phases 3, 4 and 5 as defined in the phase-average. As it was mentioned, a second maximum peak is not captured in these average auto-correlation maps as a result of the fact that the greater part of the frames lead to instantaneous results for the auto-correlation similar to the ones presented in image b) of Fig. 8.15, where the vortices are not being properly captured (even if a conditional average is applied). Nevertheless, as an estimation, it can be assumed that the distance between the vortices is actually similar to their wavelength, i.e. that the vortices are close to each other. Under this assumption the final vortex distance can be computed as twice the distance between the downwash and the upwash part of the vortex, i.e. twice the distance between a maximum and a minimum in the auto-correlation maps. Note that this assumption is well corroborated by the instantaneous maps in Fig. 8.15.

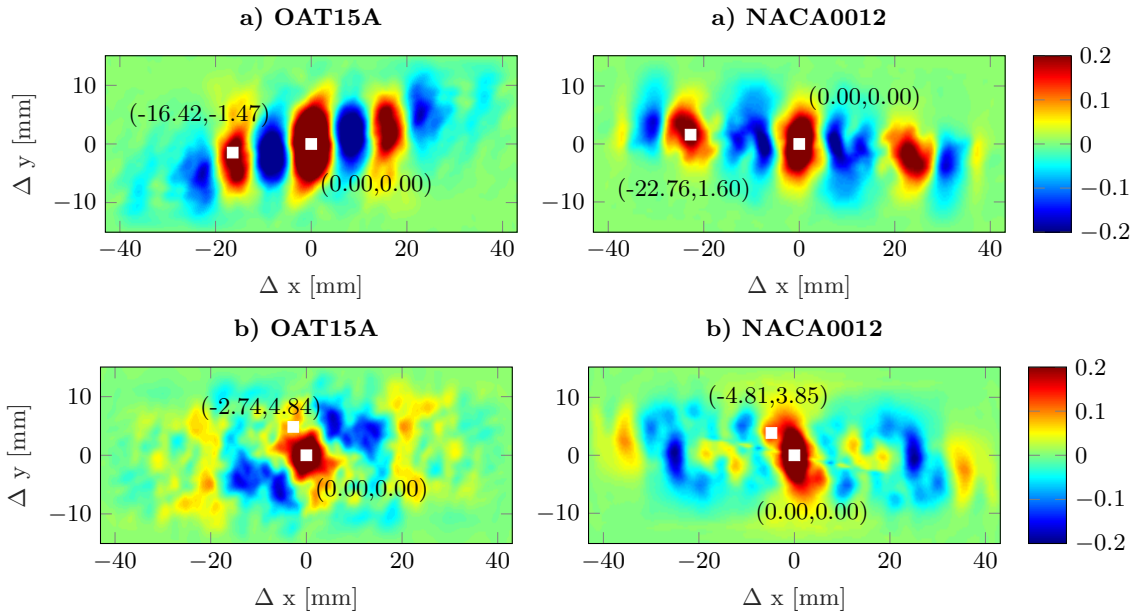

Figure 8.15: Instantaneous auto-correlation contours of the fully separated wake for a) good visualized and b) bad visualized vortices.

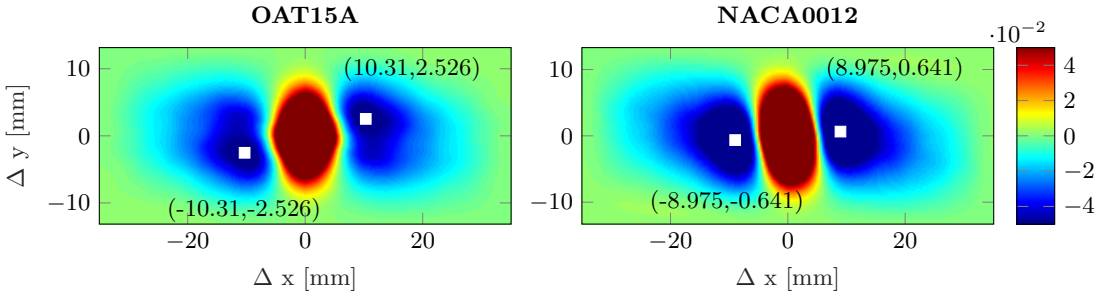

Figure 8.16: Average auto-correlation contour of the fully separated wake of OAT15A at $\alpha = 3.5°$, $Ma = 0.70$ and NACA0012 at $\alpha = 4°$, $Ma = 0.70$.

Finally, the distances shown in Fig. 8.16 can be taken as half the wavelength of the vortices from both aerodynamic models. The wavelength is then computed as

$$\begin{cases} \lambda^{sf}_{vortex} = 2 \cdot \sqrt{10.31^2 + 2.53^2} = 21.23 \quad mm \quad \text{for the OAT15A model,} \\ \lambda^{sf}_{vortex} = 2 \cdot \sqrt{8.98^2 + 0.64^2} = 18 \quad mm \quad \text{for the NACA0012 model.} \end{cases} \tag{8.4}$$

Now, comparing these wavelengths with the reference ones computed from the instantaneous cases (16.5 mm for the OAT15A, 22.8 mm for the NACA0012) it can be stated that they both agree in the order of magnitude, with values close to 20 mm. The computation of the shedding frequency at the shock foot is done using the velocities obtained in Eq. 8.2, as

follows,

$$\boxed{f^{sf}_{shed} = \frac{U^{sf}_{vortex}}{\lambda^{sf}_{vortex}} \quad \Rightarrow \quad \begin{cases} f^{sf}_{shed} \approx 5000 \quad Hz \quad \Rightarrow Str = 0.27 \quad \text{OAT15A} \\ f^{sf}_{shed} \approx 9000 \quad Hz \quad \Rightarrow Str = 0.48 \quad \text{NACA0012} \end{cases}} \tag{8.5}$$

Where the Strouhal number is computed as $Str = fL/U_\infty$ based on the airfoil thickness (12.3% for the OAT15A and 12% for the NACA0012) and on the free stream velocity for the current aerodynamic conditions ($U_\infty \approx 225$ m/s). Take into account that this Strouhal refers to the shedding of the vortices from the shock foot, and not to the shedding associated to the trailing edge of the airfoil.

Trailing edge separation

The same auto-correlation analysis is applied to the trailing edge separated region in the phases that gather the shock wave downstream movement, i.e. the phases where reattachment takes place at the shock foot and the separation is restricted to the trailing edge region. Fig. 8.17 shows the auto-correlation map for an instantaneous frame in which the disturbances are properly captured in order to have a reference value to corroborate the result from the averaged auto-correlation map presented in Fig. 8.18.

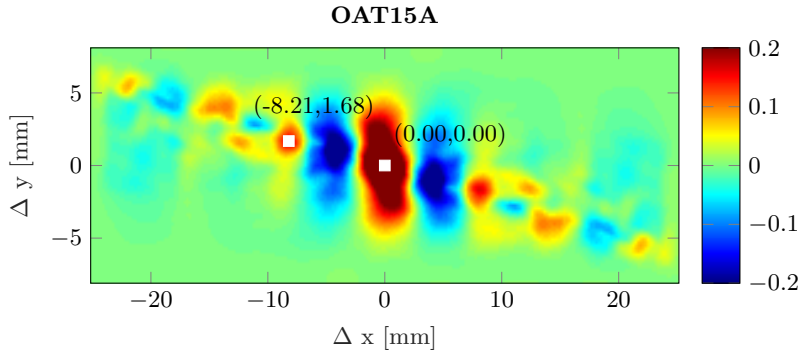

Figure 8.17: Instantaneous auto-correlation contour of the trailing edge separated region of OAT15A at $\alpha = 3.5°$ and $Ma = 0.70$.

The instantaneous correlation map in Fig. 8.17 gives a reference value for the disturbances distance equal to $d_{inst} = \sqrt{8.21^2 + 1.68^2} \approx 8$ mm, which can give an idea of the expected order of magnitude in the averaged auto-correlation map of Fig. 8.18. This average map shows again a crest of values coincident with the edge of the airfoil surface. Possible laser reflections and outliers due to the closeness of the surface may affect the correlation, which indicates that the result may not realistically represent the flow behavior. A total maximum is found at the origin for obvious reasons, and a relative local maximum is found that indicates the average distance between the vortices. However, this relative maximum is rather weak. Again the sensitivity of the auto-correlation is not too high because the velocity fields do not show accurately the disturbances development in a distance so close to the airfoil surface and this leads to the lack of a clear peak as it was obtained for the fully separated wake.

The wavelength of the disturbances is computed taking the relative local maximum as the averaged distance,

$$\lambda^{te}_{vortex} = \sqrt{5.26^2 + 1.26^2} = 5.4 \quad mm \tag{8.6}$$

Using this wavelength an the estimated convective velocity of the vortices of 12 m/s from Eq. 8.3, the vortex shedding frequency can be derived as,

$$\boxed{f^{te}_{shed} = \frac{U^{te}_{vortex}}{\lambda^{te}_{vortex}} \quad \Rightarrow \quad f^{te}_{shed} \approx 2000 \quad Hz \quad \Rightarrow Str = 0.12 \quad \text{OAT15A}} \tag{8.7}$$

Where the Strouhal number is computed as $Str = fL/U_\infty$ based on the airfoil thickness (12.3% for the OAT15A) and on the free stream velocity for the current aerodynamic conditions ($U_\infty \approx 225$ m/s). Note the difference between the physical meaning of this Strouhal and the Strouhal computed in Eq. 8.5. This Strouhal is related to the shedding frequency from the trailing edge of the airfoil when separation occurs in the trailing edge region exclusively, whereas in Eq. 8.5 it refers to the shedding taking place at the shock foot due to the shock wave - boundary layer interaction, two different phenomena.

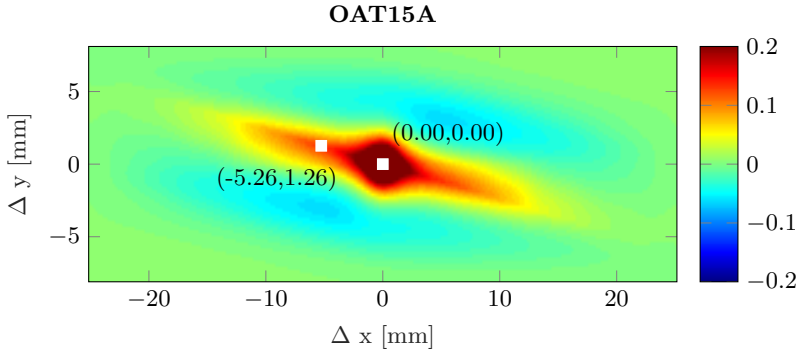

Figure 8.18: Average auto-correlation contour of the trailing edge separated region of OAT15A at $\alpha = 3.5°$ and $Ma = 0.70$.

8.3 Conclusions

The presence of the upstream traveling waves was demonstrated by plain view of the velocity fields and by a correlation analysis for the OAT15A airfoil (Figs. 8.4, 8.6 and 8.7), however not for the NACA0012, either because they are too weak to be captured by such analysis or simply because they are not being created in a periodic manner. These waves have a characteristic frequency that range between $f_{utw} \approx 2000 - 4000$ Hz and travel upstream from the trailing edge at an average velocity of -80 m/s. Furthermore, they are better captured without the presence of full separation from the shock wave foot, which suggests either that the separated region masks these disturbances or that it weakens and cancels their creation. On the other hand, the same analysis revealed the presence and movement of the shedding vortices generated at the shock foot along the chord on the NACA0012 at a convective

velocity about 160 m/s, see Fig. 8.8.

Cross-correlation and auto-correlation analyses were performed over the fully separated wake region in order to compute the convective velocities and frequencies of the vortices generated at the shock foot of both airfoils. They were found to be 100 m/s and 5 kHz for the vortices in the OAT15A case and 165 m/s and 9 kHz for the vortices in the NACA0012 case. This difference in characteristic frequencies between the vortices shed at the shock foot and the upstream traveling waves suggests that actually such vortices may not be the direct cause for the creation of the pressure waves, and hence they are originated by a different mechanism. Furthermore, having estimated these values for the characteristic frequencies and velocities, an explanation can be given about the buffet feedback loop including these phenomena and that would gather all the features involved in the motion cycle.

Moreover, cross-correlation and auto-correlation was applied over the separation at the trailing edge region when reattachment occurs at the shock foot for the OAT15A at $\alpha = 3.5°$ and $Ma = 0.70$ case. The reattachment forces the stop of the vortex shedding from the shock foot, but there are disturbances that travel downstream in the trailing edge separated region. This is also clear in the case of OAT15A at $\alpha = 2°$ and $Ma = 0.70$ where no massive separation occurs at the shock foot. In principle, it can be assumed that these two types of wakes have different Strouhal numbers associated. One is associated with the shock wave/boundary layer interaction, whereas the other is associated with the trailing edge flow behavior of the airfoil. The PIV results near the airfoil surface are not giving accurate results as they may contain errors and outliers due to surface laser reflections and lack of seeding. It is not possible to ensure that these disturbances are actually vortices, but it has been demonstrated that their behavior and nature differ from that of the vortices shed from the shock foot, i.e. the dynamics of the disturbances present in both types of wakes is different. The small order of magnitude of the convective velocities obtained for these disturbances (12 m/s) is in agreement with the results from Hartmann et al. (2013), who also found disturbances traveling at 19 m/s.

An order of magnitude estimate for the frequency of these disturbances showed that they may actually be the cause of the upstream traveling waves for different reasons. Firstly, they take place right at the trailing edge region and very close to the airfoil surface, where the sound pressure waves are generated. Secondly, their frequency was estimated to be of a similar order of magnitude than the UTW, i.e. 2000 Hz. Furthermore, this would explain the reason why no upstream traveling waves were found in the NACA0012 airfoil case, because no reattachment for this airfoil is occurring and the wake is always developing from the shock foot to the trailing edge.

Chapter 9

Discussion of buffet mechanism

The purpose of this chapter is to present an overall view of the buffet development taking into account not only the shock motion and the general flow behavior as it was done in Chapter 5, but including the vortex shedding mechanism and the upstream traveling waves motion. The aim is to answer the main research question of this experimental project, which was stated as the study of the features of the flow that play a mayor role in the feedback loop of the buffet phenomenon, trying to improve the current physical understanding of the links between those features that make possible the self-sustained character of the oscillatory motion.

In order to do so, a complete buffet cycle over the OAT15A airfoil at $\alpha = 3.5°$ and $Ma = 0.70$ is analyzed, starting from the most downstream position of the shock wave and dividing it into 8 different phases as it was done for the phase-average. The shock mean position ($\tilde{x}/c = 0.5$) and its displacement limits ($\Delta(x/c) = 0.4$) are taken from statistical data, and the time is approximated and treated as a discrete series of $\Delta t = 0.125$ ms in order to ease the understanding of the cycle. The buffet frequency is taken as 160 Hz as measured in Chapter 7, which leads to an average shock velocity of 13 m/s and a total cycle time of $50\Delta t$ (6.3 ms), which are equally divided into the 8 phases, $6\Delta t$ per phase approximately. Note that this equal distribution of time over the phases and the time discretization itself may introduce a small error since the shock is actually traveling at different velocities over the cycle. However, this error may be neglected as this is a qualitative presentation of a single cycle. It would be different if a proper analysis of concatenated cycles was desired, where the error would accumulate.

The frequencies estimated for the shock foot vortex shedding in Chapter 8, 5000 Hz for OAT15A and 9000 Hz for NACA0012, indicate a total amount of vortices being shed per buffet cycle approximately equal to 32 (4 per phase) for the OAT15A and 56 (7 per phase) for the NACA0012. On the other hand, the frequency of 2000 Hz found for the upstream traveling waves and the trailing-edge-separation shed disturbances lead to a total amount of around 12 per cycle (1.5 per phase). The frequency difference between the vortices shed from

the shock foot and the upstream traveling waves demonstrates that both phenomena are actually not linked, however the similarity with the frequency of the disturbances shed in the trailing edge separated region suggests that the reason for the creation of such pressure waves may be in these disturbances. In the present chapter, such disturbances will be treated as vortices for clarity reasons, even though it was not possible to demonstrate their actual nature.

Furthermore, the velocity at which vortices and UTW travel in the flow field was determined, this allows for the application of Lee's model for the frequency of the self-sustained shock oscillations, Lee (2001). The model states that the buffet period is equal to the addition of the time it takes the downstream disturbances to reach the trailing edge and the time it takes the UTW to reach the shock. The correction introduced by Hartmann et al. (2013) to Lee's relation is used. This correction estates that the UTW actually affect the shock at the region most distant to the shock foot. The model is first applied using the vortices shed at the shock foot as the downstream traveling disturbances, in order to corroborate that they do not hold such relation. The frequency obtained from Lee's model using the shock-foot shed vortices (f^{sf}) is,

$$f^{sf} = \left(\frac{c - \tilde{x}_{shock}}{U_{down}} + \frac{\sqrt{(c - \tilde{x}_{shock})^2 + z_{shock}^2}}{U_{utw}} \right)^{-1} = \left(\frac{0.05}{100} + \frac{0.095}{80} \right)^{-1} \approx 590 \quad Hz. \tag{9.1}$$

Where $z_{shock} = 0.8 \cdot c$ is taken from Hartmann et al. (2013). This demonstrates again that the shock-foot shed vortices are not the cause for the upstream traveling pressure waves since the frequency value obtained differs largely from the actual buffet frequency (160 Hz). Actually, a velocity for the downstream traveling disturbances of the order of ~ 10 m/s would be needed in order to get values of $f \approx 160$ Hz, the actual buffet frequency, as demonstrated by

$$f = \left(\frac{c - \tilde{x}_{shock}}{U_{down}} + \frac{\sqrt{(c - \tilde{x}_{shock})^2 + z_{shock}^2}}{U_{utw}} \right)^{-1} = \left(\frac{0.05}{o(10)} + \frac{0.095}{80} \right)^{-1} \approx 160 \quad Hz. \tag{9.2}$$

This velocity of o(10) m/s for the downstream traveling pressure disturbances suggests that the disturbances shed from the separated trailing edge region are a more suitable flow phenomenon to comply with Lee's theorem. However, the uncertainty in the cross-correlation and auto-correlation procedures to capture the dynamic behavior of such disturbances makes it difficult to obtain the proper values out of Lee's relation. This demonstrates again that the vortices shed from the shock foot do not originate the upstream traveling waves, however the pressure waves shed in the trailing edge region separation are very likely to be the cause although further analysis of the wake would be needed.

The velocities of the shed vortices and the upstream traveling waves allow to determine the time they require to travel from shock foot to trailing edge and vice versa for the 8 different phases of the buffet cycle. Table 9.1 gathers the dynamic parameters of these disturbances, namely the characteristic frequency, convection velocity and amount per phase. On the other hand, Table 9.2 contains the mean shock position per phase, the time

(measured in amount of Δt) it takes a vortex shed at each phase to reach the trailing edge (t_{vort} SF for vortices shed at the shock foot, and t_{vort} TE for vortices shed in the trailing edge separated region), and the time it takes to an UTW created at each phase to reach the shock foot (t_{utw}). Note that the origin of the trailing-edge-shed vortices is taken at $x/c = 0.65$ and that they are only shed in Phases 1, 6, 7, and 8, when there is reattachment at the shock foot. Shock foot shedding vortices take place in Phases 2, 3, 4 and 5, when separation starts from the shock foot. This data is used to reconstruct the buffet oscillation cycles presented in Fig. 9.1 for the OAT15A at $\alpha = 3.5°$ and $Ma = 0.70$.

	OAT15A			**NACA0012**		
	f [Hz]	U_{conv} [m/s]	# per phase	f [Hz]	U_{conv} [m/s]	# per phase
Vortices SF	5000	100	4	9000	165	7
Vortices TE	∼2000	∼ 12	1.5	-	-	-
UTW	2000	-80	1.5	-	-	-

Table 9.1: Vortices and UTW dynamic parameters

Phase	**01**	**02**	**03**	**04**	**05**	**06**	**07**	**08**
t	0	$6\Delta t$	$12\Delta t$	$18\Delta t$	$24\Delta t$	$30\Delta t$	$36\Delta t$	$42\Delta t$
$\tilde{x}_{shock}/c$	0.7	0.6	0.5	0.4	0.3	0.4	0.5	0.6
t_{vort} SF	-	$3.2\Delta t$	$4\Delta t$	$4.8\Delta t$	$5.6\Delta t$	-	-	-
t_{vort} TE	$\sim 20\Delta t$	-	-	-	-	$\sim 20\Delta t$	$\sim 20\Delta t$	$\sim 20\Delta t$
t_{utw} Δt	$3\Delta t$	$4\Delta t$	$5\Delta t$	$6\Delta t$	$7\Delta t$	$6\Delta t$	$5\Delta t$	$4\Delta t$

Table 9.2: Vortices and UTW dynamic parameters for the OAT15A case

The sketch plotted in Fig. 9.1 shows the dynamic development of a buffet cycle. The sketch contains:

- The 8 phases of the shock oscillation starting from the most downstream position (phase 1), the upstream travel of the shock wave (phases 2, 3, 4), the most upstream shock position (phase 5) and the shock wave downstream travel (phases 6, 7, 8). Every phase cover a time approximately equal to $6\Delta t$.
- In every phase the shock is presented in its original (shaded) and final positions with the direction of its motion indicated by a black arrow.
- The separated region is shown by a dashed line, starting either from the shock foot or from $x/c = 0.65$, depending on the type of wake.
- The vortices shed at the shock foot (in red) are presented in their original location (shock foot) and in their final location (trailing edge).
- The vortices shed at the trailing edge separated region (in purple) are shown in its original and final locations, i.e. $x/c = 0.65$ and the trailing edge respectively.
- The upstream traveling waves are shown in their original (trailing edge) and final (shock wave) locations.

The numeric labels associated to every element refer to the Phase in which they were originated, so that the phase delay between its original and final position can be directly inferred. The behavior of the flow features described next is based on the results and flow field observations from Chapters 5, 7 and 8.

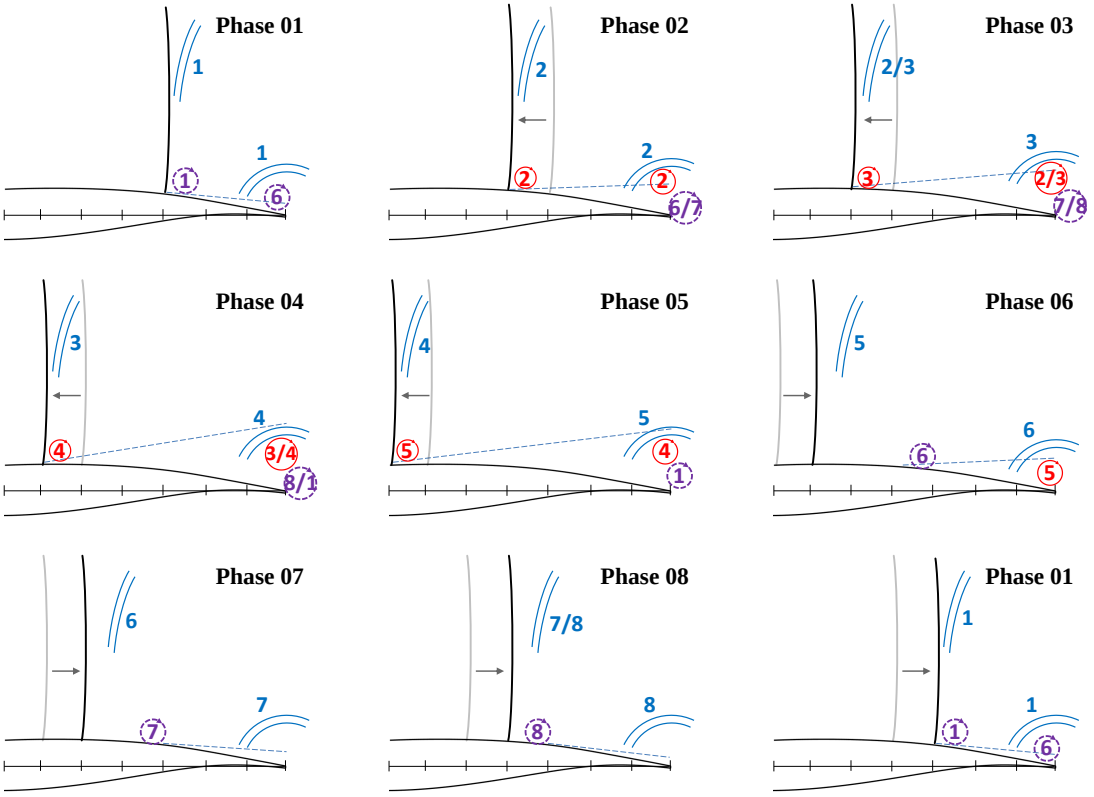

Figure 9.1: Schematic representation of the flow field during one buffet cycle containing the vortices shed from the shock foot (in red), the vortices shed at the trailing edge separated region (in purple) and the upstream traveling waves (in blue). Chord discretized in $\Delta x/c = 0.1$, time between phases equal to $6\Delta t$. Numeric labels refer to the phase at which the disturbances are originated. Study case is OAT15A at $\alpha = 3.5°$, $Ma = 0.70$.

The shock wave moves at an average velocity of about 13 m/s between the most upstream ($x/c = 0.3$, Phase 5) and downstream ($x/c = 0.7$, Phase 1) locations, which leads to a displacement of $\Delta x/c \approx 0.1$ per phase. From phases 1 to 5 the shock moves upstream and separation takes place at the shock foot. The separation region increases its size until it reaches the most upstream position where reattachment occurs, this is shown in Fig. 9.1 by a dashed blue line. During this upstream travel of the shock, vortices are shed from the shock foot (red vortices) at 5000 Hz that travel downstream at a speed of 100 m/s. Once reattachment occurs, the shock starts its downstream movement during phases 6 to 8. Separation occurs at a fixed location $x/c \approx 0.65$ and new vortices are shed in this region (purple vortices) at about 2000 Hz that travel downstream at a speed of around 12 m/s. During the whole buffet cycle, sound pressure waves are created at the trailing edge that expand in every direction. These waves travel upstream at a total velocity of 80 m/s. It is important to keep in mind for the

explanation of the buffet cycle development that the vortices shed at the shock foot and the upstream traveling waves are not considered to be coupled/linked, contrary to what was done by Hartmann et al. (2013) in their discussion. It has been demonstrated that the origin of the UTW does not lay in those vortices directly, and hence, that the strength of such waves may not be influenced by them. This leads to a new approach for the explanation of the oscillatory cycle and the reasons for its self-sustained character in which it is of paramount importance to demonstrate the real influence that the UTW have over the shock wave motion.

Focusing first on the vortices shed from the shock foot (red vortices), they are only shed during the upstream motion of the shock wave, when separation occurs from the shock foot and extends up to the trailing edge. During the first steps of the upstream motion of the shock (phases 2 and 3), the vortices arrive to the trailing edge within the same phase that they are created due to the proximity of the shock wave. However, a small delay starts appearing during these phases, meaning that the last vortices created during a phase may arrive to its destination at the beginning of the next phase (the delay is noted as a double digit label for a phenomenon at its final position, meaning that vortices that were created at two different phases are arriving to the trailing edge at that phase). This small delay keeps increasing and by the end of the upstream motion of the shock (phases 04 and 05) the delay is already of 1 whole phase, meaning that the vortices created at the shock foot at a specific phase will arrive to the trailing edge within the next one. It can be highlighted then that the maximum delay observed during the buffet cycle is of 1 phase and it occurs when the shock is near its most upstream position due to its remoteness to the trailing edge. Note the difference with Hartmann et al. (2013) description, where the delays observed for the vortices shed at the shock foot were of almost 1 whole buffet cycle.

When the shock reaches its most upstream position (phase 5), reattachment occurs at the shock foot stopping the vortex shedding. Nevertheless, separation still takes place, from $x/c \approx 0.65$. This separated region remains constant in size during the shock wave downstream motion. In this region new disturbances are being shed from the shear layer. The analysis of these disturbances did not give results with the necessary accuracy due to the proximity to the airfoil surface, as explained in Chapter 8. However, the results obtained can give an idea of their dynamic behavior. Starting at the beginning of the downstream travel of the shock (phase 6), the vortices are originated at $x/c \approx 0.65$ at every phase and they extend to the trailing edge with a velocity of about 12 m/s, i.e. they take around 3 phases ($\sim 20\Delta t$) to move from its origin to the trailing edge. Then, considering velocities of this order of magnitude, this actually demonstrates that in general the vortices that are generated during the downstream motion of the shock (phases 6, 7, 8 and 1) will reach the trailing edge during the upstream motion of the shock (phases 1, 2, 3, 4 and 5). This leads to a delay of roughly half a buffet cycle, as shown in Fig. 9.1.

Focusing on the upstream traveling waves, in this dynamic sketch it is possible to associate which UTW are being influenced by which vortices when they pass over the trailing edge, and to know when those specific waves reach the shock. The vortices created during the shock downstream motion (phases 6 to 8 and 1) arrive to the trailing edge during the shock upstream motion (phases 1 to 6) and it is then when they create the upstream traveling waves, which will travel upstream and reach the shock still during its upstream motion. Also vortices shed from the shock foot are arriving to the trailing edge in those phases, however

they are convected upward, away from the airfoil surface.

On one hand, it is shown here that the upstream traveling waves are arriving to the shock mostly during its upstream travel. On the other hand, it was shown in Fig. 8.4 that the upstream traveling waves are captured both during the upstream and downstream travel of the shock wave, however they appeared better in the shock downstream travel phases. The reason for this difference may be that during the upstream travel of the shock the separated region is masking the detection of such waves, but this demonstrates that indeed the upstream traveling waves are present through the whole buffet cycle. Now, the physical reason why these upstream traveling disturbances are generated during the whole buffet cycle, even, when separation starts at the shock foot and the frequency of those vortices does not match with the frequency of the UTW, is not fully clear. To give an accurate answer to this question, a detailed study of the trailing edge region should be performed in order to determine the real mechanisms that generates these waves.

An important question arises at this point, and that is how does the strength of the upstream traveling waves vary along the buffet cycle? It has been demonstrated in Fig. 9.1 how do the different disturbances behave dynamically along one cycle, however with these results it is not possible to make an exact conclusion about whether the UTW become significantly stronger during part of the cycle so that they may have a stronger effect over the shock wave. It can be hypothesized that the waves generated during the upstream movement of the shock wave are stronger due to the presence of the vortices close to the airfoil surface (disturbances generated at the trailing edge separated region during the shock downstream movement), and then those waves have a greater influence over the shock, forcing its upstream movement. Furthermore, this would explain why the shock shifts between upstream and downstream movements. During the shock downstream movement, at some point (Phase 1) the UTW gain strength due to the presence of the vortices at the trailing edge surface shed during the downstream shock motion (see Fig. 9.1). These waves force the shock to stop its downstream movement and separation is triggered from the shock foot. The upstream movement of the shock starts and it is maintained by the effect of both the UTW and the presence of the growing separated region at the shock foot. At a certain moment (Phase 5), the strength of the UTW and the separated region decreases, forcing the shock to stop and the flow to reattach at the shock foot. This would close the explanation for the self-sustained character of the buffet motion. However, the effect over the shock upstream motion of both, the upstream traveling waves and the presence of a massively separated region near the shock foot, must be balanced and thoroughly analyzed before making a conclusion about the actual reason for such shock motion.

For the NACA0012 airfoil case, it was not possible to capture the existence of the so called upstream traveling waves. Moreover, the separated region always starts from the shock foot and no reattachment is observed. In Fig. 7.3 the buffet peaks of energy associated to the phenomenon from the spectral analysis are plotted as function of Ma and α, it was shown that the highest peak for the NACA0012 case is actually of the same order of magnitude than the lowest peaks for the OAT15A, so taking this into account it could be stated that fully developed buffet conditions were not actually achieved for this standard airfoil in the present experiments. Fluctuations of the shock wave are observed, however they are much less periodic and defined than in the OAT15A case.

Chapter 10

Conclusions

A comprehensive experimental study of the unsteady development of the flow field about a NACA0012 and a OAT15A airfoils under transonic buffet conditions was done in the present project, with the main purpose of studying the physical mechanisms that sustain the phenomenon and that play a major role in the unsteady evolution of the flow field. The experimental approach followed for the analysis was based on 4 experimental campaigns. Firstly, one experimental campaign was done over each airfoil using Schlieren visualization, in order to analyze the aerodynamic conditions under which buffet is most fully developed and to be able to study the influence of the Mach number, the angle of attack and the boundary layer state over the phenomenon. Secondly, once the right values of these parameters for the complete development of buffet were known, a second campaign was done over each airfoil by means of time-resolved particle image velocimetry, in order to capture the evolution of the phenomenon. The results from these experiments showed that the flow over the OAT15A achieves a state of fully developed buffet at $Ma = 0.70$, $\alpha = 3.5°$ and transition fixed at $x/c = 7\%$, whereas for the case of the NACA0012 the phenomenon reaches its strongest state at $Ma = 0.70$, $\alpha = 4°$ and free transition, but buffet does not develops fully as it does for the OAT15A. This is the reason why the buffet development was further analyzed focusing on the OAT15A case, but also comparing it with different flow conditions and with the NACA0012 model.

Spectral analysis of the shock wave motion

A direct approach to measure the intensity of the buffet phenomenon under given aerodynamic conditions is by analyzing the shock motion characteristics. This was done by means of spectral analysis over all the available experimental test cases in Chapter 7. As expected, the results showed that buffet is confined to a range of values of aerodynamic parameters, specially of Ma, α and Re, and that out of this range the phenomenon vanishes. Buffet was found to be most developed in two cases (one per airfoil) that were labeled as *buffet cases*, the OAT15A at $\alpha = 3.5°$, $Ma = 0.70$ and fixed transition at $x/c = 7\%$, and the NACA0012 at $\alpha = 4°$, $Ma = 0.70$ and free transition. Even though the NACA0012 *buffet case* does not

present fully developed buffet, these cases were chosen to be the reference for the rest of the analysis and for comparison with other highly unsteady or characteristic cases. Furthermore, good agreement between the shock wave spectral analysis from PIV and Schlieren data was found, which suggests Schlieren visualization technique as a proper tool for buffet detection.

Unsteady flow behavior

The unsteady flow behavior of different study cases was analyzed and compared by means of the instantaneous and the phase average velocity fields, see 5.3.2, 5.3.3 and 5.4. It was shown that the flow behavior can be divided in two stages, the upstream and downstream shock wave motion. For the OAT15A model *buffet case* (OAT15A at $\alpha = 3.5°$, $Ma = 0.70$ and fixed transition at $x/c = 7\%$) an important difference between these 2 stages was found, i.e. during the upstream shock motion, separation occurs at the shock foot and develops massively beyond the trailing edge. The shock moves upstream as an oblique shock due to the presence of a massively separated region and the deflection of the flow that it causes near the shock foot. On the other hand, during the downstream shock motion reattachment takes place at the shock foot, and separation is confined to the trailing edge region. This leads to an intermittent recirculation phenomenon at the trailing edge, occurring during the upstream shock motion and disappearing during the downstream shock motion, see Fig. 5.12. The standard deviation of the shock motion amplitude was found to be $(x/c)_{rms} = 7.03\%$.

This flow field was then compared to other OAT15A model cases were buffet was not fully developed. It was found that, for smaller angle of attack but fixed Ma (OAT15A at $\alpha = 2°$, $Ma = 0.70$ and fixed transition at $x/c = 7\%$), separation was never taking place from the shock foot and it was confined to the trailing edge region without recirculating flow, but actually the shock wave motion was strong and periodic with a high amplitude $(x/c)_{rms} = 5.3\%$, which suggests a strong buffet effect. Moreover, for a case with fixed angle of attack but higher Ma (OAT15A at $\alpha = 3.5°$, $Ma = 0.73$ and fixed transition at $x/c = 7\%$), separation was always occurring from the shock foot, without reattachment. This lead to a constant recirculating flow at the trailing edge region. The shock wave motion amplitude was $(x/c)_{rms} = 3.84\%$, considerably smaller than in the other cases, suggesting weak buffet. On the other hand, the same analysis over the NACA0012 showed that separation was constantly occurring from the shock foot, with no reattachment at all during its downstream movement.

Waves propagation

The aim of this analysis was to capture the existence and characteristics of the so called *upstream traveling waves* and the vortices shed in the separated region with the purpose of linking them together into the explanation of the dynamic development of the flow under buffet conditions. The analysis consisted mainly in correlation procedures of specific regions of the flow for different test cases, following different approaches described in 4.2.

The analysis of the *upstream traveling waves* demonstrated their presence in some of the test cases for the OAT15A model. These waves are originated in the trailing edge

region and travel upstream until they reach the shock wave. They were found to have a characteristic frequency ranging between $\sim 2000 - 4000$ Hz and to move at an average velocity near -80 m/s in the upstream direction. However, it was also demonstrated that this velocity is not constant along their trajectory but it depends on the incoming flow velocity as $(U_{loc} - a_{loc})$. An important feature observed from these results is that whenever full separation takes place from the shock foot and extends downstream beyond the trailing edge, the upstream traveling waves are not properly captured in the correlation analysis of those phases. This suggests that the separation region is masking these disturbances. Precisely in those cases, back flow recirculation is found at the trailing edge region, which moves the vortices away from the airfoil surface, hence decreasing the noise generated there. On the other hand, the upstream traveling waves were not found for the NACA0012 test cases even though back flow recirculation does not occur at the trailing edge. The reason for the absence of these waves may be related to the fact that separation and vortex shedding always occurs at the shock foot. This does not happen for the OAT15A cases, where disturbances are generated at the trailing edge separated region when reattachment occurs at the shock foot. Another interesting feature was observed for the case OAT15A at $\alpha = 2°$, $Ma = 0.70$ and fixed transition at $x/c = 7\%$. In this case separation never develops massively from the shock foot, and the wake has an almost constant size (see Fig. 5.14), however, the shock motion is strong and wide and buffet conditions are achieved. The upstream traveling waves were nicely captured in this case, which suggests that actually they are the main element that causes and maintains the shock motion, since the separated region is almost steady.

Further correlation analysis of the separated regions of the *buffet cases* showed that actually the vortices being generated at the shock foot when massive separation takes place have a completely different frequency than the upstream traveling waves. For the OAT15A case these vortices were found to be generated at ~ 5000 Hz and to travel downstream at ~ 100 m/s, whereas for the NACA0012 they are created at ~ 9000 Hz and travel at ~ 165 m/s. This demonstrates that these vortices are not the cause for the creation of the UTW, fact that is not in agreement with previous studies. A correlation was made of the trailing edge separated region that occurs when the shock moves downstream and the flow is attached at the shock foot. It showed that disturbances exist that travel downstream inside this region and whose values of convection velocity and frequency may suggest that they are a feasible cause for the UTW creation. Nevertheless, this last correlation analysis was not accurate enough as the region of study falls near the airfoil surface where laser reflection and outliers due to lack of seeding are present. The nature and origin of these disturbances could not be demonstrated. Further analysis is needed in order to accurately describe the behavior of such disturbances, their velocity, frequency and origin.

Buffet dynamic description

The description of the dynamic evolution of the buffet phenomenon done in Chapter 9 can be summarized taking into account just the main events and dividing the whole cycle in two simplified stages, namely the upstream and downstream shock wave motions. Only the *buffet case* OAT15A at $\alpha = 3.5°$, $Ma = 0.70$ and fixed transition at $x/c = 7\%$ is considered for this explanation. When the shock wave starts its upstream movement separation occurs at the shock foot and develops massively beyond the trailing edge. During this upstream

movement, vortices are shed from the shock foot (red vortices in Fig. 9.1) and they reach the trailing edge, however it has been demonstrated that they are not responsible for the creation of the upstream traveling waves. Once reattachment occurs at the most upstream shock position, the shock starts its downstream travel. From this point, separation takes place in the region near the trailing edge, and new smaller vortices (purple vortices) are generated. These vortices travel downstream at much smaller velocities than the ones generated at the shock foot, they start reaching the trailing edge by the time the shock wave arrives to its most downstream position and keep arriving during part of the upstream shock motion. These vortices create pressure waves when passing over the trailing edge that spread in every direction, i.e. these are the upstream traveling waves (blue waves). These waves travel from trailing edge to shock wave at relatively high speeds, meaning that they keep reaching the shock wave during most part of its upstream travel. This dynamic analysis suggests, that actually the shock wave stops its downstream movement due to the beginning of the arrival of UTW to the shock location, then the upstream shock motion is maintained by the arrival of these waves and, finally, the shock stops its upstream movement due to the stop of the arrival of UTW to the shock location, meaning that these waves play a major role in the shock motion behavior.

Now, from the correlation analysis performed in Chapter 8, it is known that actually, the upstream traveling waves do not really stop arriving to the shock location during its downstream travel, since the UTW appear in the correlation maps during both stages. So, it is possible that actually there exists a modulation of the strength of such waves that modifies the effect that they have over the shock wave, making them stronger during the upstream shock motion and weaker during the downstream shock motion. This strength modulation was also proposed by Hartmann et al. (2013), but their dynamic explanation for the buffet cycle differs in some details to the one given in this study. If such modulation takes place, it is due to the conditions at the trailing edge at the time the waves are created. Further research is needed in order to study the real conditions under which these waves are generated and the cause and effect of the strength modulation.

10.1 Guidelines for future research

The present project has deepen into the understanding of the physical mechanisms that sustain the buffet oscillatory motion, especially focusing in the waves and vortices propagation, considered to be the less understood features of the cycle. Several key elements have been found to be in need of more research in order to close the explanation of the phenomenon, namely

1. To study more in detail the separated region development and the dynamic properties of the vortex shedding. The frequency and velocity of all the vortices present in the wake must be obtained by improving the correlation analyses done over the separated region and increasing the PIV acquisition rates.

2. To study the strength modulation of the upstream traveling waves and the dynamics of

its generation mechanism. Both the cause and the consequence for this possible modulation of the strength of such waves would be of paramount importance to corroborate the real effect of these waves over the shock wave motion

3. To balance the importance of the effect of the upstream traveling waves and the importance of other possible flow elements (for instance the massively separated region at the shock foot) over the shock wave upstream motion. Is the motion exclusively sustained by the upstream traveling waves as proposed by other authors?

4. To study the influence of different trailing edge configurations on the buffet phenomenon and on the creation of the upstream traveling waves, e.g. serrated trailing edge and Gurney flaps.

Bibliography

W.J. Bannink. Derde jaars praktikum compressibele aerodynamica hsl 2. *Delft University of Technology, Department of Aerospace Engineering*, 1987.

W.J. Bannink and P.G. Bakker. Transonic mach number determination in a blow-down wind-tunnel with solid walls and a downstream throat. *Delft University of Technology, Department of Aerospace Engineering, Report LR-402*, 1983.

G. Barakos and D. Drikakis. Numerical simulation of transonic buffet flows using various turbulence closures. *International Journal of Heat and Fluid Flow*, 21(5):620–626, 2000.

L.H. Benedict and R.D. Gould. Towards better uncertainty estimates for turbulence statistics. *Experiments in fluids*, 22(2):129–136, 1996.

A. Bouhadji. *Analyse physique par simulation numérique de phénomènes de transition bi- et tridimensionnels dans l'écoulement compressible, visqueux autour d'une aile d'avion.* PhD thesis, 1998.

A.L. Braslow, R.M. Hicks, and R.V. Harris. *Use of grit-type boundary-layer-transition trips on wind-tunnel models.* Citeseer, 1966.

V. Brunet, S. Deck, P. Molton, and M. Thiery. A complete experimental and numerical study of the buffet phenomenon over the oat15a airfoil. *ONERA: Tire a Part*, (35):1–9, 2005.

S. Butterworth. On the theory of filter amplifiers. *Wireless Engineer*, 7(6):536–541, 1930.

J.D. Crouch, A. Garbaruk, D. Magidov, and L. Jacquin. Global structure of buffeting flow on transonic airfoils. In *IUTAM Symposium on Unsteady Separated Flows and their Control*, pages 297–306. Springer, 2009.

S. Deck. Numerical simulation of transonic buffet over a supercritical airfoil. *AIAA journal*, 43(7):1556–1566, 2005.

B.F.R. Ewald. Agardograph 336: Wind tunnel wall correction. *Canada Communication Group Inc*, 1998.

K. Finke. Unsteady shock wave-boundary layer interaction on profiles in transonic flow. *AGARD Flow Separation 11 p(SEE N 76-17030 08-02)*, 1975.

J.C. Gibbings. *On boundary-layer transition wires.* HM Stationery Office, 1959.

A. Hartmann, A. Feldhusen, and W. Schröder. On the interaction of shock waves and sound waves in transonic buffet flow. *Physics of Fluids*, 25(2):026101, 2013.

W.F. Hilton and R.G. Fowler. *Photographs of shock wave movement*. HM Stationery Office, 1952.

R.A. Humble, F. Scarano, and B.W. Van Oudheusden. Unsteady flow organization of a shock wave/turbulent boundary layer interaction. In *IUTAM Symposium on Unsteady Separated Flows and their Control*, pages 319–330. Springer, 2009.

A.K.M.F. Hussain and W.C. Reynolds. The mechanics of an organized wave in turbulent shear flow. part 2. experimental results. *Journal of Fluid Mechanics*, 54(02):241–261, 1972.

L. Jacquin, P. Molton, S. Deck, B. Maury, and D. Soulevant. Experimental study of shock oscillation over a transonic supercritical profile. *AIAA journal*, 47(9):1985–1994, 2009.

LaVision. Lavision davis 8.3 product manual, 2015.

B.H.K. Lee. Investigation of flow separation on a supercritical airfoil. *Journal of Aircraft*, 26 (11):1032–1037, 1989.

B.H.K. Lee. Oscillatory shock motion caused by transonic buffet over aerofoils. *AIAA Journal*, 28(5):942–944, 1990.

B.H.K. Lee. Self-sustained shock oscillations on airfoils at transonic speeds. *Progress in Aerospace Sciences*, 37(2):147–196, 2001.

B.H.K. Lee and F.C. Tang. Transonic buffet of a supercritical airfoil with trailing-edge flap. *Journal of Aircraft*, 26(5):459–464, 1989.

L.L. Levy Jr. Experimental and computational steady and unsteady transonic flows about a thick airfoil. *AIAA Journal*, 16(6):564–572, 1978.

J.B. McDevitt. Supercritical flow about a thick circular-arc airfoil. 1979.

J.B. McDevitt and A.F. Okuno. Static and dynamic pressure measurements on a naca0012 airfoil in the ames high reynolds number facility. 1985.

J.B. McDevitt, L.L. Levy Jr, and G.S. Deiwert. Transonic flow about a thick circular-arc airfoil. *AIAA Journal*, 14(5):606–613, 1976.

A. Melling. Tracer particles and seeding for particle image velocimetry. *Measurement Science and Technology*, 8(12):1406, 1997.

T.H. Moulden. *Fundamentals of transonic flow*. Wiley-Interscience, 1984.

H.H. Pearcey. A method for the prediction of the onset of buffeting and other separation effects from wind tunnel tests on rigid models. Technical report, DTIC Document, 1958.

M. Raffel, C.E. Willert, S. Wereley, and J. Kompenhans. *Particle image velocimetry: a practical guide*. Springer, 2013.

S. Raghunathan, R.D. Mitchell, and M.A. Gillan. Transonic shock oscillations on naca0012 aerofoil. *Shock Waves*, 8(4):191–202, 1998.

D. Ragni. Piv-based load determination in aircraft propellers. 2012.

D. Ragni, F. Schrijer, B.W. Van Oudheusden, and F. Scarano. Particle tracer response across shocks measured by piv. *Experiments in fluids*, 50(1):53–64, 2011.

D. Rockwell. Oscillations of impinging shear layers. *AIAA journal*, 21(5):645–664, 1983.

F.W. Roos. Some features of the unsteady pressure field in transonic airfoil buffeting. *Journal of Aircraft*, 17(11):781–788, 1980.

F.F.J. Schrijer and F. Scarano. Effect of predictor–corrector filtering on the stability and spatial resolution of iterative piv interrogation. *Experiments in fluids*, 45(5):927–941, 2008.

H.L. Seegmiller, J.G. Marvin, and L.L. Levy Jr. Steady and unsteady transonic flow. *AIAA Journal*, 16(12):1262–1270, 1978.

O.M. Solomon Jr. Psd computations using welch's method. *NASA STI/Recon Technical Report N*, 92, 1991.

L.C. Squire. The motion of thin oil sheet under the boundary layer on a body. agardograph, pages 7–28. Technical report, AGARD-AG-70, 1969.

E. Stanewsky and D. Basler. Experimental investigation of buffet onset and penetration on a supercritical airfoil at transonic speeds. Technical report, DTIC Document, 1990.

Z. Sun. Micro ramps in supersonic turbulent boundary layers: An experimental and numerical study. 2014.

D. Szubert, F. Grossi, A.J. Garcia, Y. Hoarau, J.C.R. Hunt, and M. Braza. Shock-vortex shear-layer interaction in the transonic flow around a supercritical airfoil at high reynolds number in buffet conditions. *Journal of Fluids and Structures*, 55:276–302, 2015.

H. Tijdeman. *Investigations of the transonic flow around oscillating airfoils*. PhD thesis, TU Delft, Delft University of Technology, 1977.

F.M. White. *Viscous fluid flow*. McGraw-Hill International Edition, 2006.

Appendix A

Test matrices

A.1 PIV campaigns

2^{nd} Exp. Campaign - NACA0012 PIV				
Model	$\boldsymbol{\alpha}$ [°]	**Ma**	$\boldsymbol{f_{aq}}$ [kHz]	**Specifications**
NACA0012	0	0.78	8/20	
	2	0.70	8	
		0.75	8/20	
	4	0.70	8/20	
		0.75	8	Zig-zag trip at x/c=30%, $t = 0.2mm$
		0.75	8/20	
Notes: *(Apply to all tests unless "specifications" says different)* Laser probe inserted up to a 50% in all tests Free transition				

Table A.1: Test matrix 2^{nd} Experimental Campaign - NACA0012 PIV

4^{th} Exp. Campaign - OAT15A PIV				
Model	$\boldsymbol{\alpha}$ [°]	**Ma**	$\boldsymbol{f_{aq}}$ [kHz]	**Specifications**
OAT15A	0	0.78	8	
	2	0.70	8	
		0.73	8	
	3.5	0.70	8	
		0.73	8	
Notes: *(Apply to all tests unless "specifications" says different)* Laser probe inserted up to a 10% in all tests Fixed transition with Carborundum 500 at $x/c = 7\% - 9\%$				

Table A.2: Test matrix 4^{th} Experimental Campaign - OAT15A PIV

A.2 Schlieren visualization campaigns

1^{st} Exp. Campaign - Schlieren Visualization				
Model	$\boldsymbol{\alpha}$ [°]	**Ma**	$\boldsymbol{f_{aq}}$ [kHz]	**Specifications**
No model	-	0.75	1.5	No laser probe
		0.80	1.5	No laser probe
NACA0012	0	0.65	1.5	
		0.70	1.5	
		0.75	1.5	
		0.78	1.5/8	With/without laser probe
		0.80	1.5	
	2	0.65	1.5	
		0.70	1.5	
		0.73	1.5/3	
			1.5	Horizontal knife
			1.5	Pin hole 2mm
			1.5	Pin hole 3mm
		0.75	1.5/3/8	
			1.5	Deep knife
			1.5	No tape at pin hole
			1.5/3	$t_{exp} = 2\mu s$
		0.77	1.5/3	
		0.80	1.5	
	4	0.65	1.5	
		0.68	1.5/3	
		0.70	1.5	With/without laser probe
			3/8/16	
			1.5	No laser probe, opposite knife edge
			1.5	No laser probe, no knife
		0.72	1.5/3	
		0.75	1.5	
		0.80	1.5	

Notes: *(Apply to all tests unless "specifications" says different)*
Laser probe inserted up to a 50% in all tests
Free transition

Table A.3: Test matrix 1^{st} Experimental Campaign - Schlieren visualization

3^{rd} Exp. Campaign Part 1/2 - Schlieren Visualization				
Model	$\boldsymbol{\alpha}$ [°]	**Ma**	$\boldsymbol{f_{aq}}$ [kHz]	**Specifications**
No model	-	0.70	8	
		0.75	8	
		0.80	8	
OAT15A	0	0.70	2	
		0.73	2	
		0.75	2	
		0.80	2	
	2	0.65	2	
		0.68	2	
		0.70	2	
		0.73	2	
		0.75	2	
		0.77	2	
	3.5	0.63	2/4/8	
		0.65	2/4	
		0.66	8	
		0.67	4/8	
		0.70	4	
Notes: *(Apply to all tests unless "specifications" says different)* Laser probe inserted up to a 50% in all tests Free transition				

Table A.4: Test matrix 3^{rd} Experimental Campaign Part 1/2 - Schlieren visualization

3^{rd} Exp. Campaign Part 2/2 - Schlieren Visualization				
Model	$\boldsymbol{\alpha}$ [°]	**Ma**	$\boldsymbol{f_{aq}}$ [kHz]	**Specifications**
OAT15A	0	0.73	4	
		0.75	4	
		0.77	4	
		0.80	4	
	2	0.65	4	
		0.67	4	
		0.70	4	
		0.73	4	
		0.75	4	
		0.77	4	
	3.5	0.63	4	Free transition
		0.65	4	Free/fixed transition
		0.67	4	Free/fixed transition
		0.69	4	Free transition
		0.70	4	Laser probe inserted 0%/10%/50%
		0.71	4	Fixed transition by zig-zag t=0.2mm
			4	Fixed transition by Carborundum150
			4	Fixed transition by Carborundum500
		0.73	4	Free/fixed transition
		0.75	4	
NACA0012	0	0.75	4	
		0.77	4	
		0.78	4	
	2	0.73	4	
		0.75	4	
		0.77	4	
	4	0.67	4	
		0.70	4	Laser probe inserted 0%/10%/50%
		0.73	4	
		0.75	4	

Notes: *(Apply to all tests unless "specifications" says different)*
No laser probe
Fixed transition with Carborundum 500 at $x/c = 7\% - 9\%$

Table A.5: Test matrix 3^{rd} Experimental Campaign Part 2/2 - Schlieren visualization

A.3 Oil flow visualization campaigns

Oil visualization measurements			
Model	$\boldsymbol{\alpha}$ [°]	**Ma**	**Specifications**
NACA0012	4	0.70	Carborundum500/Free transition
OAT15A	3.5	0.71	Free transition
			Carborundum150
			Carborundum320
			Carborundum400
			Carborundum500
			Zig-zag t=0.2mm
Notes: *(Apply to all tests unless "specifications" says different)* Fixed transition at $x/c = 7\% - 9\%$			

Table A.6: Test matrix Oil visualization measurements

Appendix B

Analytical derivations

B.1 Test conditions

Knowing the total temperature and pressure in the reservoir and the Mach number in the test section, the static pressure and temperature in the test section can then be computed using the isentropic relations, as follows,

$$T_\infty = T_t \cdot (1 + \frac{\gamma - 1}{2} Ma^2)^{-1} \tag{B.1}$$

$$P_\infty = P_t \cdot (1 + \frac{\gamma - 1}{2} Ma^2)^{\frac{-\gamma}{\gamma - 1}} \tag{B.2}$$

Where γ is the specific heat ratio, which for air is $\gamma = 1.4$. Assuming also a calorically perfect gas, the flow density is computed using the ideal gas law,

$$\rho_\infty = \frac{P_\infty}{RT_\infty} \tag{B.3}$$

Where $R = 287.058 \left[\frac{J}{kgK}\right]$ is the air gas constant. Now, the viscosity in the test section is computed using Shuterland's law, as follows,

$$\mu_\infty = \mu_{ref} \cdot \left(\frac{T_\infty}{T_{ref}}\right)^{3/2} \cdot \left(\frac{T_{ref} + S}{T_\infty + S}\right) \tag{B.4}$$

The reference values μ_{ref} and T_{ref} can be taken as $\mu_{ref} = 1.716{\cdot}10^{-5} \left[\frac{kg}{m{\cdot}s}\right]$ and $T_{ref} = 273[K]$, see White (2006). $S = 111[K]$ is Sutherland's constant. Finally the flow speed in the test section can be computed and then the Reynolds number per unit length,

$$U_\infty = Ma_t \cdot \sqrt{\gamma R T_\infty} \tag{B.5}$$

$$\frac{Re_\infty}{L} = \frac{\rho_\infty U_\infty}{\mu_\infty} \tag{B.6}$$

B.2 Boundary layer thickness estimation

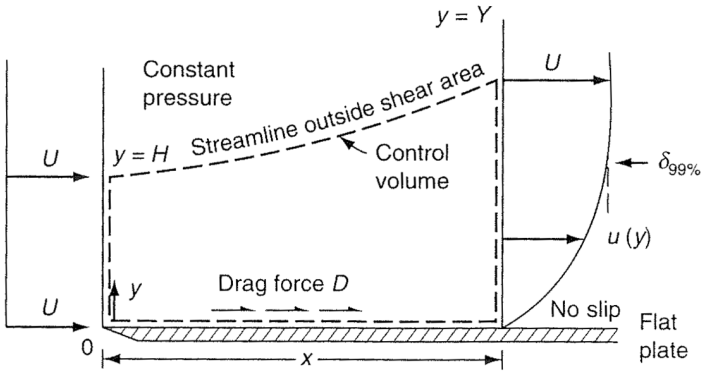

Figure B.1: Control volume over a flat plate boundary layer

The integral momentum balance over the control volume presented in Fig. B.1 is

$$D = \rho U^2 H - \int_0^Y \rho u^2 dy = \rho \int_0^Y u(U-u)dy = \rho U^2 \theta. \tag{B.7}$$

Where D is the drag force and θ refers to the momentum thickness. This leads to a local friction equal to

$$\tau_w = \frac{dD}{dx} = \rho U^2 \frac{d\theta}{dx}. \tag{B.8}$$

Assuming now a simple linear velocity profile in the boundary layer of the form $u \approx Uy/\delta$ at $(y \leq \delta)$ with $\delta = \delta(x)$, the properties of this velocity profile follow,

$$\begin{cases} \tau_w = \mu \left(\frac{\partial u}{\partial y}\right)_{y=0} = \frac{\mu U}{\delta} \\ \theta = \frac{\delta}{6} \end{cases} \tag{B.9}$$

Now substituting these expressions into the integral momentum balance, specifically into the local friction relation B.8 , an estimation can be derived for the boundary layer thickness δ,

$$\frac{\mu U}{\delta} = \rho U^2 \cdot \frac{1}{6}\frac{d\delta}{dx} \quad \Rightarrow \quad \delta \frac{d\delta}{dx} = 6\frac{\mu}{\rho U} \quad \Rightarrow \quad \frac{\delta}{x}\sqrt{Re_x} = K \quad \Rightarrow \quad \frac{\delta\sqrt{Re}}{\sqrt{x \cdot c}} = K \tag{B.10}$$

where K is just a constant value that can be numerically estimated. Such estimations are taken from the literature, for the laminar velocity profile case $K = 3.6$, for the parabolic case $K = 5.5$ and for the exact case $K \sim 5.0$. In order to compute an estimation of the boundary layer for the present experiments, the exact case is used with the standard conditions presented in Table 3.2 as follows,

$$\delta = \frac{5\sqrt{x \cdot c}}{\sqrt{Re}} = \frac{5\sqrt{0.007 \cdot 0.1}}{\sqrt{2.763 \cdot 10^6}} \approx 0.08 \quad [mm] \tag{B.11}$$

B.3 Pressure waves shedding from the laser probe

The laser probe placed inside the wind tunnel and downstream from the airfoil is exposed to a subsonic flow regime at high Reynolds number ($Re \sim 2 \cdot 10^6$). These conditions trigger the shedding of vortices from the probe, and as a result it generates pressure waves at the same frequency. The probe-generated vortices travel downstream and its interaction with the airfoil local flow field can be neglected, however this is not the case for the sound pressure waves resulting from the vortex shedding. In general a body immersed in a subsonic flow generates sound pressure waves that expand radially in a 3-dimensional pattern, nevertheless for the current analysis a two-dimensional approach can be taken for simplification. Under subsonic flow conditions, these waves travel upstream in the flow and they reach the airfoil region. Theoretically, by doing so, they might interact with and modify the flow properties over the airfoil, e.g. these waves may affect the buffet phenomenon. This is the reason why this analysis is conducted in order to study the real influence of the laser probe over the test section region, and more concretely, over the buffet phenomenon.

The morphology and relative position of the PIV probe were shown in Figs. 3.17 and 3.19. Based on this, an analytical estimation can be made about the shedding frequency of vortices and pressure waves. For this purpose and for the sake of simplicity, one can approach the problem as two-dimensional and assume the laser probe geometry to be a 2D cylinder with the same characteristic length. The Strouhal number is defined using the vortex shedding frequency (f_{shed}), the characteristic length of the probe (L) and the local flow velocity (U_∞). The Strouhal number of a cylinder under high Reynolds number conditions ($\sim 2 \cdot 10^6$) can be approximated to 0.2, the characteristic length of the probe (thickness perpendicular to flow) is 30 mm and the local flow speed obtained from PIV results oscillates about 230 m/s for a reference Mach number of 0.70. Rearranging Eq. **??**, the shedding frequency follows

$$f_{shed} = \frac{St \cdot U_\infty}{L} = \frac{0.2 \cdot 230}{0.03} \approx 1500 \quad Hz. \tag{B.12}$$

f_{shed} is the frequency at which the vortex pairs are emitted, however, note that for every pair of vortices two pressure waves emanate from the body, i.e. the wave frequency is twice the shedding frequency, $f_w = 2 \cdot f_{shed}$. This can be proven, if one assumes a constant convective velocity of the waves (total velocity). The wave displacement between two instants of time is

$$\begin{cases} x_\omega = U_{conv} \cdot t \\ x_\omega + \Delta x_\omega = U_{conv} \cdot (t + \Delta t) \end{cases} \quad \Rightarrow \quad \Delta x_\omega = U_{conv} \cdot \Delta t,$$

where x_ω is the wave location at time instant t and U_{conv} is the wave upstream velocity. If this time increment is taken as the time it takes for a vortex pair to be shed into the flow then the displacement Δx_ω can be computed as,

$$\begin{cases} \Delta x_\omega = U_{conv} \cdot \Delta t \\ \Delta t = \frac{1}{f_{shed}} = \frac{\lambda_{vortex}}{U_\infty} \end{cases} \quad \Rightarrow \quad \Delta x_\omega = \lambda_{vortex} \frac{U_{conv}}{U_\infty},$$

and it represents the distance traveled by the wave during one cycle of vortex shedding. Here λ_{vortex} is the wavelength of a vortex pair. Note that during this time increment, two waves

are emitted, which means that actually the wavelength of such waves (λ_ω) is exactly half of the displacement, i.e. $\Delta x_\omega = 2 \cdot \lambda_\omega$. Taking this relation into account it follows,

$$f_\omega = \frac{U_{conv}}{\lambda_\omega} = 2 \cdot \frac{U_{conv}}{\Delta x_\omega} = 2 \cdot \frac{U_\infty}{\lambda_{vortex}} = 2 \cdot f_{shed} \quad \Rightarrow \quad \boxed{f_\omega = 2 \cdot f_{shed}} \tag{B.13}$$

So the pressure waves are emitted from the probe at a frequency of the order of 3000 Hz, and they travel upstream with a relative velocity to the flow equal to the local sound speed a_∞, and with a total velocity $U_{conv} = a_\infty - U_\infty$. It is important to note that both a_∞ and U_∞ are dependent of the x-position as the flow conditions (temperature, pressure and local flow speed) change stream wise, although the variations are relatively small and even more if considered just during the time interval of a vortex shedding cycle, as was done in the calculations. A peak in the vicinity of 3000 Hz is expected to appear in the frequency domain if there is a real direct influence of the laser probe over the flow about the model. However there can also be an indirect influence, more related to a possible variation of the wind tunnel noise levels due to the presence of the laser probe.